UNIVERSITAT DE BARCELONA

Metabolic adaptations in liver-specific OPA1 knockout mice

Susana Raquel Costa Barros

TESIS DOCTORAL

Metabolic adaptations in liver-specific OPA1 knockout mice

Susana Raquel Costa Barros

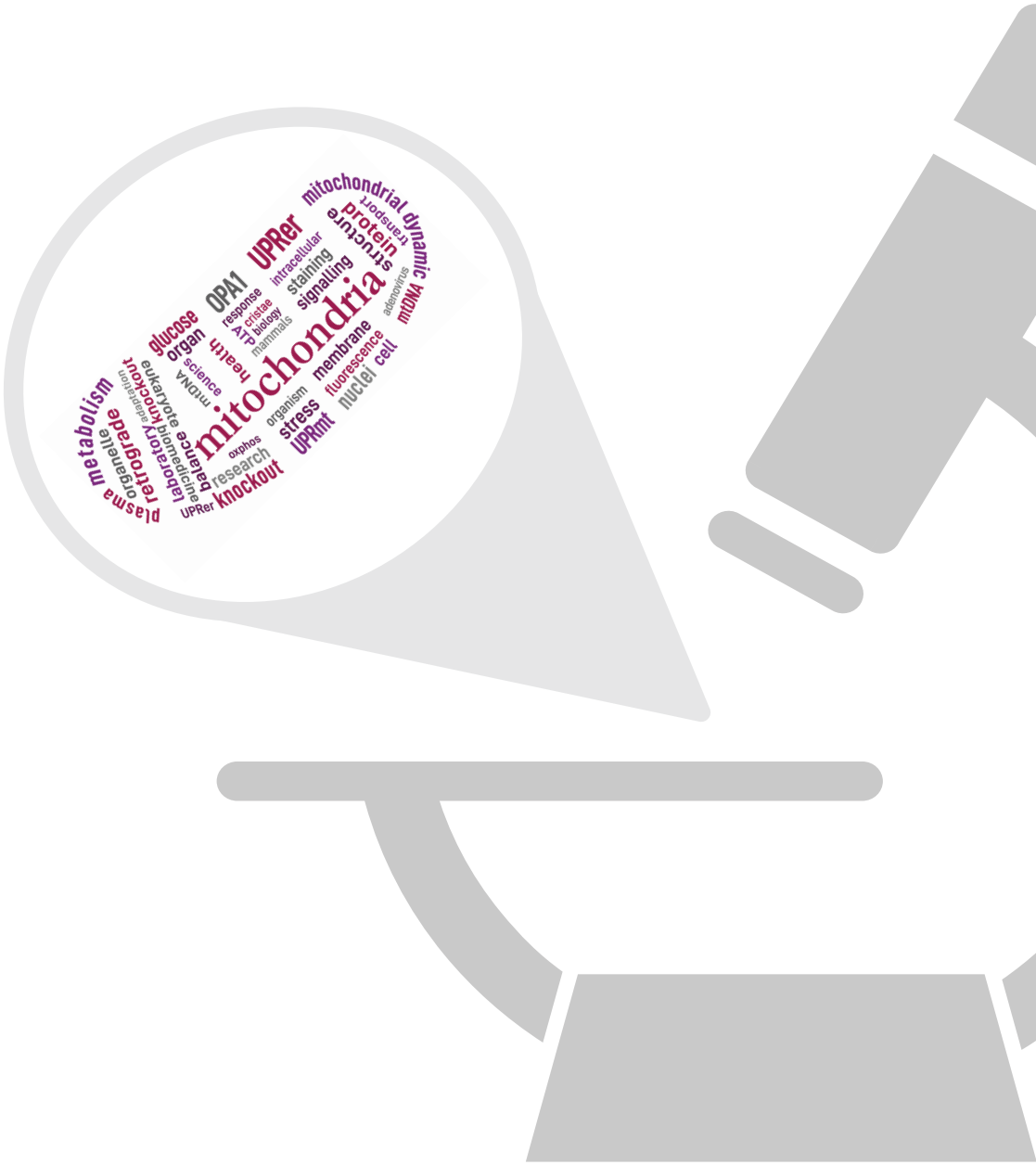

Universidad de Barcelona
Barcelona, 2019

Universidad de Barcelona

Facultad de Biología

Departamento de Bioquímica y Biomedicina Molecular

Metabolic adaptations in liver-specific OPA1 knockout mice

Adaptaciones metabólicas en el modelo de ratón OPA1 "knock-out" específico de hígado

Susana Raquel Costa Barros

Barcelona, 2019

To my grandparents, à avó Edite e ao avô Lúcio,
for their endless caring, love and support.

Biology sometimes reveals its fundamental principles through what may seem at first to be arcane and bizarre.
E. Blackburn

Abstract

OPA1 is a dynamin-related protein that is responsible for the fusion of the internal mitochondrial membrane and essential to control the morphology of the mitochondrial cristae. Thus, it directly impacts the efficiency of OxPhos and the stability of mitochondrial DNA. In this study, we have explored the effects of hepatic deletion of OPA1 on mitochondrial function and metabolism. We have shown that the ablation of OPA1 in the liver produces a mitochondrial dysfunction characterized by alterations in mitochondrial cristae structure, concomitant with a reduced respiratory capacity and mtDNA copy number, and perturbed mitochondrial proteostasis. The mitochondrial dysfunction caused by the ablation of OPA1 in liver triggers the activation of a mitochondrial stress response, including mitochondrial unfolded stress response (UPRmt) that is probably mediated by the transcription factor ATF5.

Interestingly, we have observed that OPA1 deficiency in the liver causes better glucose tolerance and protects against diet-induced obesity and insulin resistance concomitant to a high circulating levels of the metabolic modulator FGF21. Here we suggest that the systemic protective effects associated to OPA1 ablation are due to the action of FGF21, probably mediated by the mitochondrial stress response associated to OPA1 loss-of-function via ATF5 activation.

List of contents

Abbreviations

A

AAA	ATPases associated with diverse cellular activities
ADP	Adenosine diphosphate
ANT2	Adenine nucleotide translocase 2
ARP	Actin related protein
ATF4	Activating transcription factor 4
ATF5	Activating transcription factor 5
ATF6	Activating transcription factor 6
ATFS-1	Stress activated transcription factor 11
ATP	Adenosine triphosphate
ATP5a	ATP synthase (complex V) subunit alpha

B

BAT	brown adipose tissue
BCA	Bicinchoninic acid
bp	Base pair
BSA	Bovine Serum Albumin

C

CCCP	carbonyl cyanide m-chlorophenyl hydrazone
cDNA	Complementary DNA
CHOP	DNA damage-inducible transcript 3 protein
CJs	Cristae junctions
ClpP	ATP-dependent Clp protease

D

Dars2	Aspartate-tRNA synthetase 2
DKO	Double KO
DMEM	Dulbecco's Modified Eagle's medium
DMSO	Dimethyl sulfoxide
DNA	Deoxyribonucleic acid
DRP1	Dynamin-related protein 1
dsDNA	double stranded DNA
DTT	Dithiothreitol

E

EDTA	Ethylenediaminetetraacetic acid
EGTA	Ethylene glycol tetraacetic acid
eIF2a	
ELISA	Enzyme-linked immune-sorbent assay
ER	Endoplasmic reticulum

F

FBS	Fetal Bovine Serum
FCCP	Carbonyl cyanide-4-(trifluoromethoxy)phenylhydrazone
FDR	False discovery rate

FGF21	Fibroblast growth factor 21
FIS1	Fission homologue 1

G

GCN2	
GTP	guanosine triphosphate
GTPase	guanosine triphosphatase

H

H&E	hematoxylin and eosin
HEPES	Hydroxyethyl piperazine ethanesulfonic acid
HRI	
HRP	Horseradish peroxidase
HSP	Heat shock protein
HSP60	Heat shock protein 60

I

IBM	Inner boundary membrane
IMM	Inner mitochondrial membrane
IMS	Intermembrane space
ISR	Integrated stress response

K

KO	Knock-out

L

L-OPA1 KO	Liver-specific knockout
L-OPA1	OPA1 long-forms
loxP	Locus of X(cross)-over in P1

M

MEF	Mouse embryonic fibroblasts
MFF	Mitochondrial fission factor
MFN1	Mitofusin 1
MFN2	Mitofusin 2
MPP	Mitochondrial processing peptidase
mRNA	Messenger RNA
MSR	Mitochondrial stress response
mtDNA	mitochondrial DNA
mtHSP70	Mitochondrial heat shock protein 70
mTOR	Mammalian target of rapamycin
MTS	mitochondrial targeting sequence

N

NAD	nicotinamide adenine dinucleotide
NADH	NAD reduced
nDNA	nuclear DNA
NDUFA8	NADH Dehydrogenase (Ubiquinone) 1 Alpha Subcomplex, 8

O

O/N	Overnight

OMA1	Overlapping Activity With M-AAA Protease
OMM	Outer mitochondrial membrane
OPA1	Optic Atrophy 1
OxPhos	Oxidative phosphorylation

P

p-	Phosphorylated
PBS	Phosphate-buffered saline
PCR	Polymerase Chain Reaction
PERK	
PFA	paraformaldehyde
PGC-1α	Peroxisome proliferator-activated receptor γ coactivator 1 alpha
PKR	
PVDF	Polyvinylidene difluoride

Q

qRT-PCR	

R

RNA	Ribonucleic acid
ROS	Reactive oxygen species
rpm	Revolutions per minute
rRNA	Ribosomal RNA
RT	Room temperature

S

SDHA	Succinate dehydrogenase [ubiquinone] flavoprotein subunit
SDS	Sodium dodecyl sulfate
SKM	Skeletal muscle
S-OPA1	Short-isoforms of OPA1

T

TCA	Tricarboxylic acid
TFAM	Transcription Factor A, Mitochondrial
TIMM	Translocase of inner mitochondrial membrane
TIMM44	Translocase of inner mitochondrial membrane
TM	Transmembrane domain
TMRM	Tetramethylrhodamine
TOMM	Translocase of outer mitochondrial membrane
tRNA	Transference RNA

U

UPRer	Endoplasmic reticulum unfolded protein response
UPRmt	Mitochondrial unfolded protein response
UPS	Ubiquitin-proteasome system
UQCRC2	Ubiquinone cytochrome c reductase subunit core 2 (complex III)

V

ΔΨm	Mitochondrial membrane potential difference

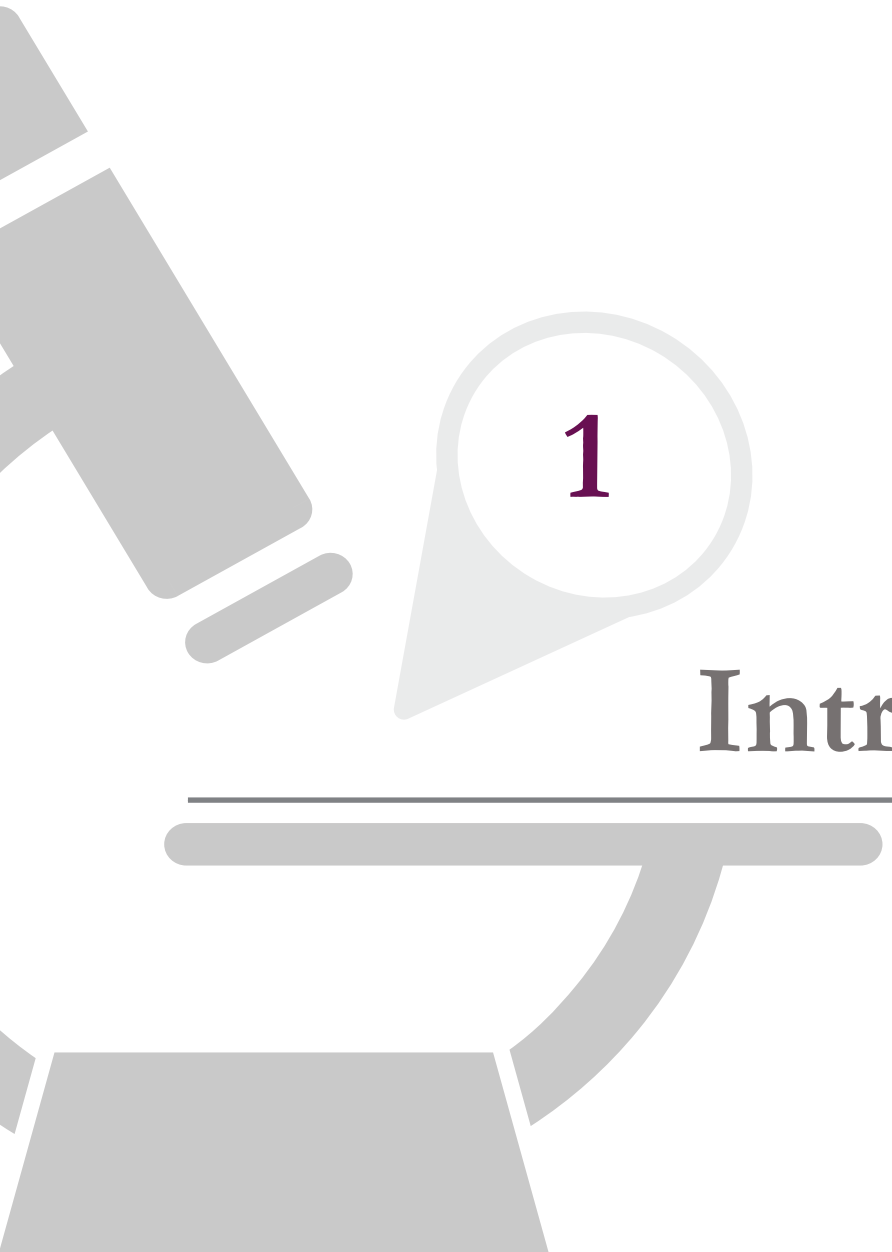

1

Introduction

1 Introduction

1.1 Mitochondria: origin and features

Mitochondria are one of the most ancient endomembrane system in eukaryotic cells, thought to have originated 2 billion years ago by endocytosis (Gray et al. 2001). In 1967 Lynn Margulis rescued the long-term forgotten endosymbiont theory of organelle origin (Sagan 1967), which describes the origin of mitochondria as derived from the engulfment of an α-proteobacterium by the eukaryotic progenitor. Among other features, mitochondria are comprised of two functionally different and separated membranes that surround a matrix compartment which contain the unmethylated mitochondrial circular genome organized as nucleoids throughout the matrix (Nunnari and Suomalainen 2012), resembling a bacterial ancestor and therefore supporting the endosymbiont theory of modern mitochondria origin.

The architecture of mitochondria is essential for the proper function of the organelle. At the ultrastructural level mitochondria are comprised by two membranes: the outer mitochondrial membrane (OMM) and the inner mitochondrial membrane (IMM), and the space between them defines the intermembrane space (IMS). The mitochondrial matrix is the space enclosed by the IMM. The OMM is structurally simple and highly permeable to small molecules and ions, while at the same time, it is able to protect the cell from noxious mitochondrial products including reactive oxygen species (ROS), immunogenic mitochondrial DNA (mtDNA) (Zhang et al. 2010) and death signals. The IMM is morphologically more complex, and it creates an impermeable barrier between the matrix and the IMS. It includes both the inner boundary membrane (IBM), which lies parallel to the OMM, and the cristae formed by tubular IMM invaginations. Cristae junctions (CJs) separate the IBM and cristae, with an opening of only 20-50nm in diameter, thus permitting these two sub-compartments to perform distinct functions (Vogel et al. 2006). The permeability of the IMM is very restricted and it is indeed the major barrier between the cytosol and the mitochondrial matrix, which in physiological conditions allows for the establishment of a proton gradient.

The restrictive permeability of mitochondria together with proper cristae morphology are the two major physical features that enable mitochondria to be: (1) the primary energy-generating system in most eukaryotic cells through oxidative

phosphorylation (OxPhos) (Jayashankar et al. 2016), providing a highly efficient route for eukaryotic cells to generate adenosine triphosphate (ATP) from energy-rich molecules and (2) pivotal in many other cellular functions such as regulation of programmed cell death, calcium homeostasis, and the generation and control of ROS (Hockenbery et al. 1990; Gunter et al. 1998; Nunnari and Suomalainen 2012; Hüttemann et al. 2007) Briefly, OxPhos is a process in which electrons from oxidative substrates are transferred to oxygen, via a series of redox reactions, to generate water. In the process, protons are pumped from the matrix across the IMM through respiratory complexes I, III, and IV. When protons return to the mitochondrial matrix down their electrochemical gradient, ATP is synthesized. During the 1970's, intensive works on mitochondrial OxPhos complex contributed to launching the golden era of mitochondrial research (Guerrieri and Nelson 1975; Brand et al. 1976; Wikström and Krab 1979)

Additionally, the IMS contains several proteins involved in protein transport, cellular homeostasis, mitochondrial bioenergetics and cell death, for example: cytochrome C, apoptosis inducing factor and mitochondrial creatine kinase. Lastly, the mitochondrial matrix accommodates intermediary metabolism through essential mitochondrial processes like the tricarboxylic acid (TCA) cycle, fatty acids b-oxidation, transamination, and Fe-S and Heme-group biosynthesis and amino acids (Osman et al. 2011; Wellen and Thompson 2012; Lill and Mühlenhoff 2008). Also, this matrix contains the mitochondrial genome or mtDNA, distributed in mtDNA nucleoids throughout the matrix, which encodes a small number of genes therein: 13 OxPhos protein coding, 22 transference RNA (tRNA) and 2 ribosomal RNA (rRNA) genes (Gray 1999; Falkenberg et al. 2007). The proteins encoded by mtDNA comprise only about 1% of the mitochondrial proteome, while the other 99% of proteins located in mitochondria are encoded by the nuclear genome, synthesized in the cytosol and subsequently imported into mitochondria. The machineries involved in mitochondrial protein import will be explained in section 2.5 of this introductory chapter.

As mitochondria fulfill numerous metabolic functions, as described above, a reduction in the activity of mitochondria is closely linked with cellular dysfunction and aging, featuring the importance of functional mitochondria activity for cell survival (Lin and Beal 2006; Rodolfo et al. 2010; Seo et al. 2010). Therefore, mitochondrial function and quality need to be strongly modulating to ensure the supply of metabolic building blocks and to prevent the production of harmful agents such as reactive ROS, produced at increased rates upon malfunctioning respiration, for instance.

In order to maintain organelle homeostasis, mitochondria have developed several surveillance mechanisms (Tatsuta and Langer 2008). In general terms, mitochondria defense mechanisms occur: (1) on the molecular level, which involves conserved intraorganellar protein quality control machinery influenced by the action of the ubiquitin-proteasome system (UPS) and the activation of a mitochondria-specific unfolded protein response (UPRmt) that operates in higher eukaryotes to attenuate the side effects of misfolded proteins accumulation in the organelle (Haynes and Ron 2010; Livnat-Levanon and Glickman 2011) (2) the dynamic nature of mitochondria itself arises the quality control at the organelle level, allowing the clearance of damaged mitochondria, in one hand, through fusion with a healthy neighbor mitochondria and restore its deficient components and in case the damage is too extreme and accompanied by dissipation of the mitochondrial membrane potential ($\Delta\Psi m$), mitochondria become fusion incompetent and rather fragmented and, turned over through mitophagy, preventing their fusion with the healthy network, limiting the damage. (Wang and Klionsky 2011; Youle and Narendra 2011) (3) ultimately mitochondrial quality control occurs on a cellular level, whereby large-scale mitochondrial damage promotes release of proapoptotic factors, leading to the entire cell turnover through apoptosis (Wasilewski and Scorrano 2009; Martin 2010).

In this work, as we will focus on the relevance of the mitochondrial dynamics and protein quality control system on metabolic adaptation, special attention will be given to these processes over other processes of mitochondrial quality control and will be described ahead, respectively in sections 2.2 and 2.5 of this chapter.

1.2 Mitochondrial dynamics

The study of mitochondrial dynamics describes how mitochondria undergo events of fusion and fission by which they are shaped to respond and adapt to the cell environment and metabolic requirements. The dynamic nature of mitochondria is crucial for organelle shaping, regulating surveillance mechanisms such as mitophagy and apoptosis, Ca^{2+} signaling, maintaining OxPhos efficiency and mtDNA stability and therefore is tightly connected to mitochondria quality control (Bereiter-Hahn and Vöth 1994; Liesa et al. 2009; Westermann 2010; Chan 2012).

Mitochondrial morphology and function strongly rely on the balance between fusion and fission processes. Reduced fusion or increased fission, for instance, causes mitochondrial fragmentation and symmetrically, reduced fission or increased fusion results in elongation of the mitochondrial network, which is often related to situations of higher cellular energetic demands such as amino acid starvation conditions (Liesa et al. 2009). Genetic studies in yeast were instrumental in identifying large guanosine triphosphate (GTP)-hydrolyzing enzymes of the dynamin superfamily as molecular players in both fusion and fission (Hermann and Shaw 1998; Bleazard et al. 1999; Tieu et al. 2002; Okamoto and Shaw 2005; Klionsky et al. 2016; Mishra and Chan 2016).

Mitochondrial fusion by itself is vital for preserving mitochondrial function by providing mtDNA stabilization which is essential for mitochondrial function. mtDNA encodes essential subunits of the respiratory complexes I, III and IV, which are indispensable for energy generation by OxPhos (Chen et al. 2007; Chen et al. 2003). This process consists of two sequential steps, where the outer and inner mitochondrial membranes fuse separately: first the fusion of the OMM and then the fusion of the IMM (Malka et al. 2005). Mitofusin1 (MFN1) and mitofusin 2 (MFN2) are transmembrane GTPases localized to the OMM and the only mammalian outer membrane proteins known to be essential for mitochondrial fusion .(Chen et al. 2003; Koshiba et al. 2004). Mfn1 and Mfn2 display several conserved domains: two transmembrane domains, a coiled-coil domain (heptad-repeat domain - HR2) located in the C-terminal part, the GTP-binding domain and another coiled-coil domain (HR1) located in the N-terminal part. The transmembrane domains confer mitofusins a U-shaped structure and as a result, both the HR2 and GTPase domain are exposed to the cytosol. The tethering of two adjacent mitochondria is accomplished through assembling a dimeric antiparallel coiled-coil structure, which can be homotypic (Mfn1-Mfn1 or Mfn2-Mfn2) or heterotypic (Mfn1-Mfn2). Optic Atrophy 1 (OPA1) is the dynamin-related protein (Alexander et al. 2000; Delettre et al. 2000) responsible for the IMM fusion (Cipolat et al. 2004; Chen et al. 2005) and it is the of center our research, which will be described more into detail in section 2.3 of this introduction.

The opposing process is mitochondrial fission and is necessary to drive old or damaged mitochondria via mitophagy. Dynamin-related protein 1 (DRP1), mitochondrial fission 1 (FIS1) and the mitochondrial fission factor (MFF) are the most relevant proteins in mitochondrial fission, being DRP1 the master regulator of this process in most eukaryotic

organisms (Smirnova et al. 2001). Drp1 contains a GTPase domain, a middle domain and the GED or assembly domain (Liesa et al. 2009; Otera et al. 2010; Losón et al. 2013).

During fission process DRP1 dimer or tetramer, localized in the cytoplasm, is recruited from the cytosol onto mitochondria by the four DRP1 receptors, Fis 1, MFF and mitochondrial dynamics protein of 49 kDa (MID49) and of 51 kDa (MID51) that are located on the OMM at sites marked by endoplasmic reticulum (ER) tubules (Otera et al. 2010; Friedman et al. 2011). These oligomeric structures that depend on GTP binding, wrap around mitochondria, generating a spiral ring around the scission site lately causing constriction of the organelle. Finally, the mitochondria membrane is divided by GTP hydrolysis (Hoppins et al. 2007; Ingerman et al. 2005; Chen and Chan 2004).

1.3 Optic Atrophy 1 (OPA1) in mitochondrial function

Opa1 is a dynamin-related GTPase localized in the mitochondrial intermembrane space in soluble forms or attached to the inner membrane (Akepati et al. 2008) and it controls mitochondrial fusion of the IMM and cristae remodeling (Cipolat et al. 2004; Chen et al. 2005; Ishihara and Mihara 2005). The gene was found years after describing the mutations in the locus containing it that are associated to the neurodegenerative disease autosomal dominant optic atrophy (ADOA; MIM165500) (Eiberg et al. 1994). Although it is expressed in all the tissues tested, OPA1 is highly expressed in retina, brain, testis, liver, heart, skeletal muscle (SKM), and pancreas (Akepati et al. 2008; Liesa et al. 2009).

The OPA1 gene in mice is localized on chromosome 16, includes 32 exons and its biogenesis is regulated both at the transcriptional and pos-transcriptional level. The alternative splicing of exons 4b and 5b generates 4 different mRNA variants, splice variants 1, 5, 7, and 8, coding 4 isoforms (Akepati et al. 2008). In mice, isoforms 1 and 7 are predominantly expressed and originate the precursor of OPA1. (Ishihara et al. 2006; Delettre et al. 2000; Olichon et al. 2003; Akepati et al. 2008).

OPA1 precursor is composed by an N-terminal mitochondrial targeting sequence (MTS), which targets OPA1 to mitochondria import followed by a first transmembrane domain (TM), anchoring the protein to the inner mitochondrial membrane (IMM) and includes S1 and S2 cleavage sites, and by the three alternate spliced domains corresponding

to exons 4b and 5b which provide two additional hydrophobic domains, TM2a and TM2b. 5b exon also encodes a coiled coil domain (CC0). The following part of the protein includes a coiled coil domain (CC1), then the conserved dynamin regions: the GTPase domain, the middle domain with unknown function and the C-terminus GTPase effector domain (GED) also containing a coiled coil domain (CC2) (Song et al. 2007).

After the import to mitochondria, OPA1 precursor is cleaved at the MTS by matrix-processing peptidase (MPP) originating membrane-bound long (L)-OPA1 forms that can be further processed at two protease cleavage sites downstream the TM region, S1 and S2, to generate short (S)-OPA1 forms, required for anchoring mtDNA nucleoids to the IMM (Ishihara et al. 2006; Alexander et al. 2000; Delettre et al. 2000; Akepati et al. 2008). S-OPA1 forms can be peripherally attached to the IMM or diffuse in the inter-membrane space (IMS) (Olichon et al. 2003; Song et al. 2007; Satoh et al. 2003).

The proteolytic processing of OPA1 is performed by two IMM proteases, which have their catalytic sites exposed to the IMS (Anand et al. 2014). In one hand, the i-AAA protease (intermembrane space oriented) or YME1L acts constitutively at S2, thus only a half of OPA1 isoforms are converted. On the other hand, m-AAA (m, matrix oriented) zinc metalloprotease Overlapping Activity with M-AAA Protease (OMA1) is able to cleave all L-OPA1 at S1 in an inducible manner (Kaser et al. 2003). The activity of these two IMM proteases establishes a near equimolar equilibrium of long and short OPA1 forms under basal conditions (Griparic et al. 2007; Song et al. 2007; Wai and Langer 2016).

Several groups have demonstrated that OPA1 processing is regulated in response to different kinds of mitochondrial stress as in, mitochondrial dysfunction, oxidative stress, heat stress, or mitochondrial $\Delta\Psi m$ dissipation (Ishihara et al. 2006; Quirós et al. 2012), which inhibits fusion by complete conversion of L-OPA1 to S-OPA1 forms (Duvezin-Caubet et al. 2006; Song et al. 2007; Guillery et al. 2008). Alterations in $\Delta\Psi m$ or intra-mitochondrial ATP levels were found to trigger OMA1 protease (Baricault et al. 2007). OMA1 possesses the autocatalytic capacity of turnover upon the disappearance of the stimuli (Baker et al. 2014).

OPA1 has been described to be responsible for the fusion of the IMM and its absence provokes fragmentation of the tubular mitochondrial network. Conversely, overexpression of OPA1 protein promotes mitochondrial elongation in cells where mitochondria are fragmented (Olichon et al. 2003; Griparic et al. 2007; Song et al. 2009).

Several experiments in OPA1-depleted cells confirmed that mitochondrial fusion is impaired, demonstrating the profusion activity of OPA1 (Cipolat et al. 2004; Chen et al. 2005; Song et al. 2007; Song et al. 2009).

Additionally, OPA1 activity is not only related to mitochondrial fusion but it also maintains mitochondrial function independently on fusion. OPA1 is responsible for modulating cristae morphology, affecting mitochondrial respiratory capacity, mtDNA content and $\Delta\psi m$ (Olichon et al. 2003; Cipolat et al. 2004; Frezza et al. 2006; Griparic et al. 2007; Chan 2012; Merkwirth et al. 2008; Song et al. 2009; Elachouri et al. 2011; Twig et al. 2008). It has been shown that the oligomerization of OPA1 in the cristae junction controls its width as well as the width of the cristae lumen, which has been observed to be crucial for the induction of pro-apoptotic-dependent cytochrome C release upon OPA1 cleavage. (Frezza et al. 2006). Furthermore, by maintaining mitochondrial cristae structure, OPA1 has a direct metabolic effect stabilizing respiratory chain supercomplexes, thus affecting directly mitochondrial respiratory capacity (Olichon et al. 2003; Cogliati et al. 2013; Mishra and Chan 2014; Civiletto et al. 2015; Varanita et al. 2015; Cogliati et al. 2016).

1.4 Mitochondrial fusion and metabolic alterations

Some research has been published on the relation between alterations in mitochondrial dynamics proteins and metabolic alterations. In our group, evidence of that Mfn2 plays an essential role in metabolic homeostasis was provided. Liver-specific ablation of Mfn2 in mice led to numerous metabolic abnormalities, characterized by glucose intolerance and enhanced hepatic gluconeogenesis. Furthermore, Mfn2 deficiency impaired insulin signaling in liver and muscle, associated with ER stress, enhanced hydrogen peroxide concentration, altered reactive oxygen species handling, and active JNK (Sebastián et al.) On the other hand, KulkRNAi et al. (2016) described that the liver-specific deletion of the Mfn1 gene led to a highly fragmented mitochondrial network coupled to an enhanced mitochondrial respiration capacity and a preference for the use of lipids as the main energy source, which protected Liver-specific Mfn1 knockout mice against insulin resistance induced by a high-fat diet.

Additional research in SKM showed that inducible SKM-specific OPA1 deficiency of young mice resulted in non-lethal progressive mitochondrial dysfunction that locally provoked muscle atrophy and distally modulated of whole-body metabolism, protecting the animals against age- and diet-induced weight gain and insulin resistance (Pereira et al. 2017). In our laboratory, Rodriguez-Nuevo et al. (2018) demonstrated that muscle atrophy caused by muscle-specific Opa1 ablation is associated to muscle inflammation characterized by NF-κB activation, and enhanced expression of pro-inflammatory genes, which induced enhanced fibroblast growth factor 21 (FGF21) levels accompanied by a dramatic reduction in life-span.

1.5 Quality control of mitochondrial proteostasis

Mitochondria are composed of well over 1000 proteins, the majority located in the matrix. Mitochondrial genome encodes 13 transmembrane proteins of the respiratory, together with a set of 22 tRNAs and two rRNAs, required for the assembly of a translation machinery in the matrix (Mercer et al. 2011). The remainder of the mitochondrial proteome is comprised of nuclear-encoded proteins (~1 500 in humans) that are synthesized by cytosolic ribosomes and targeted to each compartment within the mitochondrial network. and subsequently imported via the TOMM (translocase of the outer membrane) and TIMM (translocase of the inner membrane) channels (Kovermann et al. 2002; Rehling et al. 2003). Transport of a protein is dependent on the presence of a MTS, the $\Delta\Psi m$, ATP and molecular chaperones located within the mitochondrial matrix (Neupert and Herrmann 2007; Chacinska et al. 2009).

Nuclear-encoded proteins are also susceptible to age-associated damage as they can become misfolded and aggregate, which can be exacerbated by locally produced reactive oxygen species ROS during normal OxPhos-mediated ATP production, an inevitable unwanted by-product from complexes I and III activities. Proteins oxidation may result in loss of protein function (Stadtman and Berlett 1998). Also, uncoordinated expression of nuclear or mtDNA encoded subunits leads to an increase in unassembled subunits, which must be turned over to prevent mitochondrial stress (Curtis et al. 2012). Additionally, mutations in mtDNA and accumulation of damaged mtDNA adversely affect mitochondrial proteostasis (Naresh and Haynes 2019; Moehle et al. 2019). Due to the archetypic origin of mitochondria and the resulting physical separation from the cytosol, both imported and

mitochondrially translated proteins are folded and need to be quality controlled to maintain mitochondrial proteostasis. The proper function of proteins and maintenance of proteostasis entails the tight control of protein folding, including co-translational and post-translational folding, maturation, and degradation of proteins. The mitochondrial matrix forms a largely independent protein compartment providing its own translation and protein quality control machinery including chaperones and proteases capable of counteracting the effects of an imbalanced proteostasis.

Mitochondria contain their own set of matrix localized heat shock proteins (HSP) 70, chaperonins, and proteases to maintain proteostasis and protect mitochondria from proteotoxicity. The turnover of misfolded or damaged proteins in mitochondria is accomplished by a specific mitochondrial complement of proteases. The mitochondrial matrix harbors members of the Lon protease family, which is conserved among prokaryotes and eukaryotes (Desautels and Goldberg 1982; van Dyck et al. 1994). Lon is required for the elimination of denatured or oxidatively damaged proteins (Suzuki et al. 1994; Bota and Davies 2002). Although Lon can degrade mildly oxidized hydrophobic substrates, severely oxidized substrates aggregate, rendering them resistant to degradation (Bota and Davies 2002). Lon functions in collaboration with the chaperone system, which keeps the aimed proteins in an unfolded state until their proteolytic removal can be initiated (Wagner et al. 1994; Bender et al. 2011). In mammalian mitochondria, Lon has been shown to degrade the mitochondrial transcription factor A (TFAM) (Granot et al. 2007; Matsushima et al. 2010).

A second protease exists in the mitochondrial matrix, the ATP-dependent Clp protease (ClpP), which is conserved from bacteria to higher eukaryotes (Sagarra et al. 1999; Santagata et al. 1999). ClpP functions in a complex with ClpX, an AAAþ chaperone protein in the mitochondrial matrix and it is postulated that ClpX is required for substrate recognition (Kang and Hamasaki 2002). Even though the function of ClpXP within mitochondria is still not completely defined, a study described that ClpP is able to degrade a folding impaired mutant of the mitochondrial enzyme, medium chain acyl-CoA dehydrogenase (Hansen et al. 2005).

1.6 Mitochondrial Unfolded Stress Response (UPRmt) and Mitochondrial Stress Responses (MSR)

Upon proteostasis failure, stress responses are rapidly activated in an attempt to alleviate proteostasis defects by modulating the folding environment through the availability of chaperones, responsible for the proper protein folding. A hallmark of these responses is that they are highly acute, pro-survival responses that aim to alleviate transient stresses to restore homeostasis and support cell survival. However, upon chronic activation, they typically shift towards pro-death responses (D'Amico et al. 2017). The stress responses to several mitochondrial stresses, such as hypoxia and oxidative stress, are nowadays well characterized, including the pathways by which they potentially trigger cell death. However, how cells react to mitochondrial proteotoxicity caused by accumulation of misfolded proteins in mitochondria is still not well understood, despite the significant impact of protein aggregation on mitochondrial function and cellular health.

By far, one of the most significant discoveries in mitochondria biology has been the identification of mitochondria as signaling organelle and in the late 1990's the UPRmt, a retrograde stress response induced by mitochondrial proteotoxic stress was first described (Martinus et al. 1996; Ryan et al. 1997). Since then, this is an area of increased scientific interest for research on aging and metabolic diseases. Although initially characterized in mammalian cells, getting mechanistic insight on the UPRmt was possible through studies in worms and flies. In the last few years, the mechanism of UPRmt regulation was partially revealed in mammals as well as worms (Haynes and Ron 2010; Nargund et al. 2015), in which the mitochondrial chaperones and proteases involved in the regulation of mitochondrial proteostasis may have an essential role in the modulation of this process and perhaps in metabolic adaptation in mammalian cells and mice.

Similar to *C. elegans*, the transcriptional regulation of the UPRmt in mammalian cells is also mediated by multiple bZIP transcription factors including transcription factor 5 (ATF5) (Fiorese et al. 2016). ATF5 harbors an MTS and therefore in the absence of stress is localized in mitochondria but it specifically responds to mitochondrial stress by translocating and accumulating in the nucleus. Moreover, ATF5 has been described to rescue UPRmt activation in nematodes lacking stress activated transcription factor 1 (ATFS-1) and cultured cells ATF5 transcriptionally up-regulates mitochondrial chaperones and proteases during mitochondrial stress, by which ATF5 has been proposed to be the key effector of UPRmt

activation (Fiorese et al. 2016). However, in mammalian systems, studies have suggested that UPRmt activation requires at least two additional bZIP proteins, ATF4 and CHOP, as rotenone exposure transcriptionally up-regulates both ATF4 and DNA damage-inducible transcript 3 protein (CHOP) (Horibe and Hoogenraad 2007; Silva et al. 2009). In Fiorese's model, ATF5 is proposed to be activated downstream of eIF2α-phosphorylation but independent of ATF4 activity.

Nonetheless, all three transcription factors are linked to the integrated stress response (ISR), which is a conserved adaptive response, from yeast to mammals, activated by a wide variety of stressors. The ISR was first characterized in yeast as the "general control pathway," activated during amino acid deprivation. The ISR initiation is mediated by kinases that respond to specific stressors and phosphorylate serine 51 of the translation initiation factor subunit eIF2α (Pathak et al. 1988). The mammalian ISR kinases are RNA-dependent protein kinase (PKR)-like ER kinase (PERK), heme-regulated eIF2α kinase (HRI), doublestranded PKR, and general control nonderepressible 2 (GCN2). PERK, HRI, and PKR are specifically activated in response to perturbations in ER homeostasis, heme availability, and the presence of cytosolic double-stranded RNA, respectively (Meurs et al. 1990) (Harding et al. 1999; Chen and London 1995). GCN2 is activated by amino acid or glucose deprivation, ROS, ribosome stalling, mitochondrial dysfunction, and UV light (Dever et al. 1992; Deng et al. 2002; Baker et al. 2012). Ultimately, eIF2α phosphorylation causes attenuation of global protein synthesis while promoting the selective translation of messenger RNAs (mRNAs) harboring upstream open reading frames (uORFs) in the 5' untranslated region (5'UTR). The bZIP transcription factors CHOP, ATF4, and ATF5 are among the mRNAs selectively translated on eIF2α phosphorylation (Pakos-Zebrucka et al. 2016). However, the nuances of the interdependence between these transcription factors during mitochondrial stress or which kinases are specifically activated by which mitochondrial perturbations is not yet fully understood.

Due to the current lack of insight and to avoid confusion as to the numerous mitochondrial stresses and responses observed, it is important to distinguish between mitochondrial stress response (MSR) and UPRmt, depending on the primary involvement of mitochondrial protein misfolding as causative agent. Essentially, not all mitochondrial stress responses are apparently induced by mitochondrial protein misfolding, but still show a certain degree of similarity to the UPRmt by relying on overlapping pathways. Several studies have demonstrated that activation of mitochondrial stress response via ISR may not be associated to protein unfolding in the mitochondria.

Here we describe a few: (1) accumulation of mtDNA deletions in SKM resulted in the induction of ATF4 and ATF5, mediated by mammalian target of rapamycin (mTOR) activity, however, whether this response is mediated by protein misfolding in the matrix remains unclear, as this response also included the activation of markers of the canonical UPRmt (Khan et al. 2017); (2) Knockout of the mitochondrial aspartate-tRNA synthetase 2 (Dars2) in mice caused mitochondrial translation defects and respiratory deficiency without any apparent effects on mitochondrial protein misfolding and rather activated ISR (Dogan et al. 2014), (3) Knockout of Surf1, a complex IV assembly factor, in the SKM of mice leads to decreased respiration and causes induction of CHOP, HSP60 and LONP1 without apparent effects on mitochondrial protein folding (Pulliam et al. 2014; Pharaoh et al. 2016; Dell'agnello et al. 2007); (4) Michel et al. (2015) have demonstrated that inhibition of mitochondrial translation leads to GCN2-dependent ISR induction activating CHOP, without stimulating chaperonins and finally, (5) ATF4 has been described as key regulator of the mitochondrial stress response in mammals, without activation of ATF5 or canonical UPRmt (Quirós et al. 2017).

Together, these described MSRs are able to induce adaptation mechanisms, largely mediated by retrograde signaling (via the ISR) and transcriptional modulation, and some potentially utilize signaling through the canonical UPRmt transcriptional response.

1.7 Integration of mitochondrial dysfunction, UPRmt, MSRs and metabolic adaptations

Mitochondrial dysfunction, characterized by alterations in OxPhos, has often been placed as an underlying genetic factor of metabolic diseases including type 2 diabetes mellitus (T2DM) and obesity (Sreekumar et al. 2002, Mootha et al. 2003b; Sparks et al. 2005; Petersen et al. 2004). However, the past few years several studies have documented the occurrence of a metabolic adaptation associated to mitochondrial dysfunction, which is not surprising considering the central role mitochondria play in metabolism and its capability as a signaling organelle.

Studies in *in vivo*, using mammalian models of mitochondrial dysfunction in liver have demonstrated that hepatic mitochondrial dysfunction is able to trigger systemic metabolic adaptations: (1) muscle- and liver-specific AIF ablation in mice initiates a pattern of OxPhos

deficiency absent of ROS generation that results in increased glucose tolerance, reduced fat mass, and increased insulin sensitivity, in chow and high-fat diet, due to metabolic shifts including glucose metabolism, and possibly to inefficient utilization of fuels such as fatty acids (Popsilik, 2007) and (2) targeted disruption of the predominant isoform of hepatic mitochondrial adenine nucleotide translocase (ANT2), responsible for adenosine diphosphate/adenosine triphosphate (ADP/ATP) exchange, enhances uncoupled respiration without damaging mitochondrial integrity and protects liver-specific ANT2 knockout mice against diet-induced obesity, hepatic steatosis, and insulin resistance (Cho et al., 2017). However, both studies lack knowledge on the key molecular players of the systemic metabolic adaptation.

The modulation of metabolism caused by mitochondrial stress responses, has been connected to the release of signaling factors from tissues or organs with primary mitochondrial damage. These mediating factors are known as mitochondrial cytokines, or mitokines, and are secreted in response to mitochondrial dysfunction in an attempt to re-establishing the whole-body metabolism homeostasis. Over the years several groups have dedicated their research to the FGF21 function over energy metabolism and as a stress hormone and there is compelling evidence that both nutritional and cellular stress stimuli can induce FGF21 secretion in liver and some other responsive tissues, leading to increased circulating levels.

In physiological conditions, FGF21 is mainly produced by the liver, during fasting, however other tissues have been observed to express FGF21 as well (Nishimura et al., 2000 Zhang et al., 2008 Johnson et al., 2009 et al., 2007, Patel et al., 2015). On those conditions, the liver releases FGF21 which action mediates an adaptive starvation (1) local response, involving the induction of ketogenesis, reduction of gluconeogenesis and FFA β-oxidation (Inagaki et al., 2007; Izumiya et al., 2008) and (2) a paracrine response enhancing glucose uptake into tissues, by increasing insulin sensitivity and lipolysis in white adipose tissue (WAT). This type of crosstalk enhances the capacity of FGF21 to regulate energetic homeostasis and to promptly respond to different stresses.

Indeed, studies have extensively associated the eIF2a-phosphorylation and downstream ATF4 activation, part of the endoplasmic reticulum unfolded protein response (UPRer) and ISR, to the induction of FGF21 (Kim et al., 2015, Schaap et al., 2013). However, in the past years, studies started to demonstrate the relevance of MSR and UPRmt in the

stimulation of FGF21 release. Khan et al. (2017) demonstrated that mitochondrial dysfunction caused by the accumulation of mtDNA deletions in SKM, leads to the induction of FGF21 mediated by the activation of ATF4 and ATF5 in a mTOR activity-dependent manner. Also, the activation of the markers of the canonical UPRmt activation is observed in this model. Chung et al. (2017) have recently that OxPhos-deficiency in SKM activates UPRmt and induction of mitokines, thereby maintaining whole-body energy metabolism homeostasis during diet-induced obesity. Additionally, mitochondrial dysfunction caused by OPA1 SKM-specific ablation have been shown to induce FGF21 (Pereira et al., 2017; Tezze et al., 2017; Rodríguez-Nuevo et al., 2018).

In this regard, further studies should be followed to enlighten the relevance of MSRs and UPRmt in the transient modulation of systemic metabolism. Understanding how mitonuclear communication network and cell non-autonomous hormonal factors apply beneficial effects in energy metabolism will possibly challenge the concept of mitohormesis defined as a response to low, non-cytotoxic ROS levels that increases fitness and confers resistance to subsequent stresses to a more global concept of a mitohormetic effect upon generalized mitochondrial dysfunction.

2

Objectives

2 Objectives

There is compelling evidence documenting the key role of OPA1 in mitochondrial quality and function. Recently, our group demonstrated that OPA1 specific-SKM ablation caused FGF21 induction due to the up-regulation of ATF4 target genes in muscle. This suggests that the absence of OPA1 induces a systemic response (Rodríguez-Nuevo et al. 2018), and the ablation of OPA1 activates a mitonuclear communication.

The main goal of the present thesis is to evaluate the link between the impact of OPA1 loss of function in mitochondrial quality and glucose homeostasis in a liver-specific knockout mouse model. To this end, the following specific objectives have been pursued:

1. To evaluate the mitochondrial dysfunction caused by OPA1 loss-of-function;6
2. To characterize the metabolic impact associated to ablation of OPA1 in liver;
3. To identify the key players responsible for the metabolic response associated to OPA1 deficiency in liver.

3

Results

3 Results

3.1 Evaluation of the impact of OPA1 loss-of-function in mitochondrial function in liver

3.1.1 Validation of liver-specific OPA1 knockout mice model

The generation of liver-specific OPA1 knockout (L-OPA1 KO) mice was performed by crossing homozygous Opa1$^{loxP/loxP}$ mice (Rodríguez-Nuevo et al. 2018) with a mouse strain expressing Cre recombinase under the control of the albumin promotor (Alb-Cre) (Figure 1.A). When the *Opa1* gene was disrupted in liver using the Alb-Cre/loxP system, OPA1 levels were practically inexistent in liver extracts (Figure 1.B) while unaffected in other tissues (Figure 1.C).

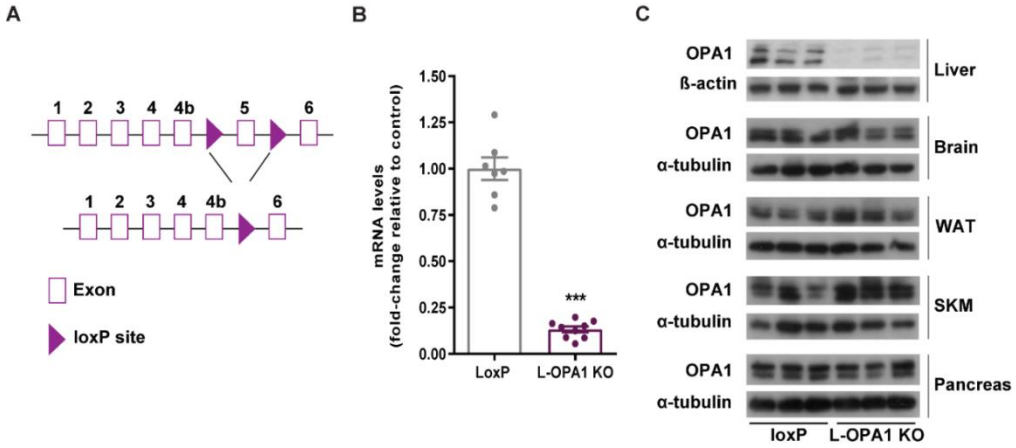

Figure 1. Liver-specific OPA1 knockout mouse model generation. (A) Partial genomic structure of the Opa1 gene showing the scission of exon 5, thus deleting all isoforms of OPA1 protein. (B) *Opa1* mRNA levels in the liver from loxP and and L-OPA1 KO mice (n=7-8). (C) Representative western blot of OPA1 protein levels in liver, brain, white adipose tissue (WAT), skeletal-mucle (SKM) and pancreas tissue homogenates of control loxP (loxP, non-expressing Cre Opa1$^{loxP/loxP}$) and liver-specific OPA1 KO (L-OPA1 KO) mice (n=7-8). Data represent mean ± SEM. *** $p<0.001$ vs. control loxP mice.

Mice were fertile, viable and the progeny respected the Mendelian proportions of the expected genotypes; 100% of the offspring were loxP, in which 50% were homozygotic loxP non-expressing Alb-Cre recombrinase and 50% were homozygotic loxP expressing Alb-Cre recombrinase. At 8 weeks of age, alterations in liver structure, mitochondrial function and

morphology was characterized to further describe the phenotype associated to the hepatic depletion of OPA1.

3.1.2 Characterization of mitochondrial function and morphology

3.1.2.1 Mitochondrial morphology and mitochondrial cristae structure

OPA1 also plays a structural role in maintaining cristae structure and in modulating cristae shape, therefore we then evaluated mitochondrial morphology and cristae structure in livers of 8-week-old L-OPA1 KO and control loxP mice. We analyzed μm liver sections by transmission electron microscopy and image analysis revealed that OPA1-KO livers showed fragmented rounded-shape mitochondria and disorganized cristae structure in comparison with control loxP mice (Figure 2; loxP - upper panel; L-OPA1 - lower panel).

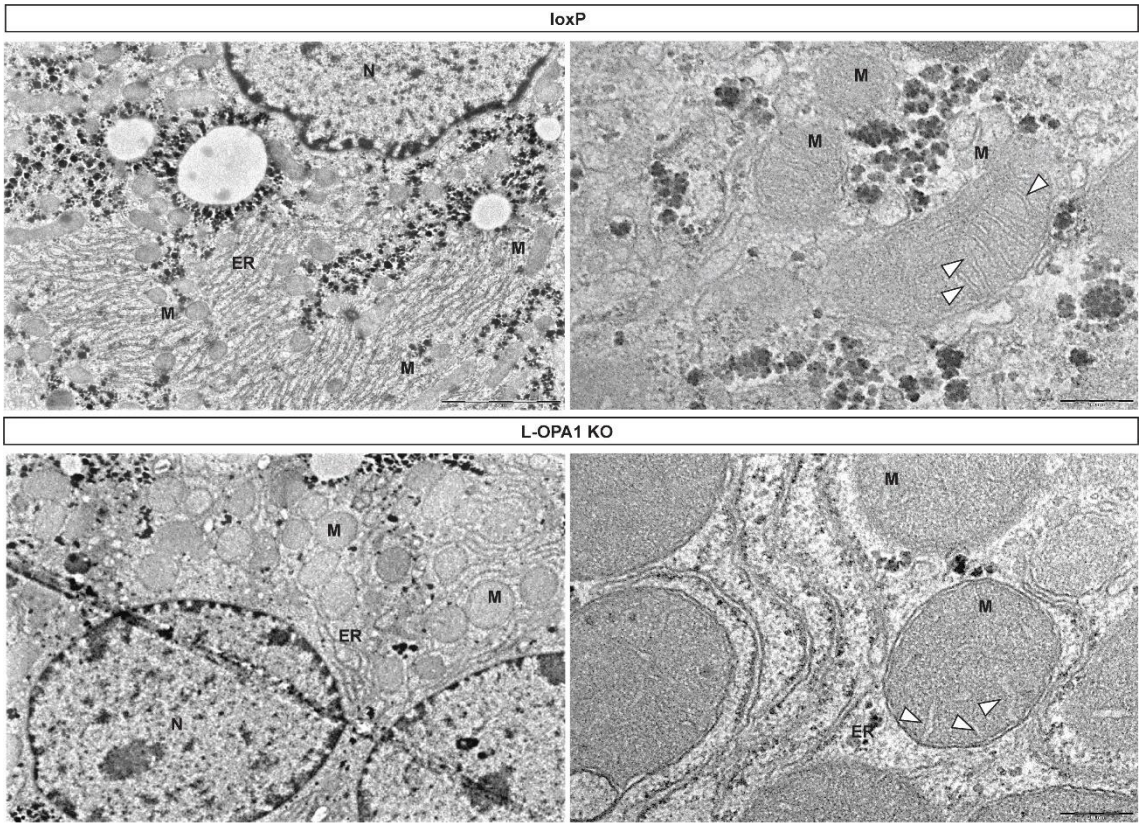

Figure 2. Mitochondrial cristae morphology is perturbed in L-OPA1 KO mice. Representative electron micrograhs of livers from control loxP and L-OPA1 KO mice. (n=3). (ER) Endoplasmic Reticulum. (M) Mitochondria. (N) Nuclei. Mitochondrial cristae indicated by arrows in the figure, in both panels. Scale bar 2 μm.

3.1.2.2 Mitochondrial respiration

The alterations in mitochondrial morphology and mitochondrial structure observed in L-OPA1 KO livers led us to think that in these livers, mitochondria activity would be compromised, as the structural role of OPA1 in mitochondria is intimately associated to mitochondrial oxidative efficiency by modulating the functional organization of the mitochondrial super-complexes. Based on this, to assess the rate of oxygen consumption of OPA1-deficient livers we performed high-resolution respirometry analysis in total liver homogenates obtained from L-OPA1 KO and control loxP mice using the O2k-Respirometer (OROBOROS). This methodology provides us the global vision of the functioning of the mitochondrial respiratory chain through the successive addition of different substrates and inhibitors to the chambers of the O2k-Respirometer (section 7.2.1.8 of Materials and Methods).

At 8 weeks of age, 5 loxP control mice and 4 L-OPA1 KO mice were sacrificed, total liver homogenates were obtained and transferred to the O2k-Respirometer chamber. The protocol began by measuring basal respiration (state 4), in the presence of glutamate (2mM) and malate (10mM), substrates that provide NADH to complex I of the respiratory chain, and in absence of ADP. ADP was added at a saturating concentration (250 μM) to measure the oxygen consumption in state 3 with substrates of complex I [State 3 (I)]. Subsequently, mitochondrial respiration was stimulated with succinate (10mM) to estimate the capacity of oxidative phosphorylation in the presence of substrates of the complex I and complex II in order to measure State 3 (I + II). Finally, rotenone and antimycin A were added, inhibitors of complexes I and III of the respiratory chain, respectively. In this way, residual or non-mitochondrial oxygen was obtained, which was deducted from the previous values referring as exclusive mitochondrial respiration.

Basal mitochondrial respiration was 92.5 ± 21.8 pmol O2/s·mg in the total homogenates of control livers and 33.9 ± 10.5 pmol O2/s·mg in th total homogenates of L-OPA1 KO livers. The addition of ADP stimulated oxygen up to 192.3 ± 37.9 pmol O2 / s ·mg in controls and up to 101.3 ± 28.2 pmol O2/s·mg in the case of L-OPA1 KO livers. The addition of succinate stimulated respiration up to 756.0 ± 88.2 pmol O2/s·mg and 310.4 ±114.3 pmol O2/s·mg in control livers and L-OPA1 KO livers, respectively (Figure 3).

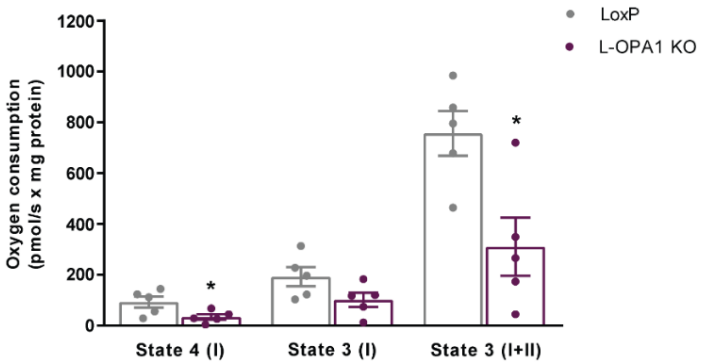

Figure 3. Hepatic mitochondrial respiration is impaired in L-OPA1 KO mice. Oxygen consumption assayed in liver total homogenates isolated from loxP or KO mice (n=4-5). Data represent mean ± SEM. * $p<0.05$ vs. loxP.

3.1.2.3 OxPhos subunits levels and mitochondrial content

The results obtained from respiration studies, which give us information on the global activity of the electron transport chain, showed that OPA1 absence in liver causes reduced mitochondrial respiration, characterized by substantial reduction in complex I and complex II activity. To check whether the decrease in mitochondrial respiratory capacity observed in L-OPA1 KO livers was due to a reduction in the expression of these complexes, we next analyzed the expression of subunits of all mitochondrial complexes in liver homogenates of L-OPA1 KO and control loxP mice. Protein expression analysis revealed a substantial reduction in the expression of NDUFA8 (complex I; NADH dehydrogenase [ubiquinone] 1 alpha subcomplex subunit 8) in parallel with reduced content of SDHB (complex II; succinate dehydrogenase [ubiquinone] iron-sulfur subunit beta), UQCRC2 (complex III; cytochrome b-c1 complex subunit 2), MTCO2 (complex IV; mitochondrial cytochrome c oxidase subunit 2) and ATP5A (complex V; ATP synthase F1 subunit alpha) (Figure 4.A-B).

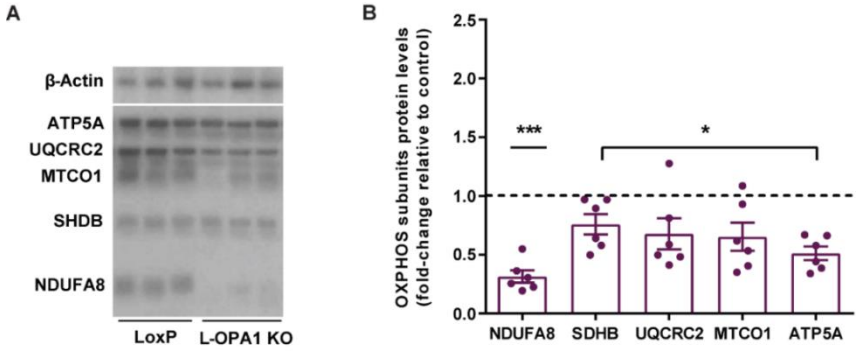

Figure 4.

Figure 4. OxPhos subunits expression is reduced in L-OPA1 KO. (A) Representative western blot of relative mitochondrial OxPhos subunits expression of liver of loxP and L-OPA1 KO. OPA1 (n=6). (B) Protein expression levels of complex I subunit NDUFA8, complex II subunit SDHB, complex III subunit UQCRC2, complex IV subunit MTCO1 and complex V subunit ATP5A. Data represent mean ± SEM. * p<0.05, *** p<0.001 vs loxP

To evaluate whether the decrease in mitochondrial complexes expression was linked to reduced mitochondrial content we analyzed the expression of mitochondrial proteins porin and TIMM44 in liver total homogenates of L-OPA1 KO and control loxP mice. Our results showed an increase in mitochondrial porin and TIMM44 expression levels in L-OPA1 KO mice compared to control loxP mice (Figure 5.A-B).

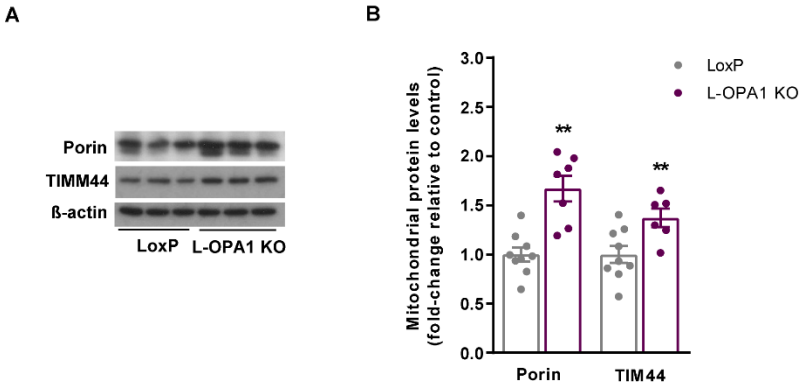

Figure 5. Hepatic depletion of OPA1 increases the abundance of some mitochondrial proteins. (A) Representative western blot of mitochondrial protein levels in liver homogenates of 8-week-old mice (B) Protein expression levels of Porin and TIMM44 (n=6-7). Data represent mean ± SEM. ** p<0.01 vs. loxP

Given the increase in some mitochondrial protein expression levels, we next evaluated whether the increase in these mitochondrial proteins content was associated to the activation of mitochondrial biogenesis in L-OPA1 KO by assessing peroxisome proliferator-activated receptor γ coactivator 1 α (PGC-1α) mRNA expression levels (Figure 6) and no activation was observed in livers of L-OPA1 KO mice compared to control loxP mice.

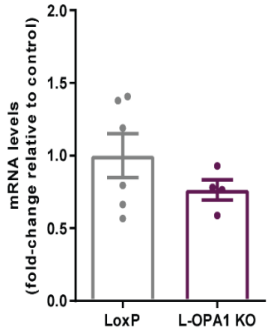

Figure 6. OPA1 loss-of-function does not activate mitochondrial biogenesis. (A) *pgc-1a* mRNA levels in the liver from loxP and and L-OPA1 KO mice (n=4). Data represent mean ± SEM.

3.1.2.4 mtDNA copy number and TFAM levels

Based on the link between OPA1 loss-of-function and mtDNA instability, we then determined liver mtDNA content by real-time PCR (section 7.2.3.6 in Materials and Methods). This quantification was carried out by the amplification of a conserved region in the mitochondrial 12S ribosomal RNA gene, between positions 1212 and 1352 in the mitochondrial genome and SdhA (subunit A of the complex II), encoded by the nuclear genome. Relative quantification analysis revealed a 55% reduction in the mitochondrial DNA/nuclear DNA (mtDNA/nDNA) ratio indicating that the repression of OPA1 in liver affects mtDNA copy number (Figure 7).

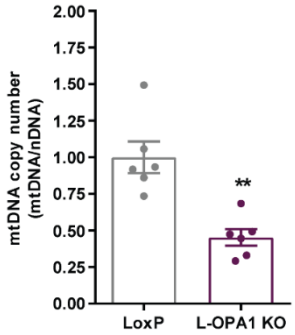

Figure 7. OPA1 depletion reduces mtDNA content in liver. mtDNA levels relative to nuclear DNA (n=6). Data represent mean ± SEM. ** $p<0.01$ vs. loxP control mice

TFAM is a key mediator of mitochondrial transcription as well as a participant in mitochondrial genome replication, by binding to mitochondrial DNA promoter. Unbound TFAM is rapidly degraded and therefore the amount of mtDNA directs the levels TFAM. Based on this, we next determined whether the reduction in mtDNA copy number affected TFAM induction by assessing the expression of TFAM protein. Protein expression levels

analysis demonstrated that OPA1-deficient livers showed a reduction of 32.4% in TFAM abundance (Figure 8.A-B).

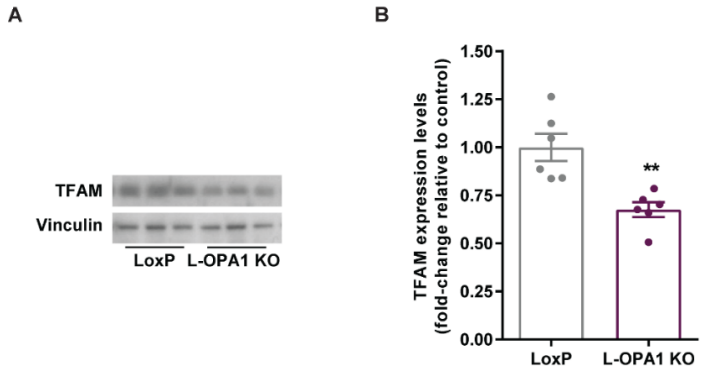

Figure 8. OPA1 depletion reduces TFAM abundance. (A) Representative western blot of TFAM protein levels in liver tissue homogenates of 8-week-old mice. (B) Protein expression levels of TFAM (n=6). Data represent mean ± SEM. ** $p<0.01$ vs. loxP control mice.

3.1.3 Histological studies

Histological inspection revealed cell death in the hepatic centrilobular area (around the central vein) in L-OPA1 KO livers (Figure 9; loxP – upper panel; L-OPA1 – lower panel).

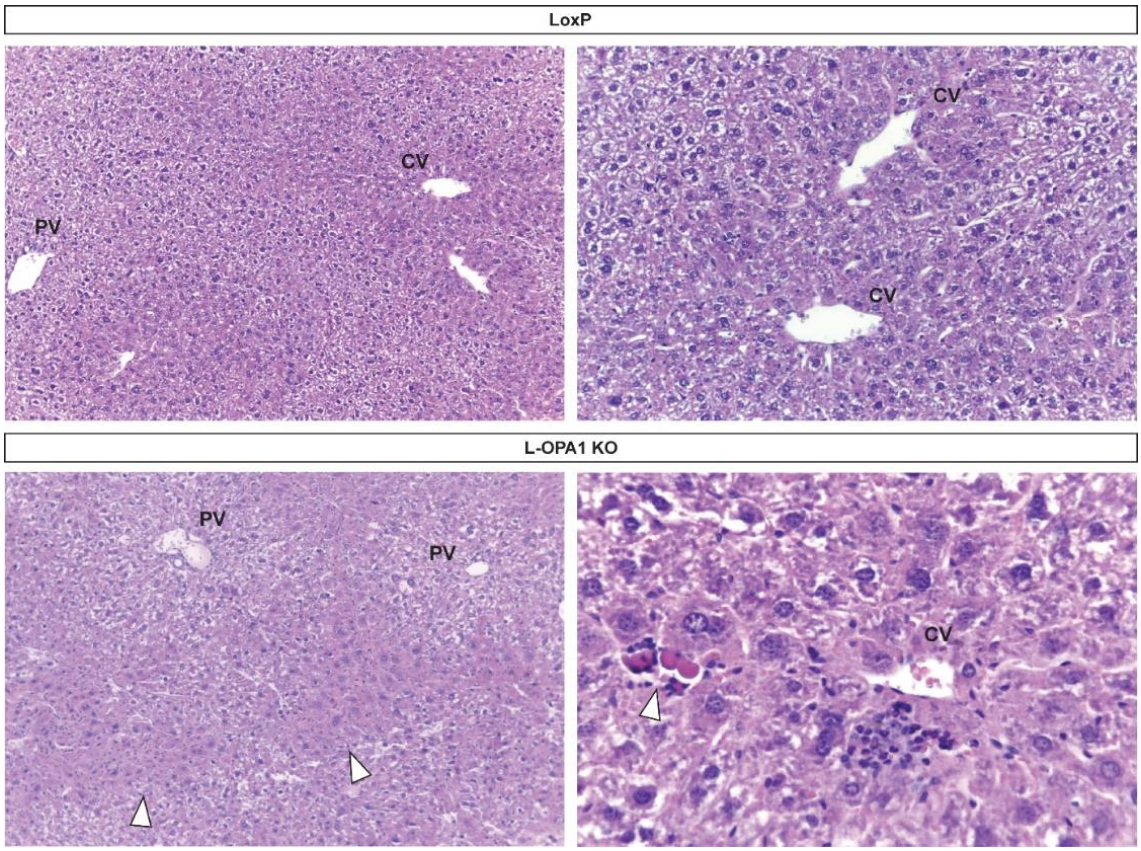

Figure 9. L-OPA1 KO mice present alterations in liver structure. Representative H/E staining of liver sections of loxP (upper panel) and L-OPA1 KO (lower panel). (CV) Central vein. (PV) Portal vein. Hepatic cell death indicated by arrows in both panels.

In order to assess whether apoptosis is the type of cell death detected in L-OPA1 KO, immunostaining against cleaved-caspase 3 was performed. Apoptosis was excluded to be relevant in the phenotype because cleaved caspase 3 detection was negative in both control loxP and L-OPA1 KO livers (Figure 10.A; loxP upper panel; L-OPA1 KO lower panel) which was corroborated by protein levels of cleaved caspase 3 (Figure 10.B).

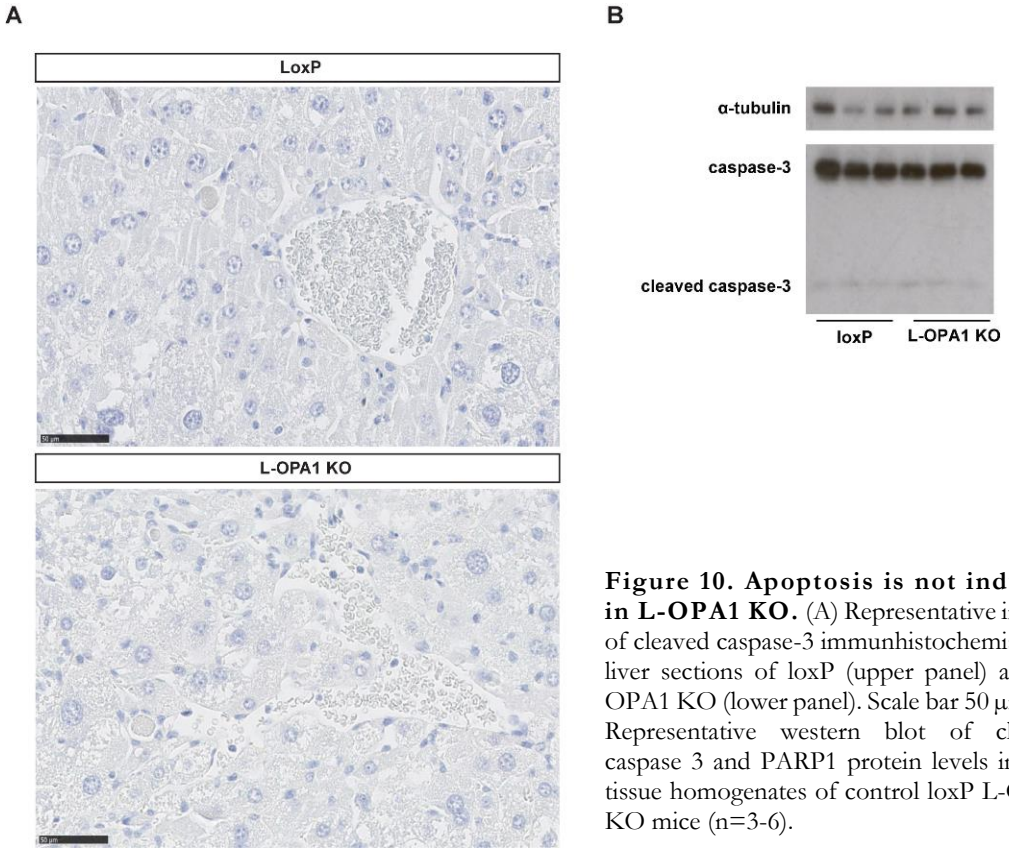

Figure 10. Apoptosis is not induced in L-OPA1 KO. (A) Representative images of cleaved caspase-3 immunhistochemistry in liver sections of loxP (upper panel) and L-OPA1 KO (lower panel). Scale bar 50 μm. (B) Representative western blot of cleaved caspase 3 and PARP1 protein levels in liver tissue homogenates of control loxP L-OPA1 KO mice (n=3-6).

These results suggested that another type of hepatic cell death is occurring, probably mitochondrial damage-induced hepatic necrosis. Ni et al. (2013) have demonstrated that hepatic mitochondrial damage triggered by the usage of drugs like acetaminophen, characterized by the inhibition complex I-dependent mitochondrial respiration and mtDNA damage, led to hepatocellular cell death in the central vein area of the liver. Moreover, the same research group have demonstrated that the hepatic cell death upon acute acetaminophen treatment caused mitochondrial fission.

The results obtained in this section indicate that OPA1 ablation in liver caused mitochondrial dysfunction by impairing mitochondrial oxidative capacity and decrease mtDNA copy number and TFAM levels. To determine whether mitochondrial dysfunction associated to the loss of function of OPA1 in liver affected metabolic homeostasis in L-OPA1 KO mice, we proceeded to perform phenotyping studies in these mice.

3.2 Study of the metabolic impact caused by hepatic ablation of OPA1

To carry out the metabolic characterization of L-OPA1 KO mice, we performed a series of metabolic screening tests in chow- and high-fat diet (HFD) such as weekly body weight control, glucose tolerance test (GTT) and insulin tolerance test (ITT), food intake and indirect calorimetry. Since at 8 weeks of age L-OPA1 KO demonstrated consistent mitochondrial dysfunction this time point was chosen for all subsequent metabolic analyses subjected to a normal chow diet.

3.2.1 General phenotyping of L-OPA1 KO mouse model in chow diet

3.2.1.1 Body mass parameters and food intake

Body weight was measured every 2 weeks until the animals reached 24 weeks of age. L-OPA1 KO body weight was undistinguishable from that of loxP mice, as well as lean and fat mass distribution (Figure 11. A-B). Food intake was assessed for 7 days and under these conditions dietary consumption was similar in control loxP and L-OPA1 KO mice (Figure 11. C).

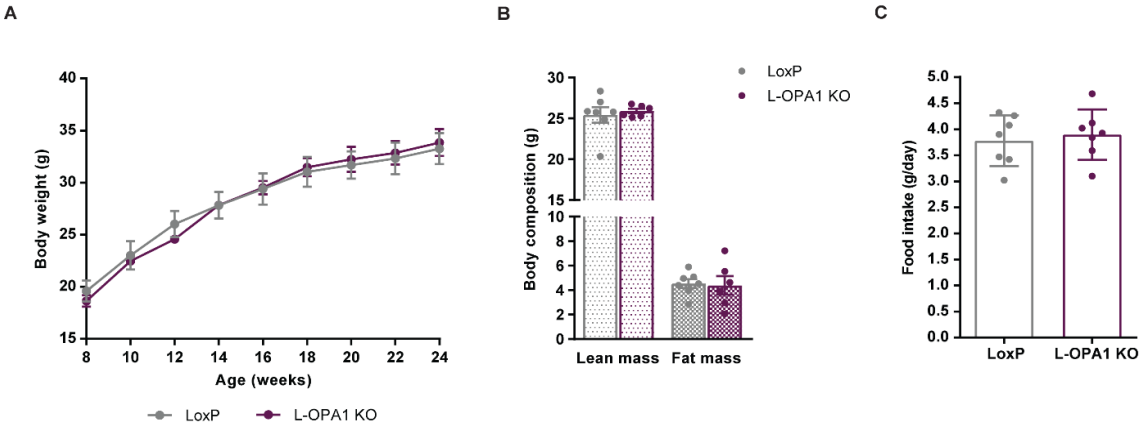

Figure 11. L-OPA1 KO mice present no changes in body weight or food intake. (A) Mice body weight measurements between 8 and 24 weeks of age (n=7-6). (B) Body composition measured by EchoMRI at 16 weeks of age. Data as grams of weight and represent mean ± SEM. (C) Food consumption as grams of intake by day (7 consecutive days; n=7). Data represent mean ± SEM.

3.2.1.2 Glucose Tolerance and Insulin Sensitivity Tests

To determine whether the mitochondrial dysfunction associated to the loss of function of OPA1 in liver affected glucose homeostasis in L-OPA1 KO mice we challenged the animals with a glucose tolerance test (GTT), which not only assesses the disposal of a glucose load administered via intraperitoneal injection, but it also provides information about insulin secretion (Ayala et al. 2010). Following an overnight fasting (16h), a 2g/kg glucose load was administered, and blood glucose was measured over a span of 2 hours at 5, 15, 30, 60, 90 and 120-minute time-points. Overnight fasting nearly depletes liver glycogen stores in mice, which allows reducing variability in baseline blood glucose and it gives more accuracy on glucose utilization.

The results revealed that regardless no body weight changes, L-OPA1 KO mice showed enhanced glucose handling (Figure 12.A). Differences in glucose tolerance can often be explained by altered plasma insulin levels which led us to analyzing insulin levels during the GTT. To determine plasma insulin-levels we performed an Enzyme-linked immune-sorbent assay (ELISA) using plasma samples from 0, 15, 30 and 60-minute time-points and observed the presence of reduced plasma insulin levels in L-OPA1 KO compared to control loxP mice (Figure 12.B). These finding indicate that OPA1 loss-of-function in liver results in an improvement of the glucose handling capacity and a higher responsiveness to insulin.

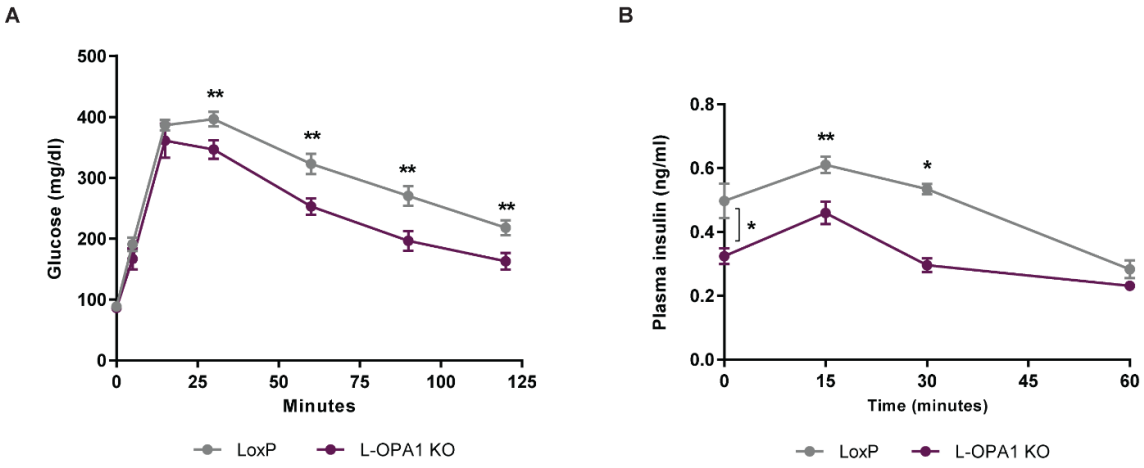

Figure 12. L-OPA1 KO mice display improved glucose handling in a lower circulating insulin context. (A) 16h-fasted 8-week-old male mice were subjected to Glucose Test Tolerance (GTT) (2g/kg; n=6). (B) Plasma insulin levels during the test (n=6). Data represent mean ± SEM.* $p<0.05$, ** $p<0.01$ vs. control loxP mice.

Because L-OPA1 KO mice showed higher glucose tolerance characterized by lower plasma insulin levels, we decided to further evaluate the responsiveness to insulin by performing an ITT which gives indication of whole-body insulin action. To this end, after a 4h-fast we administered a maximal dose of insulin, 1U/Kg, and monitored glucose levels over 1 hour at 0, 15, 30, 45 and 60-minute time-points. Under those conditions, L-OPA1 KO showed a higher tolerance to insulin compared to control loxP mice, suggesting an enhanced insulin responsiveness (Figure 13.A-B).

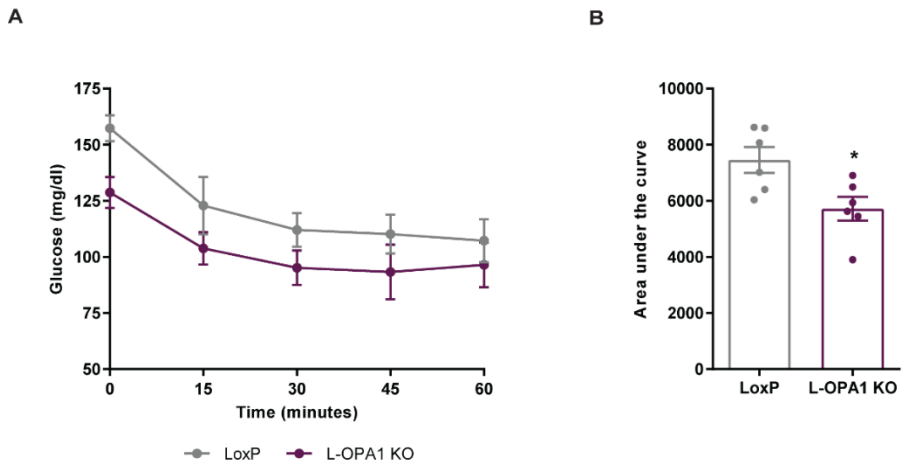

Figure 13. L-OPA1 KO mice exhibit a higher response to insulin. (A) 4h-fasted 10-week-old male were insulin stimulated and subjected to Insulin Test Tolerance (ITT). (B) Area under the curve (0.5U/kg; n=6). Data represent mean ± SEM. * $p<0.05$ vs control loxP mice.

3.2.1.3 Energy expenditure

Alterations in glucose utilization often result from changes in energy balance, therefore investigating whole-body energy homeostasis is essential to better understanding glucose metabolism. Since L-OPA1 KO showed higher glucose tolerance and better response to insulin but no changes in food intake, we next assessed the energy metabolism of 12week-old mice by indirect calorimetry. To do so, the animals were placed in ventilated and open-circuit system cages through which a flow of fresh air is passed, and the system collects and mixes the expired air, measures the flow rate and analyzes the gas concentration of the incoming and outgoing air for both O_2 and CO_2. Thus, in indirect calorimetry, energy expenditure is calculated based on the amount of oxygen consumed and carbon dioxide produced.

Energy expenditure analysis revealed that L-OPA1 KO mice showed similar oxygen consumption (VO_2) and carbon dioxide (VCO_2) to that of the control loxP mice (Figure 14.A-B). In this line, no changes in energy expenditure, whole body glucose oxidation and ambulation were observed in L-OPA1 KO compared to control loxP mice (Figure 14.C-F).

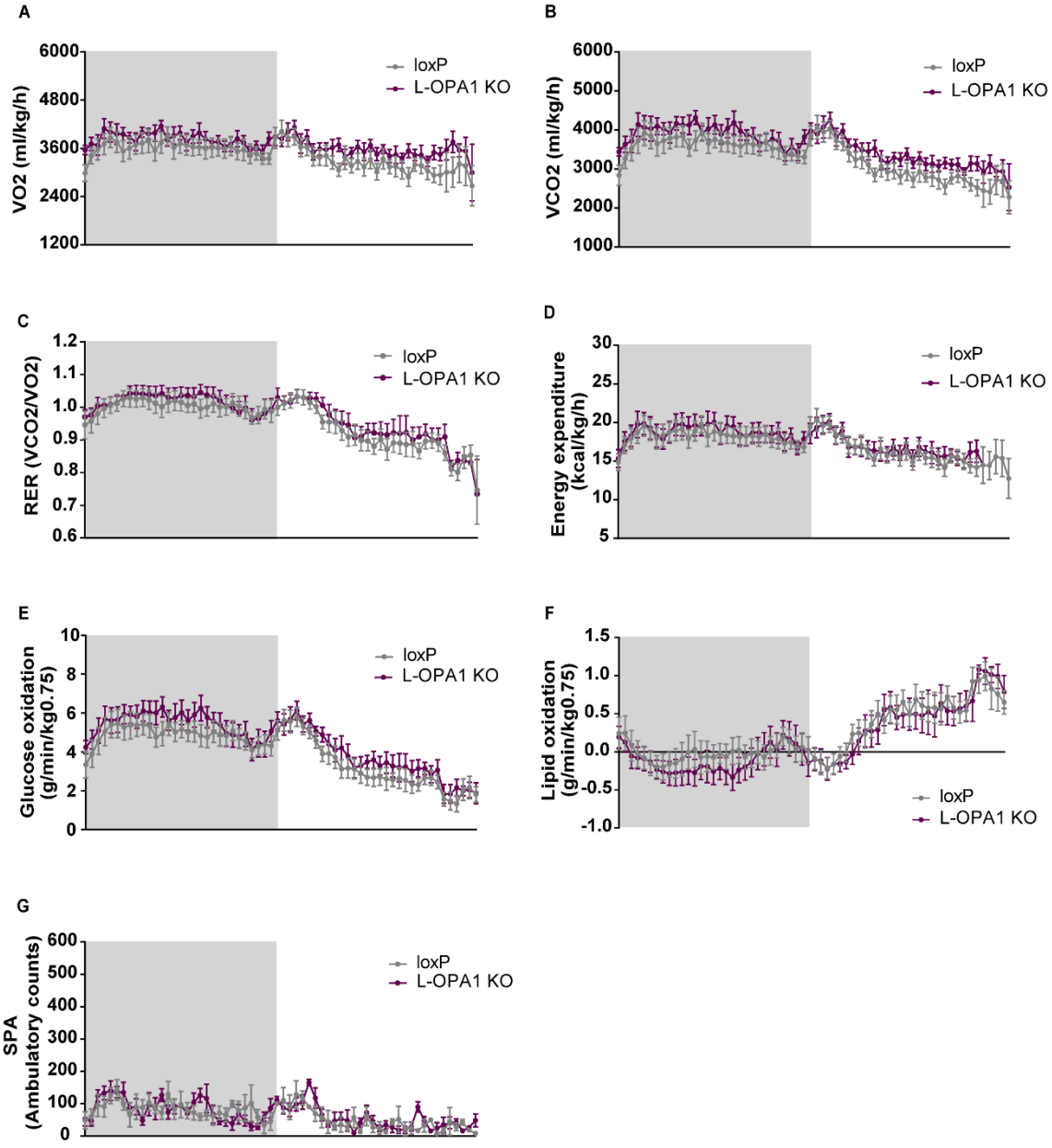

Figure 14. Indirect calorimetry revealed no changes in energy metabolism in L-OPA1 KO. Indirect calorimetry data points were collected each 20 minutes every 24h, **from** 7pm to 7pm, for 3 days. The grey area corresponds to the dark period (7pm to 7am). Average dark-light period (A) oxygen consumption, (B) carbon dioxide production, (C) Ratio Exchange Rate (RER; VCO2/VCO2) (D) Energy Expenditure {=1,44xVO2x (3,815+1,232xRER)}, (E) Glucose Oxidation {=[(4,545xVCO2) (3,205xVO2)]/1000}, (F) Lipid Oxidation {=[1,672x(VO2-VCO2)]/1000} and (G) Spontaneous physical activity represented by ambulatory movement counts. Data represent mean ± SEM. 12-week-old mice were used (n=8).

3.2.1.4 Biochemical parameters

To better characterize the metabolic alterations associated to the deletion of OPA1 in the liver, we measured several biochemical parameters in fed and fasted-state. Upon 16h-fasting, glucose, insulin and glucagon levels were measured. Despite no changes in plasma glucose levels we observed that L-OPA1 KO mice presented reduced levels of plasma insulin in comparison to the loxP control mice (Figure 15 - left and middle panel). Also, the biochemical analysis showed that glucagon levels were not different between control loxP and L-OPA1 KO mice (Figure 15 - right panel).

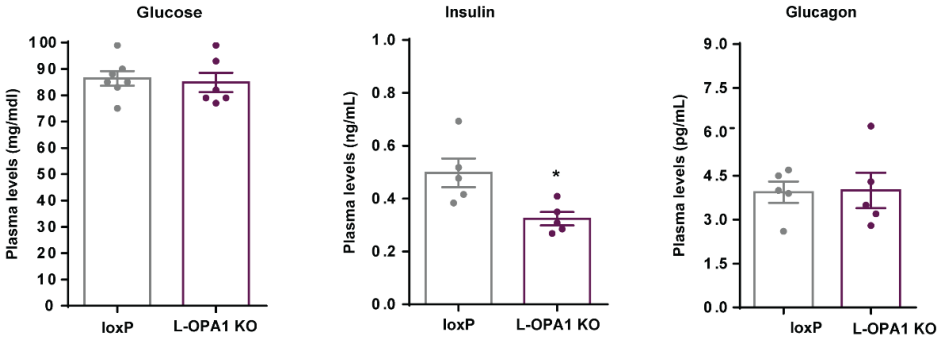

Figure 15. Plasma levels of glucose, insulin and glucagon in L-OPA1 KO and control loxP mice. Circulating levels of glucose, insulin and glucagon from 8week-old 16h-fasted mice. n=5-6). Data represent mean ± SEM. * $p<0.05$ vs control loxP mice.

On a fed metabolic-state, L-OPA1 KO mice did not show changes in circulating triglycerides, though cholesterol plasma levels were decreased. NEFAs and β-hydroxybutyrate circulating were significantly higher in L-OPA1 KO mice compared to the controls (Figure. 16).

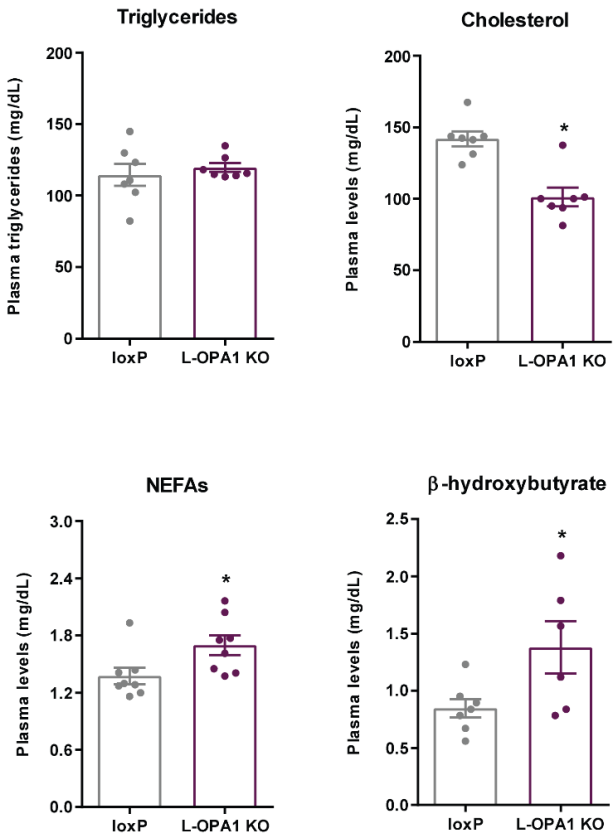

Figure 16. Plasma measurements in L-OPA1 KO mice in fed-state. Circulating levels of triglycerides (left-upper panel), cholesterol (right-upper panel), NEFAs (left-lower panel) and β-hydroxybutyrate (right-lower panel) of 8week-old mice (n=6-8). Data represent mean ± SEM. * $p<0.05$ vs control loxP mice.

3.2.1.5 Studies of energy expenditure and lipid handling in fasted state

We also assessed energy expenditure in mice subjected to an overnight-fasting. Similarly to the results on fed-state, no changes in oxygen consumption/carbon dioxide production, energy expenditure or substrates oxidation were observed in L-OPA1 KO (Figure 17.A-F). Thus, based on this study, the ameliorated glucose handling in L-OPA1 KO mice in chow diet cannot be explained by alterations in energy expenditure.

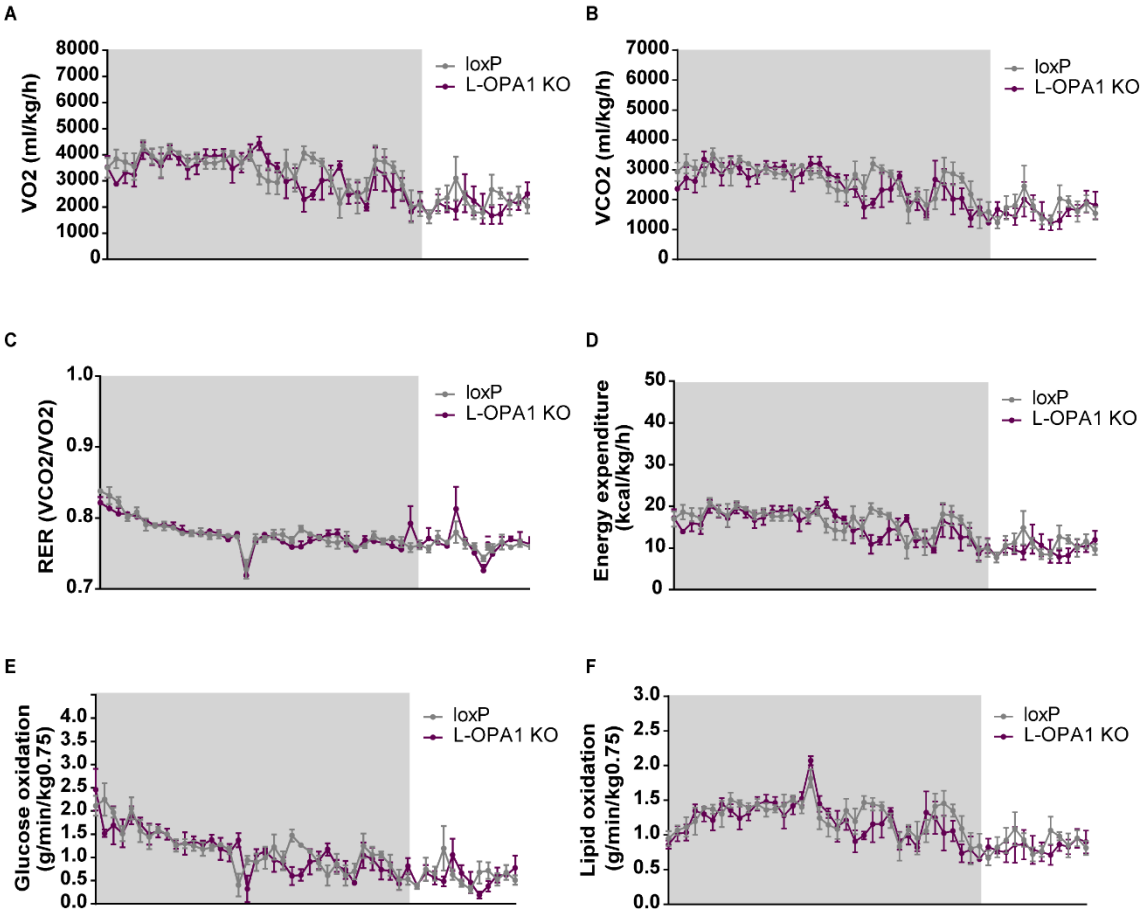

Figure 17. Indirect calorimetry revealed no changes in energy metabolism during fasting. Indirect calorimetry data points were collected each 20 minutes during 16h, from 7pm to 11am. The grey area corresponds to the dark period (7pm to 7am). Average dark-light period (A) oxygen consumption, (B) carbon dioxide production, (C) Ratio Exchange Rate (RER; VCO2/VCO2) (D) Energy Expenditure {=1,44xVO2x (3,815+1,232xRER)}, (E) Glucose Oxidation {=[(4,545xVCO2) (3,205xVO2)]/1000}, (F) Lipid Oxidation {=[1,672x(VO2-VCO2)]/1000}. Data represent mean ± SEM. 12-week-old mice were used (n=8).

In order to understand how hepatic lipid metabolism is affected by the improved glucose homeostasis and response to insulin, we have measured relevant plasma metabolites in overnight-fasted. Under fasted conditions, L-OPA1 KO mice presented a significant decrease in circulating triglycerides, cholesterol and β-hydroxybutyrate in parallel with an increase in non-esterified fatty acids (NEFAs) compared to the controls (Figure. 18).

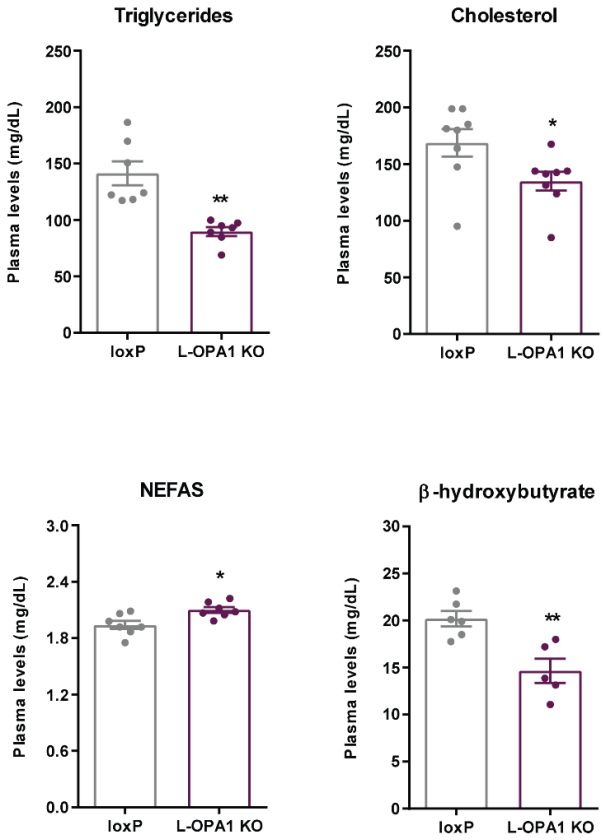

Figure 18. Biochemical plasma measurements in L-OPA1 KO mice in fasted-state. Circulating levels of triglycerides (left-upper panel), cholesterol (right-upper panel), NEFAs (left-lower panel) and β-hydroxybutyrate (right-lower panel) of 8week-old mice (n=6-8). Data represent mean ± SEM. * $p<0.05$ vs control loxP mice.

3.2.2 General phenotyping of L-OPA1 KO mouse model challenged by a high-fat diet

To further challenge the enhanced capacity of glucose handling of L-OPA1 KO mice, we decided to expose the animals to a chronic lipid overflow and evaluate glucose homeostasis. At 6 weeks of age, we introduced the animals into a high-fat content diet (60% kcal% fat) for a duration of 16 weeks, described as the standard procedure for high-fat diet (HFD) studies (Wang and Liao 2012).

3.2.2.1 Body mass parameters and food intake

Body weight measurements were performed every two weeks until the endpoint of the experiment (16 weeks). We observed that L-OPA1 KO mice were significantly leaner compared to control loxP and the difference in weight gain was evident along the diet

duration-time (Figure 19.A-B), indicating that L-OPA1 KO mice are protected against diet-induced obesity.

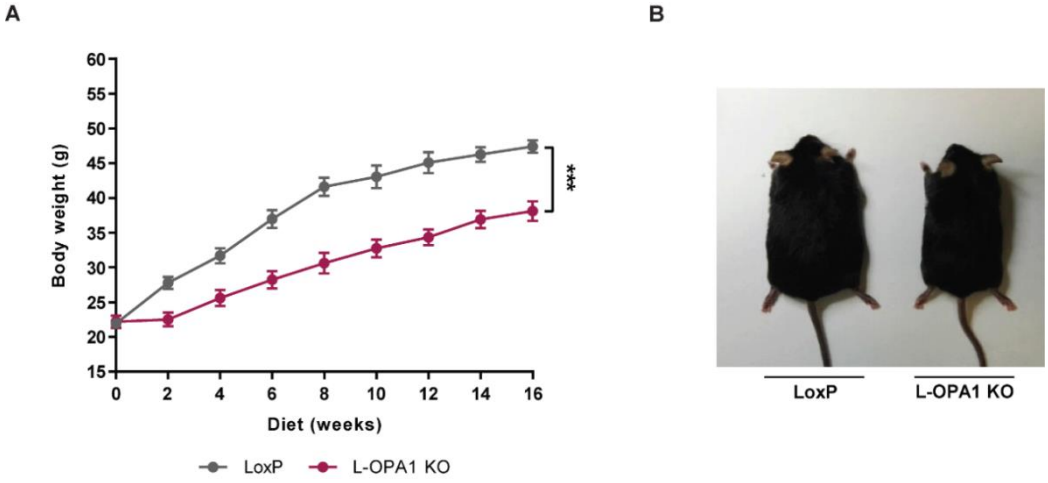

Figure 19. L-OPA1 KO mice are protected against diet-induced obesity. (A) Picture of control loxP and L-OPA1 KO at 16 weeks of HFD. (B) Mice body weight measurements every 2 weeks during 16 weeks of diet (n=6-8). (C) Body composition measured by EchoMRI at 16 weeks of diet. *** p<0.001 vs. control loxP mice.

As L-OPA1 KO lower body weight was evident as early as at 2 weeks of diet we reasoned that at 8 weeks we would get valuable information on glucose homeostasis. Therefore, at 8 weeks of diet, we measured body fat and lean mass, by ECO-MRI technology, food intake and fat depots weight in control loxP and L-OPA1 KO mice (Figure 20.A-C).

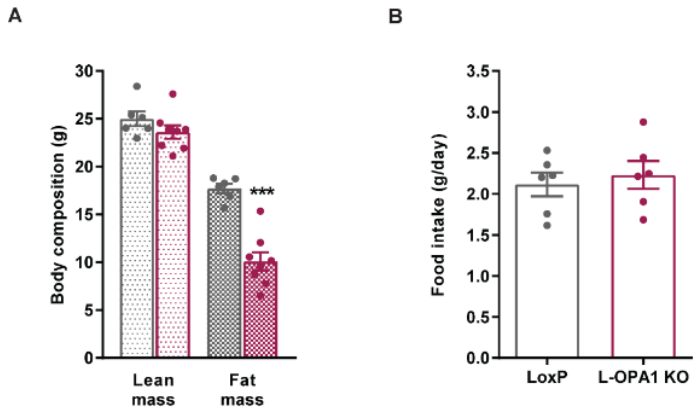

Figure 20. Fat mass content is lower in L-OPA1 KO despite no differences in food intake. Body composition measured by EchoMRI at 16 weeks of diet. (B) Food consumption as grams of intake by day (7 consecutive days; n=7). Data represent mean ± SEM. *** p<0.001 vs. control loxP mice.

L-OPA1 KO revealed a 43% reduction in fat mass composition compared to the control loxP in keeping with the lower body weight gain observed. Food intake was not different between control loxP mice and L-OPA1 KO mice. Our results indicate that L-OPA1 KO mice are protected against diet-induced obesity.

3.2.2.2 Glucose Tolerance and Insulin Sensitivity Tests

To further examine the capacity of glucose handling of L-OPA1 mice upon lipid overload, we challenged the animals to a GTT, as described before in point 4.2.1.2. The results demonstrated that L-OPA1 KO mice was able to maintain their enhanced capacity to handle glucose even when stimulated with a lipid overload (Figure 21.A). Surprisingly, on HFD fasting glucose and plasma insulin levels of L-OPA1 KO mice were lower comparing to loxP control mice (Figure 21.B). This suggests that liver-specific OPA1 deletion caused an enhanced insulin sensitivity.

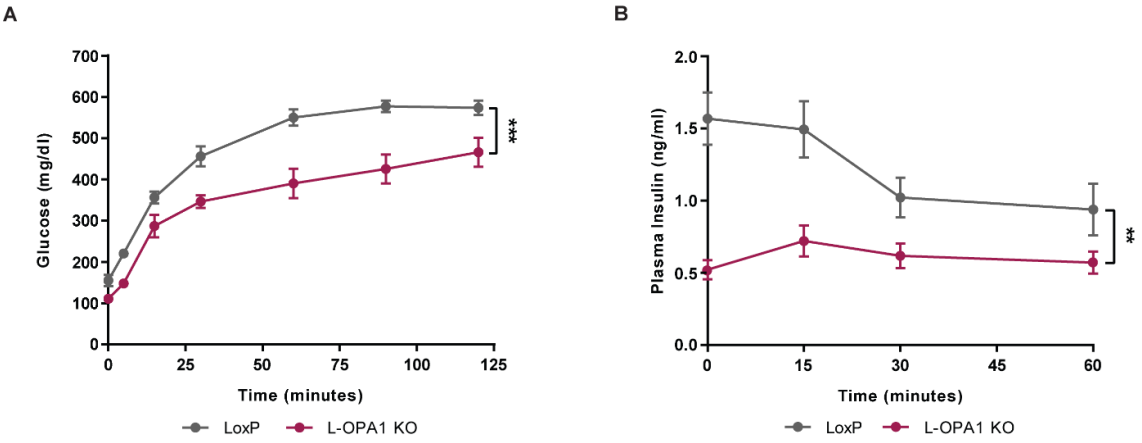

Figure 21. L-OPA1 KO mice maintain enhanced glucose tolerance on HFD (A) 16h-fasted male mice at 8 weeks on a high-fat diet were subjected to Glucose Test Tolerance (GTT) (2g/kg; n=6). (B) Plasma insulin levels during the test (n=6). Data represent mean ± SEM.** $p<0.01$, *** $p<0.001$ vs. control loxP mice.

To further confirm the higher responsiveness to insulin of L-OPA1 KO on HFD, 2 weeks after performing the GTT, we carried out an ITT to assess whole-body insulin action, as described in point 4.2.1.2. by injecting the animals with a with a dose of insulin of 2U/Kg considering that animals on HFD develop intolerance to insulin. ITT results showed that L-OPA1 KO mice were more responsive to insulin compared to control loxP mice,

indicating that L-OPA1 KO mice are protected against diet-induced insulin resistance (Figure 22).

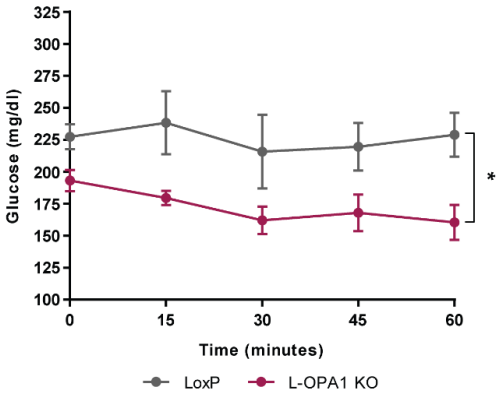

Figure 22. L-OPA1 KO mice exhibit a higher response to insulin. (A) 4h-fasted male mice on high-fat diet for 10 weeks were insulin stimulated and subjected to Insulin Test Tolerance (ITT), Area under the curve (1U/kg; n=6). Data represent mean ± SEM. * $p<0.05$ vs. control loxP mice.

3.2.2.1 Energy expenditure studies

Given the fact that, L-OPA1 KO mice under HFD regimen were leaner and more tolerant to glucose with no alterations on food intake, which suggested a differential energy expenditure rate, we next assessed whole-body energy homeostasis by indirect calorimetry, as described before on section 4.2.1.3, at 12 weeks of diet. Indirect calorimetry analysis revealed that L-OPA1 KO mice showed a higher VO_2 and VCO_2 rates compared to that of the control loxP mice (Figure 23.A-B). In this line, L-OPA1 KO mice exhibited augmented energy expenditure and rather oxidized glucose over lipid to meet their energetic demands (Figure 34.C-D). Possibly, these alterations are associated to a higher locomotor activity observed in L-OPA1 KO (Figure 23.E-F).

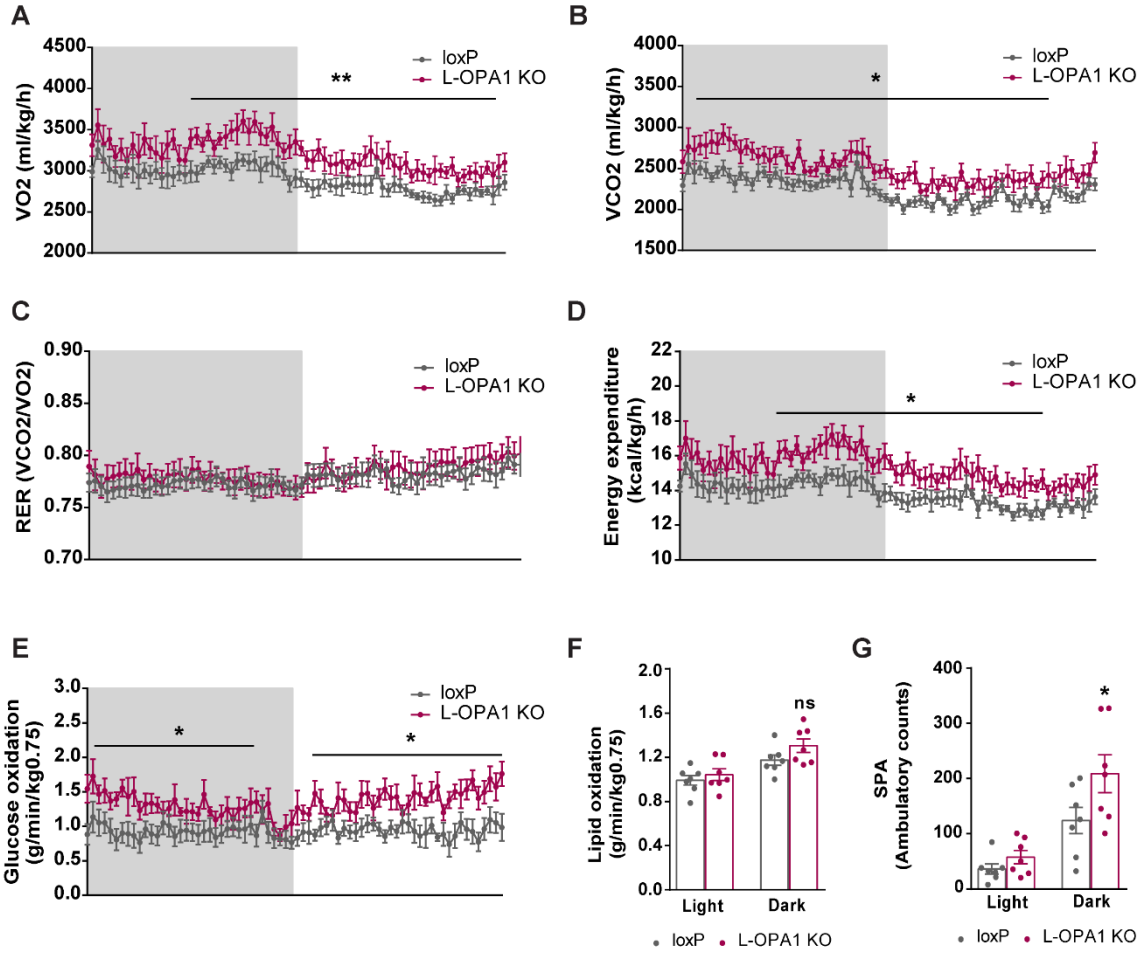

Figure 23. Indirect calorimetry revealed altered energy metabolism in L-OPA1 KO subjected to HFD. Indirect calorimetry data points were collected each 20 minutes every 24h, from 7pm to 7pm, for 3 days. The grey area corresponds to the dark period (7pm to 7am). Average dark-light period (A) oxygen consumption, (B) carbon dioxide production, (C) Energy Expenditure {=1,44xVO2x (3,815+1,232xRER)}, (D) Glucose Oxidation {=[(4,545xVCO2) (3,205xVO2)]/1000} and (E-F) Physical activity represented by movement counts. Data represent mean ± SEM. Mice were used at 12-week-diet (n=8).

3.2.2.2 Biochemical parameters

To further characterize the metabolic adaptation observed in L-OPA1 KO mice exposed to HFD challenge, we have measured several biochemical parameters in fed and fasted-state. Upon 16h-fasting, glucose, insulin and glucagon levels were measured. Our analysis showed that plasma glucose and insulin levels were significantly lower in comparison to the loxP control mice (Figure 24- left and middle panel). Also, the biochemical analysis showed that glucagon levels were not different between control loxP and L-OPA1 KO mice, as observed before in chow-diet (Figure 24- right panel).

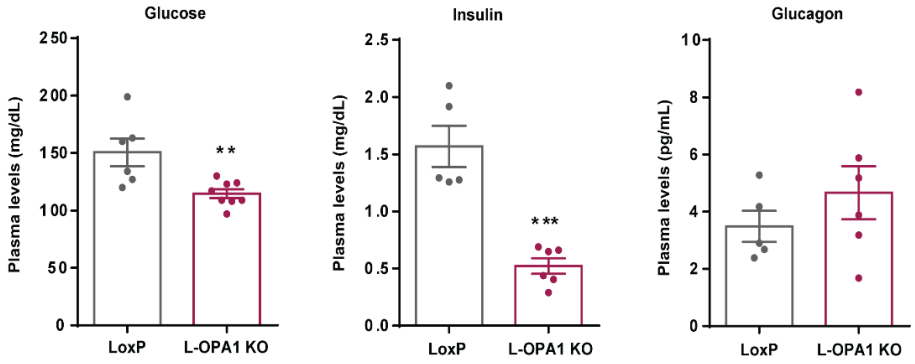

Figure 24. Plasma levels of glucose, insulin and glucagon in L-OPA1 KO mice on HFD. Circulating levels of glucose, insulin and glucagon NEFAs from 8week-old 16h-fasted mice n=5-8). Data represent mean ± SEM., ** p<0.01 *** p<0.001 vs control loxP mice.

The results of the basic metabolic phenotyping of L-OPA1 KO mice on HFD demonstrated that OPA1 loss-of-function in liver on those conditions exacerbates the improved metabolic phenotype which protected OPA1-deficient mice against diet-induced obesity and insulin resistance.

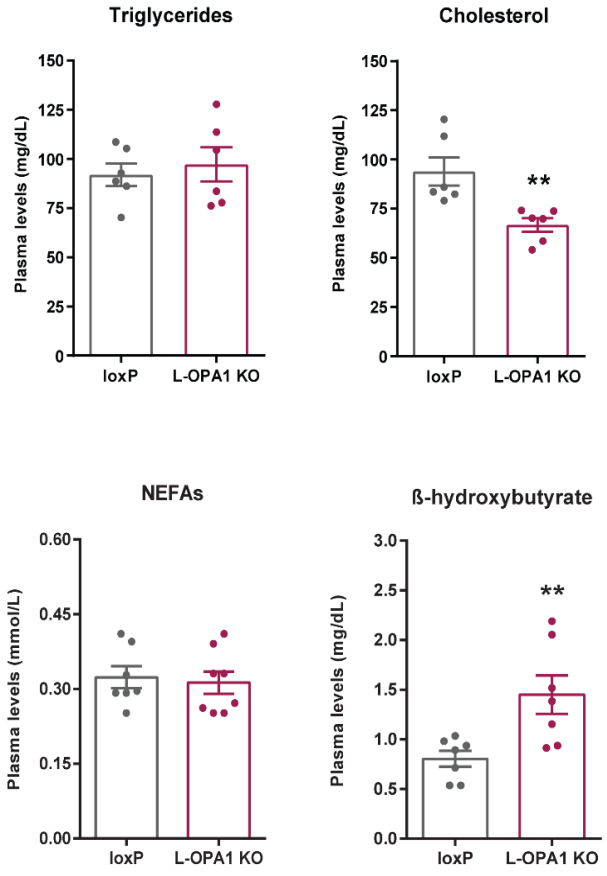

Figure 25.

Figure 25. Plasma measurements in L-OPA1 KO mice on HFD. Circulating levels of triglycerides (left-upper panel), cholesterol (right-upper panel), NEFAs (left-lower panel) and β-hydroxybutyrate (right-lower panel) of 8week-old mice (n=6-8). mice. n=6-11). Data represent mean ± SEM. * p<0.05, ** p<0.01 vs control loxP mice.

3.2.2.3 Studies of energy expenditure and lipid handling in fasted state

In order to understand how hepatic lipid metabolism is affected by the improved insulin sensitivity and glucose homeostasis on HFD, we measured relevant plasma metabolites in overnight fasted mice. Under fast-conditions, L-OPA1 KO mice presented a significant increase in circulating triglycerides and a reduction in cholesterol circulating levels (Figure 26 – right and left-upper panels). An increase in non-esterified fatty acids (NEFAs) was also observed in L-OPA1 KO mice in parallel with no changes in β-hydroxybutyrate levels (Figure 26 - right and left-lower panels).

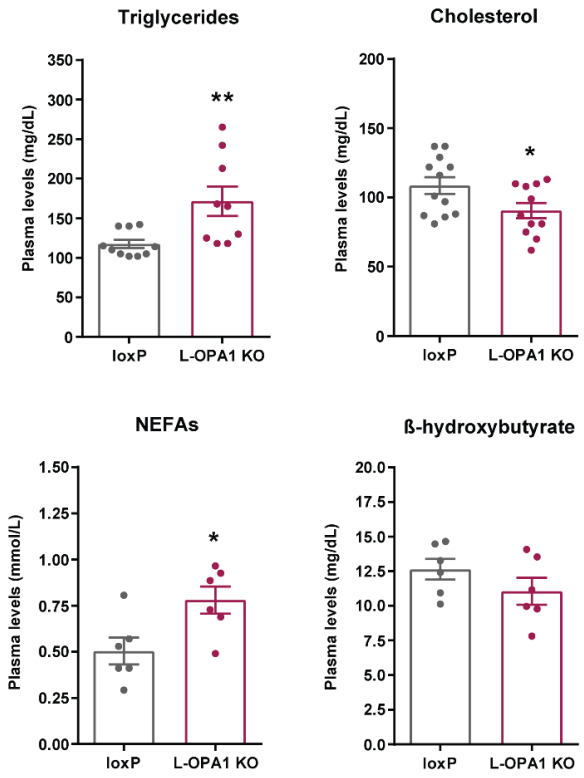

Figure 26. Plasma measurements in L-OPA1 KO mice on HFD on fasting. Circulating levels of triglycerides (left-upper panel), cholesterol (right-upper panel), NEFAs (left-lower panel) and β-hydroxybutyrate (right-lower panel) of 8week-old fasted mice (n=6-8). mice. n=6-11). Data represent mean ± SEM. * p<0.05, ** p<0.01 vs control loxP mice.

Given the elevated energy expenditure for L-OPA1 KO mice in the previous experiment, we sought to accentuate this phenomenon further by subjecting the mice to an overnight fasting. Although not as accentuated as in fed-state, L-OPA1 KO mice also revealed higher oxygen consumption and carbon dioxide production during 16h-fasting (Figure 28.A-B). During fasting, L-OPA1 KO mice also showed a higher energy consumption associated to a preference for glucose over lipid oxidation and curiously, to a higher locomotor activity (Figure 27.C-F). Several studies have demonstrated that physical activity is higher during fasting due to increased motivation to find food (reference). Our results suggest that liver-specific OPA1 deletion challenged by a lipid overload may enhance the motivation to find food possibly activity-induced thermogenesis during fasting, which could explain the enhanced glucose tolerance and lower body weight in L-OPA1 KO on HFD.

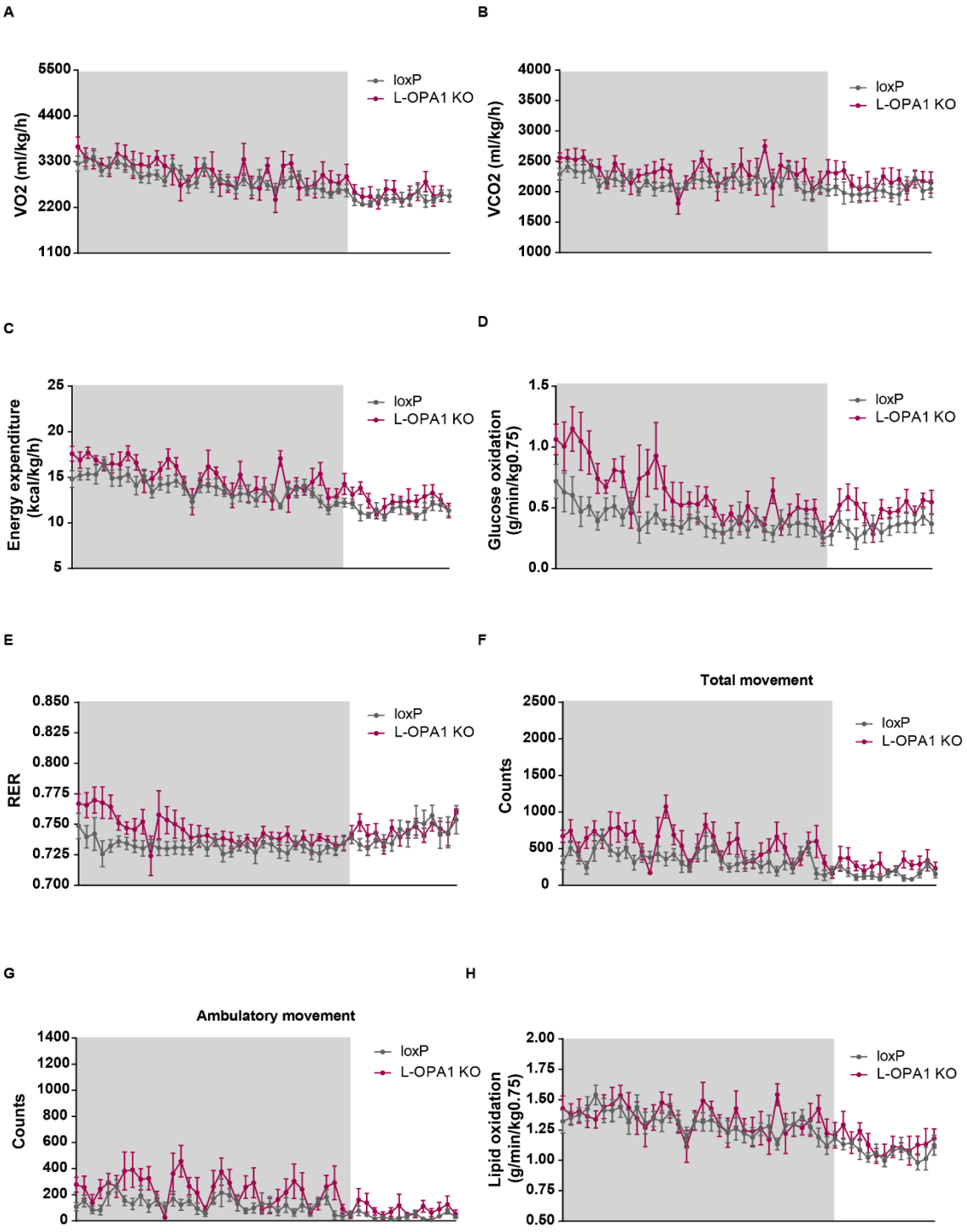

Figure 27. Indirect calorimetry revealed enhanced energy metabolism during fasting on HFD. Indirect calorimetry data points were collected each 20 minutes during 16h, from 7pm to 11am. The grey area corresponds to the dark period (7pm to 7am). Average dark-light period (A) oxygen consumption, (B) carbon dioxide production, (C) Energy Expenditure {=1,44xVO2x (3,815+1,232xRER)}, (D) Glucose Oxidation {=[(4,545xVCO2) (3,205xVO2)]/1000}, (E) Ratio Exchange Rate (RER; VCO2/VCO2), (F-G) Physical activity represented by movement counts and (H) Lipid Oxidation {=[1,672x(VO2-VCO2)]/1000}. Data represent mean ± SEM. Mice were used at 12-week-diet (n=8).

3.3 Identification of the key players responsible for the metabolic phenotype associated to OPA1 deficiency in liver

3.3.1 Examination of differential gene expression linked to liver specific OPA1 deletion

To identify the cellular processes that participate in the metabolic adaptation induced by the ablation of OPA1 in liver, transcriptomic analysis on livers of L-OPA1 KO and loxP control mice by RNASeq was performed. A total of 2,059 unique genes were differentially expressed (fold-change > 1.5, adjusted p-value < 0.01), of those 1,214 (59%) were significantly upregulated and 845 (41%) were significantly downregulated.

Gene set enrichment analysis (GSEA) revealed that loss of OPA1 in liver resulted in altered gene expression patterns in L-OPA1 KO compared with loxP control mice. In the top upregulated pathways, an enrichment in stress response pathways was observed, amongst those the UPRer and the activation of mitochondrial stress-associated genes (mt-stress genes). Mitochondrial stress-associated genes (mt-stress) refer to a mitochondrial stress signature that is shared by many mitochondrial stress conditions in cellular and animal models and that is characterized primarily by the activation of amino acid biosynthesis pathways (Quirós et al. 2017). Of those downregulated, as expected, an enrichment in oxidative capacity related pathways was observed, indicating the presence of mitochondrial dysfunction provoked by the ablation of OPA1 (Figure 28).

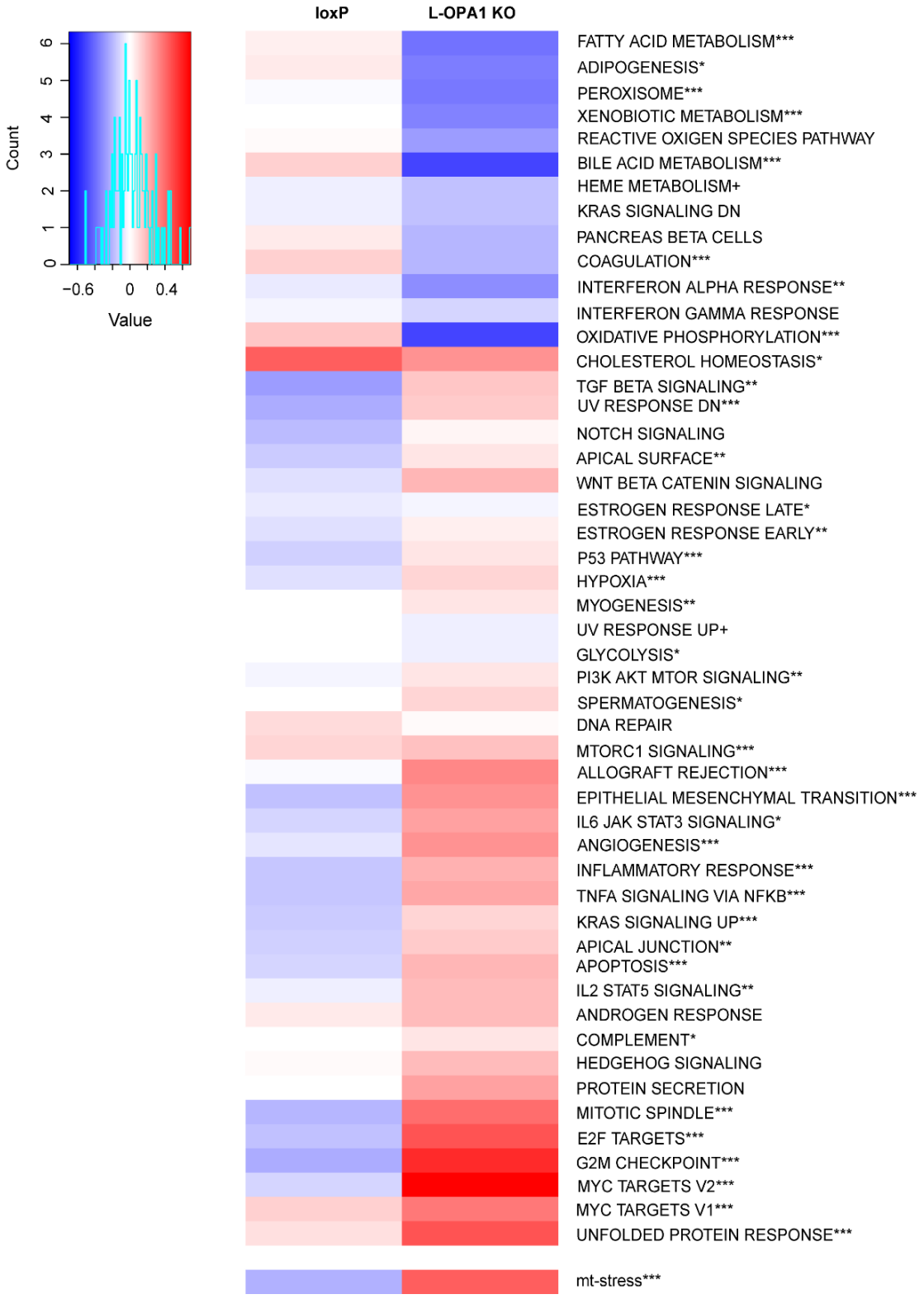

Figure 28. Gene transcripts are differentially altered in L-OPA1-KO mice. PreRanked algorithm Gene Set Enrichment Analysis of 2059 transcripts identified differentially enriched and depleted Broad Hallmarks gene sets in L-OPA1 KO mice (chow-diet; n=6). Data represent ranked mean of log2 fold-change. p-value after Bonferroni correction. * $p<0.05$, ** $p<0.01$, *** $p<0.001$ vs control loxP mice.

Next, we analyzed the up-regulated mt-stress associated genes in livers of L-OPA1 KO mice. Quirós et al. (2017) have recently described a mitochondrial stress signature that is composed by 49 genes. Here we found that 23 out of the 49 mt-stress associated genes were up-regulated with a FDR < 0.01 in L-OPA1 KO mice (Figure 29.A). Notably, among those 23 genes, we observed the activation of genes related to amino acid biosynthesis, in particular, the key enzymes involved in asparagine and serine biosynthesis, one carbon (1C) metabolism, amino acid transporters and key enzymes involved in aminoacyl-tRNAs biosynthesis (Figure 28.B).

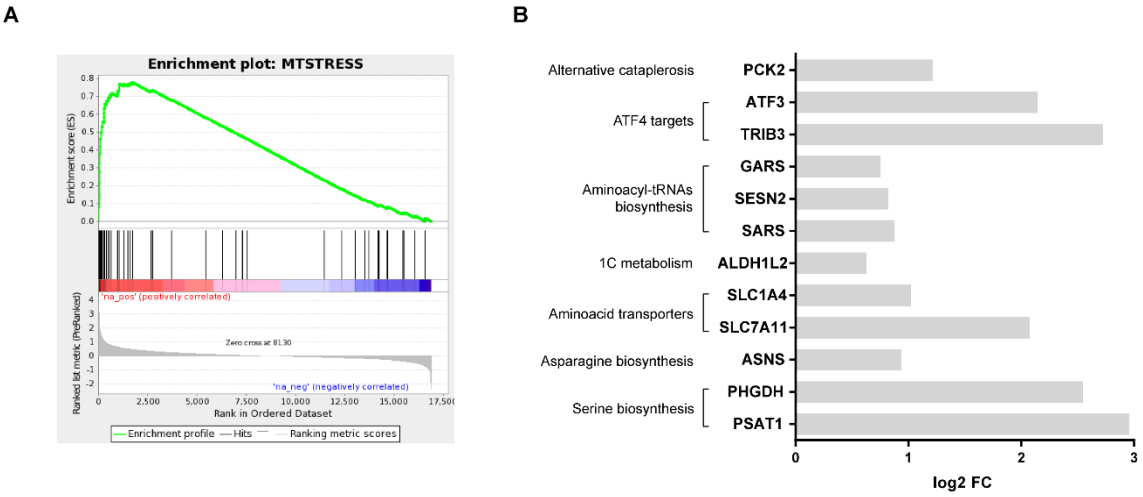

Figure 29. OPA1 deletion in liver leads to activation of mt-stress associated genes. (A) Mt-stress enrichment score plot from GSEA data. (B) Bar plots showing enrichment scores (log2 fold change (FC) relative to control loxP mice) of genes involved in amino acid biosynthesis filtered by mt-stress genes with FDR < 0.01. n=6, livers of 8-weeks old mice on chow diet were used.

The activation of mt-stress associated genes together with our data demonstrating that the deficiency of OPA1 in liver led to cristae disorganization associated to unbalanced OxPhos subunits content and mtDNA deletion, all linked to perturbations in mitochondrial proteostasis, encouraged us to further assess the UPRmt that is activated by mitochondria in an attempt to alleviate possible proteostasis defects. We analyzed individual gene expression of the mediator genes of UPRmt and outputs. The transcription factor ATF5, the UPRmt effectors mitochondrial heat-shock protein 70kDa (mtHSP70) and Lon Peptidase 1 (LONP1), and the metabolic regulator Fibroblast Growth Factor 21 (FGF21) were differentially regulated in L-OPA1 KO in comparison to control loxP mice. Activation of ClpP protease and the chaperonins HSP60 and HSP10 was not observed in L-OPA1 KO,

suggesting that the mitochondrial stress caused the deletion of OPA1 in liver is being handled via AT5-dependent UPRmt activation (Table 1).

Table 1. Individual gene expression

Gene	Encoding	FC > 1.5	p-value	Adjusted p-value
atf5	ATF5	1.99	4.68E-14	4.01E-12
atf4	ATF4	1.14	0.04	0.11
hspa9	mtHSP70	1.71	1.70E-15	1.99E-13
lonp1	LONP1	1.98	1.47E-12	9.45E-11
fgf21	FGF21	3.79	8.31E-10	2.93E-08
clpp	ClPp	1.10	0.12	0.24
hspd1	HSP60	1.24	0.06	0.15
hspe1	HSP10	1.02	0.83	0.90

Previously in our lab. Rodriguez et al. (2018) demonstrated that the ablation of OPA1 in SKM leads to mtDNA copy number depletion. This made us suspect that mt-stress associated genes as well as UPRmt would be also activated in this model. Comparative analysis of transcriptomic data of L-OPA1 KO and SKM-OPA1 showed that 13 of the 27 mt-stress associated genes up-regulated in either L-OPA1 KO or SKM-OPA1 KO were statistically significant in both studies Figure 30; in detail in Table 2).

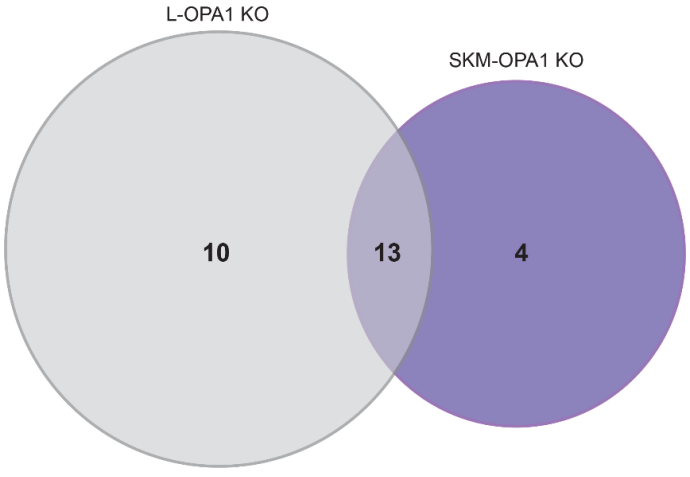

Figure 30. mt-stress associated genes are activated in both L-OPA1 and SKM-OPA1 KO mice models. Venn diagram showing commonly up-regulated genes in L-OPA1 KO and SKM-OPA1 KO with a FDR < 0.01.

Table 2. mt-stress associated genes intersection in SKM-OPA1 and L-OPA1 KO mice models

Gene	L-OPA1 KO FC > 1.5	SKM-OPA1 KO FC >1.5
Fam129a	3.34	2.63
Aldh1l2	1.54	2.99
Stc2	2.08	2.25
Pck2	2.32	3.46
Psat1	7.77	28.22
Trib3	6.60	26.07
Phgdh	5.85	2.77
Sars	1.84	2.08
Sesn2	1.76	6.26
Asns	1.92	52.83
Gars	1.68	2.65
Nupr1	3.34	6.45
Gdf15	2.68	5.02

Moreover, ATF5, LONP1 and FGF21 were also activated in OPA1 KO muscles, similarly to OPA1 KO livers (Table 3).

Table 3. UPRmt associated genes and FGF21 gene intersection in SKM-OPA1 and L-OPA1 KO mice models

Gene	L-OPA1 KO FC > 1.5	SKM-OPA1 KO FC >1.5
Atf5	3.79	3.54
Lonp1	1.99	3.64
Fgf21	1.98	1.94

Our results on mitochondrial function and metabolic phenotyping gathered with the analysis of transcriptomic data of our model and SKM-OPA1 KO mice model led us to hypothesize that OPA1 ablation causes mitochondrial stress, possibly by perturbing proteostasis in mitochondria, and leads to the activation of UPRmt via activation of ATF5 and induction of FGF21. FGF21 is possibly the factor responsible for the improvement in whole-body glucose homeostasis of L-OPA1 KO mice.

We next aimed to determine the molecular participant or participants responsible for the metabolic adaptation in response to mitochondrial dysfunction caused by OPA1-deficiency in liver. To this end, we next performed a series of *in vivo* and *in vitro* studies using L-OPA1 KO model and OPA1-deficient mouse embryonic fibroblasts cell model,

respectively. In the next sections, we will (1) explore the role of UPRer and UPRmt in FGF21 induction; (2) assess the involvement of phosphorylation of eIF2α in ATF5 activation and (3) characterize the implication of ATF5 in activation of UPRmt.

3.3.2 *In vivo* studies in L-OPA1 KO mouse model

We first assessed *fgf21* gene expression levels in liver and validated FGF21 circulating levels by using a specific ELISA kit. The results revealed that the expression of *fgf21* gene was 12-fold increase in liver in parallel with 16-fold greater circulating FGF21 levels in L-OPA1 KO mice (Figure 31.A-B).

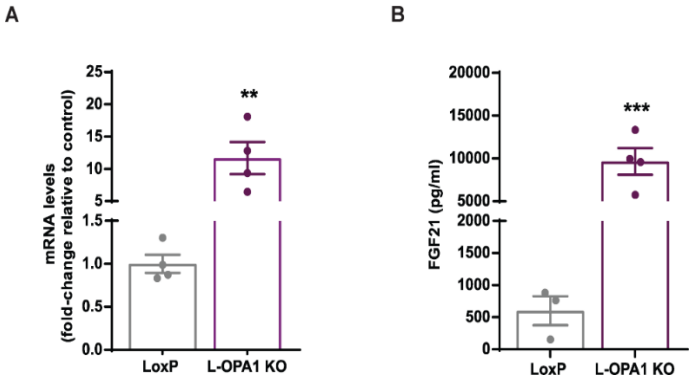

Figure 31. FGF21 is enhanced under OPA1 loss-of-function in liver. (A) *Fgf21* gene expression in liver of lox and L-OPA1 KO (n=4). (B) FGF21 levels in plasma of loxP and L-OPA1 KO mice (n=4). Data represent mean ± SEM. ** $p<0.01$ vs. control loxP mice.

Not only p-eIF2α-ATF4 arm of UPRer has been described to activate FGF21 but also mitochondrial stress in muscle have been stated to induce FGF21 secretion however the exact mechanism is still unknown. To further explore the involvement of the activation of UPRer and UPRmt pathways in the metabolic phenotype associated to OPA1 loss-of-function in liver we examined the induction of both pathways as it follows. We first analyzed the expression of key markers of the PERK, IRE1α and ATF6 UPR branches in liver homogenates. Our results demonstrate that UPRer arms ATF6 and IRE1α are activated in livers of L-OPA1 KO mice (Figure 32.A-B).

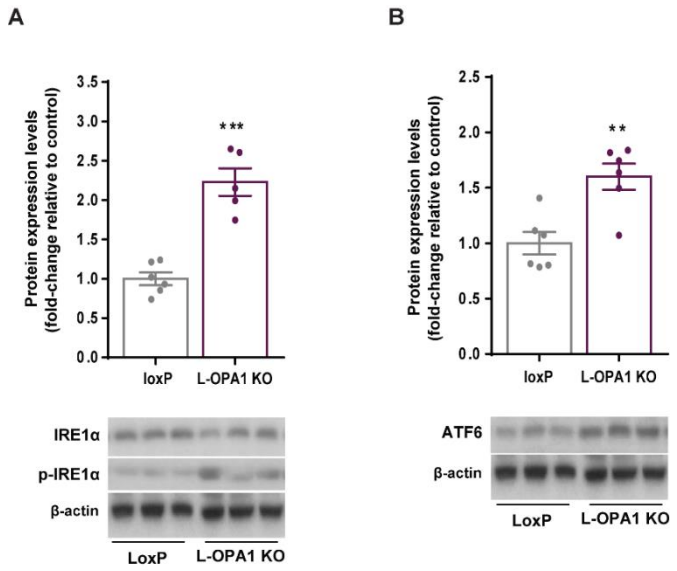

Figure 32. p-IRE1α and ATF6 are upregulated in OPA1-depleted livers. (A) Representative western blot and protein expression levels of p-IRE1α/IRE1α. (B) Representative western blot and protein expression levels of ATF6 in liver tissue homogenate of control loxP and L-OPA1 KO. Values corrected by β-actin. Data represent mean ± SEM. ** p<0.01 and *** p<0.001 vs. control loxP mice.

Protein expression analysis also confirmed the phosphorylation of eIF2a and activation of ATF4 and CHOP (Figure 33.A-B).

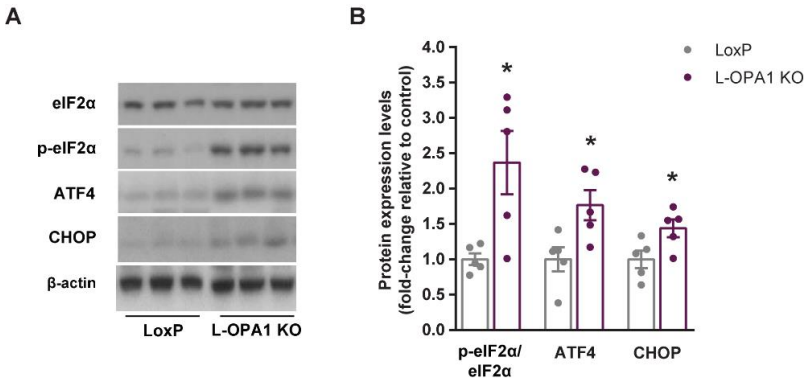

Figure 33. p-eIF2a-ATF4 pathway is activated in OPA1-depleted livers but not via PERK. (A) Representative western blot and protein expression levels of p-eIF2α/ eIF2α, ATF4 and CHOP in liver tissue homogenate of control loxP and L-OPA1 KO. Values corrected by β-actin. Data represent mean ± SEM. * p<0.05 vs. control loxP mice.

We next evaluated UPRmt-associated genes expression by quantitative PCR (qPCR) and at protein level. mRNA analysis showed increased expression of the UPRmt mediators *hspa9*, *lonp1* and *atf5* (encoding for mtHSP70, Lon protease and ATF5, respectively) in L-

OPA1 KO compared to control loxP. However, the expression of the mitochondrial chaperone genes, *hspd1* and *hspe1*, and ClPp protease gene, *clpp* (encoding for HSP60 and HSP10, respectively) did not change, as observed in transcriptomic studies (Figure 34).

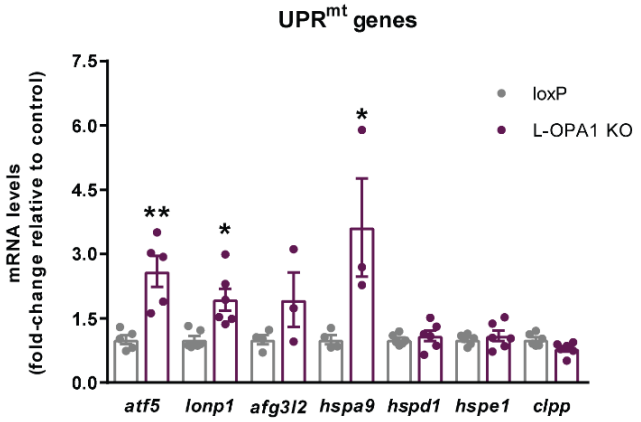

Figure 34. ATF5-mediated UPRmt genes are activated in L-OPA1 KO livers. (A) *atf5, lonp1, afg3l2, hspa9, hspd1, hspe1*and *clpp* genes expression in liver of lox and L-OPA1 KO (n=5). (B) *atf4* gene expression in liver of loxP and L-OPA1 KO livers (n=5). Data represent mean ± SEM. * p< 0.05, ** p<0.01 vs. control loxP mice.

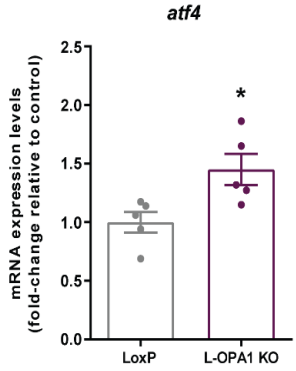

Moreover, *Atf4* gene was also found to be activated in OPA1 KO livers (Figure 35).

Figure 35. atf4 gene is activated in L-OPA1 KO livers. *atf4* mRNA expression levels in liver of lox and L-OPA1 KO (n=5). Data represent mean ± SEM. * p< 0.05 vs. control loxP mice.

In parallel, protein expression analysis supported the upregulation of the UPRmt transcriptional outputs, mtHSP70 and Lon (ATF5 targets), and AFG3L2 protease in L-OPA1 KO liver homogenates. (Figure 36.A-B).

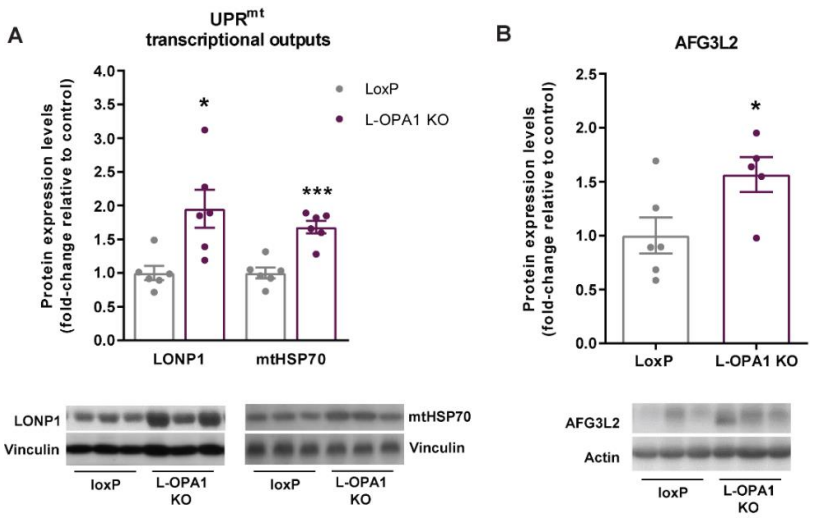

Figure 36. UPRmt transcriptional program is activated in L-OPA1 KO livers (A) Representative western blot and protein expression of ATF5 targets, mtHSP70 and LONP1. (B) Representative western blot and protein expression of AFG3L2, in liver tissue homogenates of 8-week-old loxP and L-OPA1 KO mice (n=5-6). Data represent mean ± SEM. * $p<0.05$; *** $p<0.001$ vs. control loxP mice.

3.3.3 *In vitro* studies in MEF OPA1-deficient cells

Given the activation of UPRer and UPRmt in liver upon OPA1-specific deletion, the next step was to determine the role of each of the pathways in the activation of FGF21. As mouse embryonic fibroblast (MEF) cells have been used in previous studies on FGF21 induction and activation of UPRer (Kim et al. 2015; Olivares and Henkel 2017), for mechanistic studies we used MEF OPA1-deficient cells (MEF Opa1$^{-/-}$) as our cellular model. To validate the feasibility of MEF Opa1$^{-/-}$ as cell model for this study, we examined FGF21 protein levels by western blot which revealed 3.5-fold higher levels of FGF21 in OPA1-deficient cells (Figure 37.A-B).

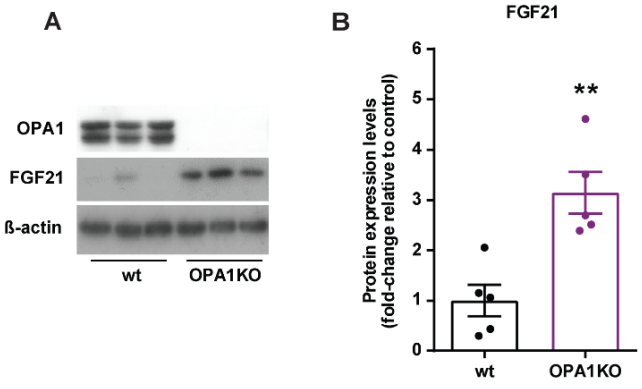

Figure 37.

Figure 37. FGF21 is induced in OPA1-/- MEF cells. (A) Representative western blot of OPA1 and FGF21 protein levels in total cell extract of control wild-type mouse embryonic fibroblasts (wt) and OPA1-KO mouse embryonic fibroblasts (OPA1KO). (B) FGF21 protein levels in total cell extract of wt and OPA1KO cells (n=3). Data represent mean ± SEM. ** $p<0.01$ vs. control cells.

We also evaluated mitochondrial morphology by means of the mitochondrial probe MitoTracker® Red CMXRos, which passively diffuse across the plasma membrane and accumulate in active mitochondria. Image analysis revealed that OPA1-deficient cells present alterations in the mitochondrial network characterized by the increase in mitochondrial fragmentation (Figure 38; left panel – loxP; right panel – OPA1 KO).

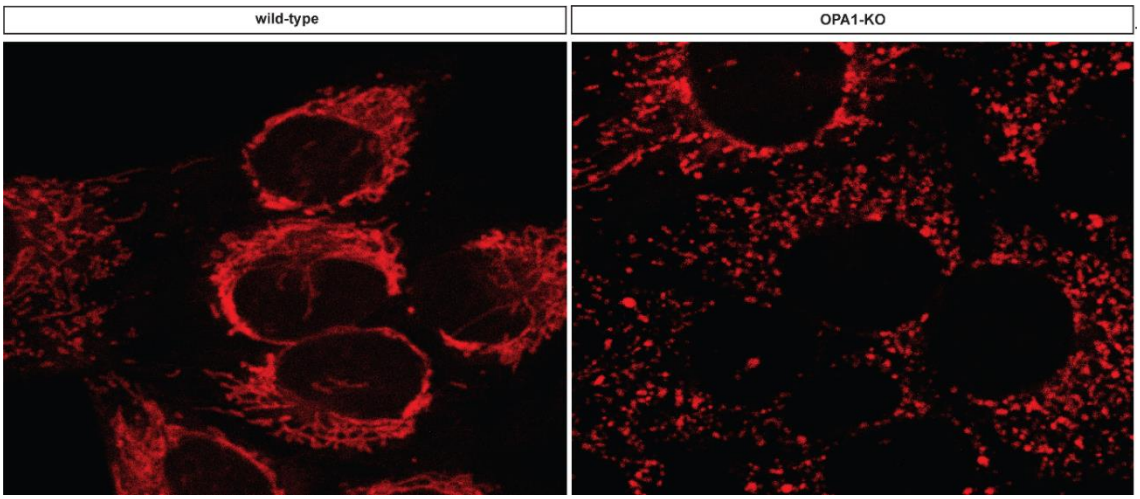

Figure 38. Mitochondria are fragmented in OPA1-deficient MEF cells. Representative images of mitochondrial network of MEF Opa1-/- cells incubated with MitoTracker® Red CMXRos. Mitochondria in red and nuceli in clear(n=3).

Given the alterations in mitochondrial network, we next analysed the cristae structure by TEM and our results showed that OPA1-deficient mitochondria present disorganized cristae (Figure 39; left panel – loxP; right panel – OPA1 KO).

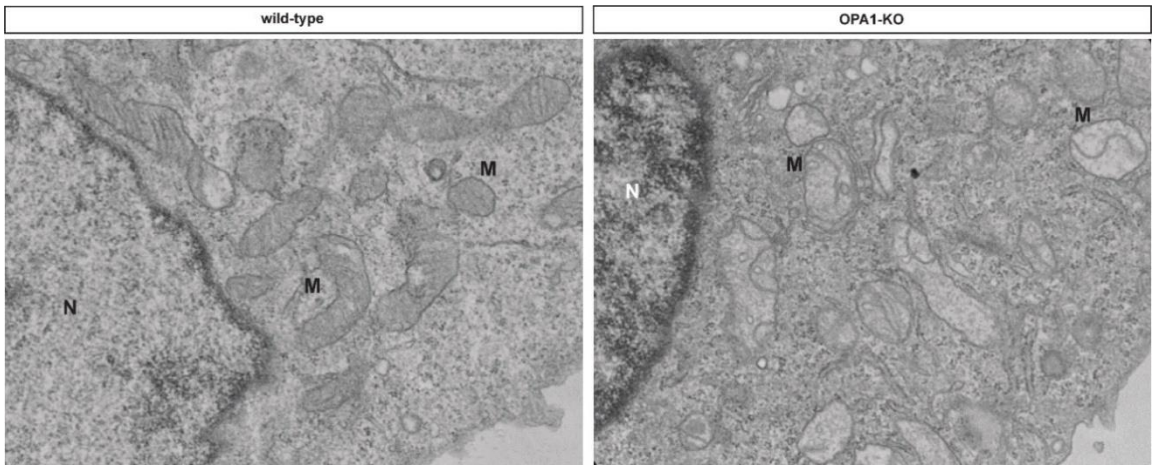

Figure 39. Mitochondria cristae are disorganized in OPA1-deficient MEF cells. Representative electron micrograhs of MEF Opa1-/- cells from control loxP and L-OPA1 KO mice. (n=3). (ER) Endoplasmic Reticulum. (M) Mitochondria. (N) Nuclei. Mitochondrial cristae indicated by arrows in the figure, in both panels.

One of the consequences of the disorganization of the cristae structure is the loss of ΔΨm. On that matter, we measured ΔΨm using the methyl ester tetramethylrhodamine, (TMRM) which is a cell-permeant dye that accumulates in active mitochondria with intact membrane potentials. Carbonyl cyanide-4-(trifluoromethoxy)phenylhydrazone (FCCP), a uncoupling agent, was used as positive control. Upon quantification of TMRM-positive cells, the results revealed loss of ΔΨm in OPA1-deficient cells (Figure 40).

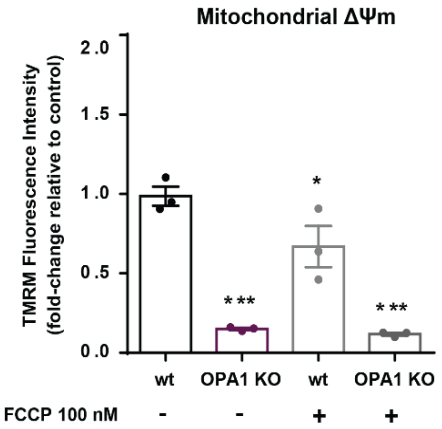

Figure 40. OPA1-deficient MEF cells present loss of mitochondrial membrane potential (ΔΨm). Quantification of TMRM positive cells of control wild-type mouse embryonic fibroblasts (wt) and OPA1-KO mouse embryonic fibroblasts (OPA1KO) in the presence and absence of FCCP 100nM used as positive control (n=3). Data represent mean ± SEM. * $p<0.05$, *** $p<0.001$ vs. control wt cells.

After extensive validation of MEF OPA1-deficient cells as cellular model for our studies, we next proceeded to evaluate the role of UPRer and UPRmt in FGF21 induction in these cells. We first analyzed the induction of ATF5 and its transcriptional targets, mtHSP70 and Lon. Protein expression analysis showed that ATF5 and mtHSP70 are

upregulated in MEF Opa1$^{-/-}$ cells, however, contrary to what we observed *in vivo*, Lon protease was reduced *in vitro* (Figure 41.A-D).

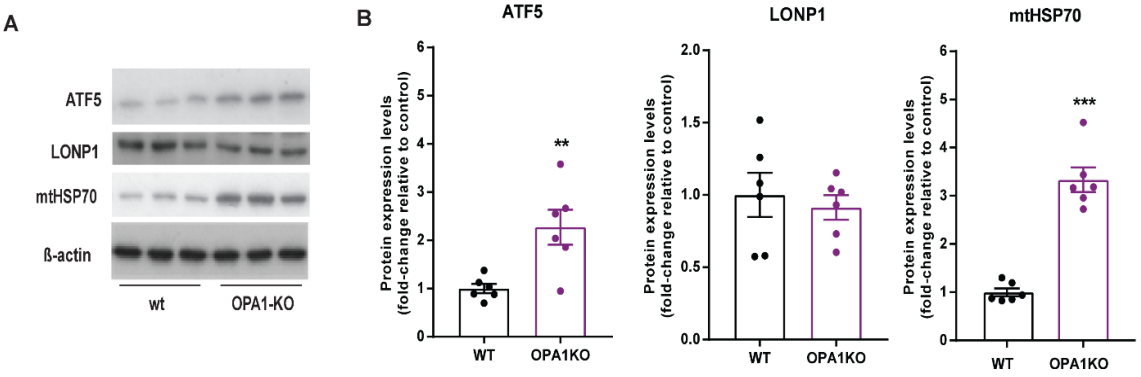

Figure 41. UPRmt transcriptional program is activated in OPA1-/- MEF cells. (A) Representative western blot of ATF5 and its targets LONP1 and mtHSP70 protein levels in total cell extract of control wild-type mouse embryonic fibroblasts (wt) and OPA1-KO mouse embryonic fibroblasts (OPA1KO). (B) Protein levels of ATF5, LONP1 and mtHSP70 of total cell extract of wt and OPA1KO cells (n=3). Data represent mean ± SEM. ** p<0.01, *** p>0.001 vs. control cells.

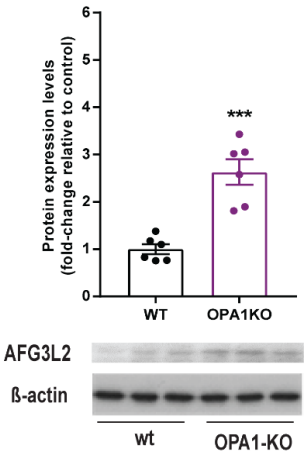

Protein analysis also revealed the up-regulation of AFG3L2 protease in MEF Opa1$^{-/-}$ cells compared wild-type (wt) cells (Figure 42).

Figure 42. Protease AFG3L2 is upregulated in OPA1-/- MEF cells. Protein levels of AFG3L2 of total cell extract of wt and OPA1KO cells and corresponding representative western blot (n=3). Data represent mean ± SEM. *** p<0.001 vs. control cells.

We next determined the activation of UPRer in cells by assessing protein levels of specific markers of the PERK, IRE1a and ATF6 branches. Protein analysis demonstrated that only p-eIF2a induction and ATF4 activation, also part of ISR, was up-regulated. OPA1-deficient cells (Figure 43.A-D).

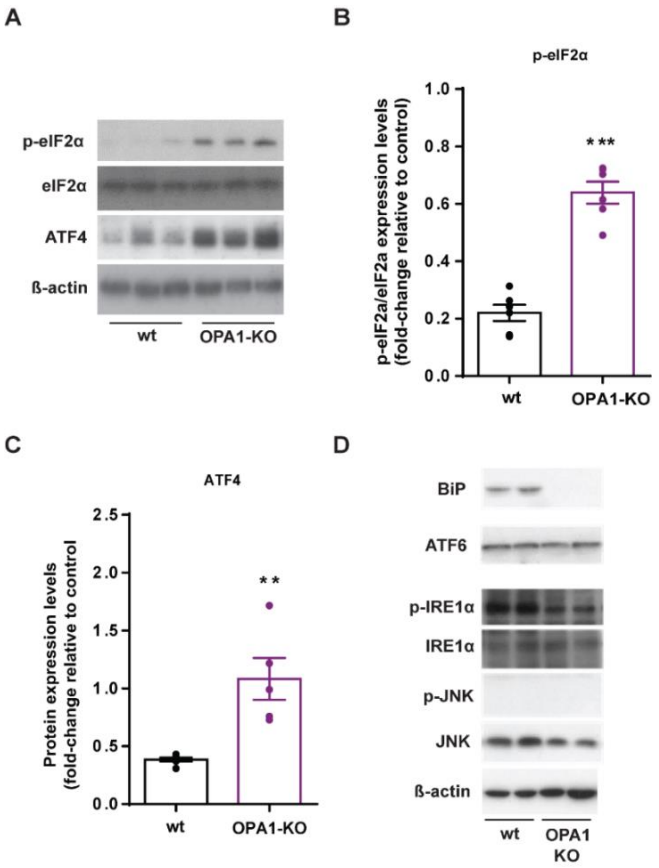

Figure 43. p-eIF2a and ATF4 are induced in OPA1-/- MEF cells in the absence of ER stress. (A) Representative western blot of p-eIF2a, eIF2a and ATF4 protein levels in total cell extract of control wild-type mouse embryonic fibroblasts (wt) and OPA1-KO mouse embryonic fibroblasts (OPA1KO). (B-C) Protein levels of p-eIF2α/eIF2α and ATF4 total cell extract of wt and OPA1KO cells (D) Protein levels of UPRer markers of ATF6 and IRE1α branches (n=3). Data represent mean ± SEM. ** p<0.01 vs. control cells.

These data suggested that the ER stress observed in liver is a tissue-specific response to stress caused by the deletion of hepatic OPA1 and that FGF21 induction relies on the activation of mitochondrial response. However, as we observed the activation of ATF4-p-eIF2α in OPA1-/- MEF cells, we speculated that the response to mitochondrial stress is possibly occurring downstream of phosphorylation of eIF2α. It has been described that different cellular stressors are capable of activating ATF4-p-eIF2α pathway, which culminates in the inhibition of total protein synthesis. Based on this, we proceeded to the treatment of the cells with ISRIB, an ISR inhibitor that specifically blocks eIF2α-phosphorylation in order to understand the its role in the response to the mitochondrial stress caused by OPA1.

The treatment with ISRIB for 24h reduced the expression of ATF4 but not ATF5 or FGF21 (Figure 44), suggesting that the activation of ATF5 and FGF21 is not dependent of eIF2α-phosphorylation and consequential downstream ATF4 activation.

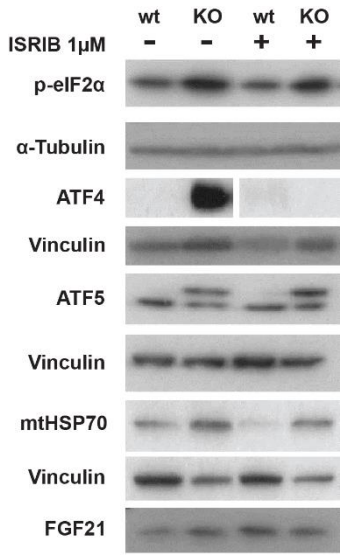

Figure 44. Inhibition of p-eIF2α in blocks ATF4 but not ATF5 OPA1-/- MEF cells. Representative western blot of p-eIF2a, ATF4, ATF5, mtHSP70 and FGF21 protein levels in total cell extract of control wild-type mouse embryonic fibroblasts (wt) and OPA1-KO mouse embryonic fibroblasts treated with 1 μM ISRIB upon 24h treatment (OPA1KO; n=3).

ATF5 has been described to localize to mitochondria in the absence of stress due its MTS but during mitochondrial stress it specifically responds to perturbations in mitochondrial protein import by translocating from mitochondria and accumulating in the nucleus. Fiorese et al. (2016) have proposed that ATF5 acts as key effector of UPRmt independent of ATF4 activity, however in their model they described ATF5 activation dependent on the eIF2α-phosphorylation (Fiorese et al. 2016).

Given the previous result and our results demonstrating that the deletion of OPA1 in liver led to reduction of OxPhos complexes subunits, mtDNA instability and reduced levels of TFAM which could possibly lead to peptide accumulation in mitochondria and block protein import, we suspected that ATF5 would play a role in the activation of UPRmt transcriptional program upon OPA1-deletion. By confocal microscopy, we examined the translocation of ATF5 from mitochondria to the nucleus in OPA1-KO MEF cells. Image

analysis showed that ATF5 accumulated in the nuclei, rarely co-localized with mitochondria, and surprisingly formed agglomerates in the cytosol of MEF Opa1$^{-/-}$ cells (Figure 45).

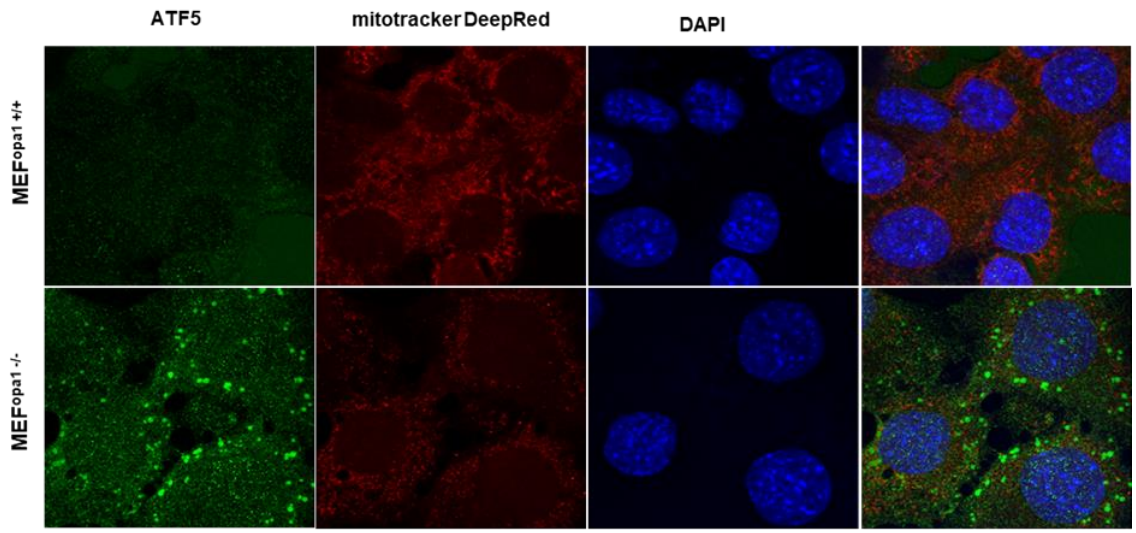

Figure 45. ATF5 accumulates in the cytosol and co-localizes in the nuclei in OPA1-deficient cells. Immunofluorescence of ATF5 and mitochondria mitotracker DeepRed labelling in MEF wt (upper panel) vs MEF Opa1$^{-/-}$ cells (lower panel). ATF5 localizes to nuclei in MEF Opa1$^{-/-}$ cells as demonstrated by co-localization with nuclear marker DAPI.

To get further insight into the role of ATF5 in the induction of FGF21 upon OPA1 deletion, we developed an Atf5$^{-/-}$ MEF cells model using CRISPR-Cas9 technology. Using this technology we obtained a 62% deletion of Atf5 mRNA. By knocking down Atf5 gene, we observed a substantial reduction in Opa1 and Fgf21 genes, while Atf4 gene remained unaltered (Figure 46), suggesting that, in one hand, ATF5 interacts with OPA1 and on the other hand, FGF21 induction is rather dependent on ATF5 activation.

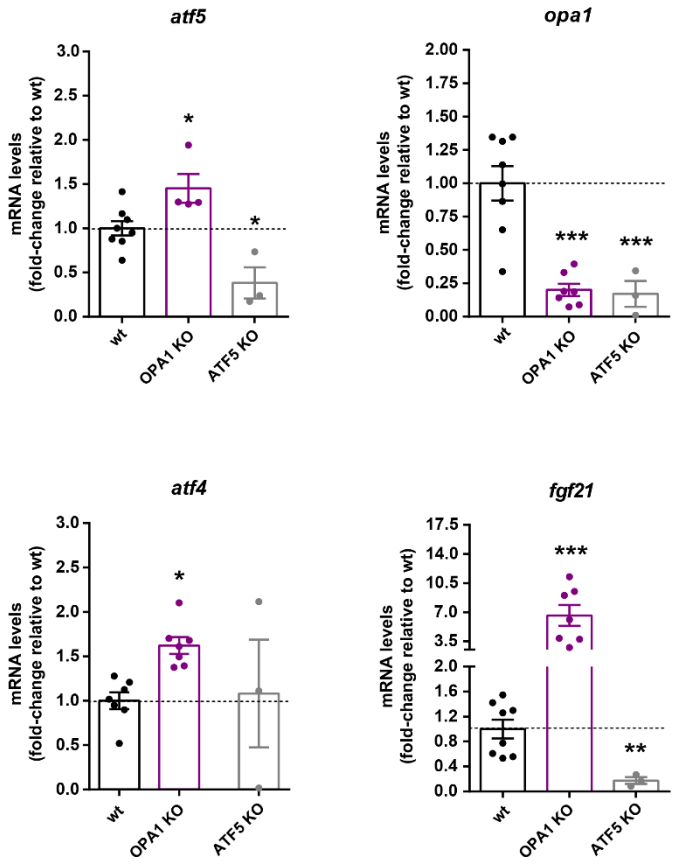

Figure 46. Deletion of ATF5 in wt MEF cells provokes a reduction in OPA1 and FGF21 but not in ATF4 mRNA levels. *atf5* (left-upper panel), *opa1* (right-upper panel), *atf4* (left-lower panel) and *fgf21* (right-lower panel) gene expression levels of wt, OPA1 and ATF5 KO cells. Data represent mean ± SEM. * $p<0.05$, ** $p<0.01$, *** $p<0.001$ vs control cells.

4

Discussion

4 Discussion

The results of the present work, based on basic characterization of mitochondria function and morphology, metabolic phenotyping of L-OPA1 KO mice model and mechanistic studies, can be synthesized below:

1. OPA1 ablation causes impaired mitochondrial respiration, mtDNA deletion, perturbances in cristae organization and mitochondrial proteostasis.

2. Liver-specific OPA1 loss-of-function results in improved whole-body glucose homeostasis and protects against diet-induced obesity and insulin resistance.

3. OPA1 deficiency in liver context causes chronic mitochondrial stress that leads to activation ATF5-mediated UPRmt.

In this chapter dedicated to discussion, I am going to dissect and explore the possible interpretations of the results obtained throughout this PhD thesis. At the end of the chapter, I will comprehensively discuss my working model.

4.1 Evaluation of the impact of OPA1 loss-of-function in mitochondrial function in liver

OPA1 is an essential dynamin-related GTPase that participates in the process of inner mitochondrial membrane fusion and modulates mitochondrial cristae structure organization, impacting directly mitochondria oxidative capacity and mtDNA stability. Studies have demonstrated that OPA1 is required for proper mitochondrial metabolism during mouse embryonic development as genetic ablation of Opa1 is lethal (Rahn et al. 2013). OPA1 multifunctional feature and the impact of its loss-of-function has been extensively explored in different cell models including transient OPA1 silencing and/or stable genetic ablation and, to some extent, *in vivo* studies have been conducted as well, although not much has been described in the context of liver tissue. In this study we have explored the impact of the loss of hepatic OPA1 functionality in mitochondrial function and metabolism. Liver-specific OPA1 knockout mouse model (L-OPA1 KO) was obtained in the laboratory. Upon the successful generation of L-OPA1 KO model we have characterized mitochondrial defects associated with OPA1 loss-of-function in liver in mice subjected to a normal chow diet.

Immunoelectron microscopy studies showed that OPA1 is mostly associated with the cristae membrane and inner boundary membrane with gradual decreases toward cristae junction and cristae tip (Barrera et al, 2016). Studies have documented that the absence of OPA1 or the presence of OPA1 pathogenic mutations are associated with dramatic disruption of the cristae structure, showing greatly decreased cristae number and loss of cristae tightness, which is defined by the narrowness of the width between two cristae membranes (Olichon et al., 2003; Griparic et al., 2004; Lee et al., 2017). In keeping with previous research, our data support that the presence of OPA1 is crucial for maintaining the proper mitochondria cristae ultrastructure. Not only OPA1 is crucial for the bioenergetic competence of mitochondria as a result of its role in the cristae ultrastructure remodeling of but also due to interacting directly with the subunits of the respiratory complexes, suggesting a stabilizing function over the respiratory chain (Zanna et al., 2008). Keeping with this, here we document a substantial reduction in mitochondrial respiratory capacity and in both nDNA- and mtDNA-encoded OxPhos complexes subunits in liver from L-OPA1 KO mice. Here we expose some explanations for it.

First, hepatic OPA1 loss-of-function was characterized by a reduction in mtDNA copy number which would explain the decreased expression of the mtDNA-encoded subunit

MTCO1. Several in vitro studies have described that the ablation of OPA1 or the presence of OPA1 mutations cause a marked depletion of mtDNA or can affect mtDNA nucleoid distribution within mitochondrial matrix, leading to mtDNA instability (Chen, 2010). Additionally, Rodriguez-Nuevo (2018) have recently demonstrated in our laboratory that the depletion of OPA1 in skeletal-muscle caused mtDNA instability by reducing mtDNA copy number and nucleoids abundance. These studies together with our data support the role of OPA1 on mtDNA stability and suggest that is not restricted to cells or tissue-specific. Moreover, in L-OPA1 KO livers TFAM protein abundance was reduced. It has been described that TFAM deficiency results in mtDNA instability (West et al., 2015) which could explain the reduction in mtDNA copy number observed in livers from L-OPA1 KO mice. Also, in this study we have reported that Lon protease was activated as part of the UPRmt in OPA1-knockout livers. Mitochondrial LON protease is responsible for the degradation of TFAM (Matsushima, Goto and Kaguni, 2010), where such degradation is highly affected by the amount of mtDNA bound to TFAM, as unbound TFAM rapidly degraded by LON protease (Lu et al., 2013). Thus, it is possible that mtDNA-TFAM interaction directly affects TFAM abundance upon OPA1 deletion in liver.

Secondly, the formation of a functional respiratory chain depends on the coordinated assembly of nuclear-encoded subunits, which must be imported into mitochondria after their synthesis on cytosolic ribosomes, with mt-encoded respiratory chain subunits (Baker et al., 2011). In liver lacking OPA1, it is easy to speculate that the assembly of the nuclear- and mtDNA-encoded is perturbed and that there is accumulation of non-assembled subunits. Several mitochondrial proteases degrade non-assembled subunits to prevent and thus prevent potential proteotoxic damaging effects (Arlt et al. 1998; Hornig-Do et al. 2012; Stiburek et al. 2012; Richter et al. 2015), which could be what it is happening in the OPA1-deficient livers, revealing therefore a reduction in nuclear-encoded OxPhos complexes subunits.

As a consequence of OPA1 deletion in liver, some mitochondrial protein markers, as in TIMM44 and VDAC/porin, were upregulated suggesting an increase in mitochondrial mass. Our first assumption was that, as a result of the activation of UPRmt, mitochondrial biogenesis would be occurring. However, hepatic PGC1a gene was unchanged in livers of L-OPA1 KO mice. In our group it was revealed that OPA1 deletion in muscle cells impaired the completion of mitophagy (Rodriguez-Nueveo, 2018). Transmission electron microscopy results in this study showed more fragmented mitochondria in OPA1-deficient hepatocytes

which would prone mitochondria to undergo mitophagy, however mitochondrial mass seems to be increased. This, together with the results gotten from OPA1-deficient muscle cells led us to hypothesize that perhaps OPA1 deletion in liver is also causing impaired completion of mitophagy. Further studies would be necessary to address this question though.

4.2 Study of the metabolic impact caused by hepatic ablation of OPA1

Mitochondrial dysfunction has been long linked to obesity and associated insulin resistance. By contrast, in the past decade studies have been challenging this correlation. In this study we sought to analyze the metabolic impact of mitochondrial dysfunction caused by the loss of hepatic OPA1 functionality. L-OPA1 KO mice were more tolerant to glucose and more responsive to reduced insulin circulating levels regardless of the presence of mitochondrial dysfunction in liver.

These data demonstrate that L-OPA1 KO mice are more glucose-handling effective in the presence of lower insulin secretion. Moreover, during the insulin tolerance test, L-OPA1 KO mice revealed a higher response to insulin which indicates a higher insulin sensitivity. Thus, we can report that at least mitochondrial dysfunction associated to defects in OxPhos and mtDNA copy number reduction in liver impacts whole-body metabolism. Nonetheless, to further strengthen our hypothesis, for future studies it would be interesting to perform hyperinsulinemic-euglycemic clamps. Hyperinsulinemic-euglycemic clamps are a gold standard approach not only to assess insulin action but also to determine sites where insulin action is affected and consequently tissue-specific glucose uptake (Ayala et al., 2006; Wasserman et al., 2009).

Differences in body weight, body mass distribution, food intake and energy expenditure were not observed in L-OPA1 KO mice in chow diet, suggesting that the improvement in glucose homeostasis observed in our model is not associated with these factors. These observations suggest that these tissues are not involved in the improved glucose homeostasis in L-OPA1 KO and possibly the metabolic shift is in fact occurring in the liver, at least on a chow diet. To explore this possibility, future studies could analyze hepatic glucose oxidation and hepatic insulin signaling.

When challenged with a high-fat diet, L-OPA1 KO mice were significantly leaner compared to control loxP mice, despite no differences in food intake demonstrating that L-

OPA1 KO mice are resistant to diet-induced obesity. Additionally, L-OPA1 KO mice are protected against diet-induced insulin resistance due to their improved glucose handling capacity that they are capable of maintaining despite the lipid overload.

Regarding energy expenditure, L-OPA1 KO mice revealed a higher energy expenditure in HFD in both dark and light periods, which corroborates with the higher levels of oxygen consumption and carbon dioxide production. These animals presented higher levels of glucose and lipid oxidation; however RER values are no different between groups. The circadian usage of fuel sources was ablated (glucose-fed-night vs lipid-fast-day) as glucose oxidation is not restricted to the day period neither lipid oxidation is restricted to the night period. These animals also were more physically active than loxP control mice.

As these studies are not restricted to liver metabolism and are rather an indication of the state of systemic whole-body metabolism, to explain such changes it would be of interest to assess in future studies the mitochondrial respiratory capacity not only in the liver but also in brown adipose tissue and skeletal muscle fibers in order to understand which of these tissues might display oxidative capacity that is enhanced and possibly responsible for the improved metabolic phenotype.

These animals clearly displayed lower levels of plasma cholesterol in both fed and fasting states, which was also observed on HFD. The liver has a central role in cholesterol homeostasis as it is the only tissue capable of cholesterol de novo synthesis and therefore displays of a system of cholesterol secretion to the system through bile acid production. Based on this, we think that an impairment in either the bile acid production or cholesterol biosynthesis system must be present in the livers of L-OPA1 KO. However, this is only a hypothesis at this point. Future studies in the hepatic cholesterol de novo synthesis and secretion by bile acid production would help us understand how the deletion of OPA1 in liver is affecting cholesterol homeostasis.

NEFAs circulating levels were increased in L-OPA1 KO mice in both chow diet and HFD feeding suggesting that possibly white adipose tissue in L-OPA1 KO is more lipolytic active compared to the control loxP mice. This feature of white adipose tissue in L-OPA1 might contribute to leaner phenotype in L-OPA1 KO mice on HFD regimen.

4.3 Identification of the key players responsible for the metabolic phenotype associated to OPA1 deficiency in liver

Based on the data linking hepatic OPA1 deficiency and amelioration in whole-body metabolism, we next aimed to determine the molecular participant or participants responsible for the observed phenotype and to explain the mechanisms by which mitochondrial dysfunction caused by OPA1-deficiency in liver is capable of generating a systemic metabolic response. Consistent with the results gathered from the metabolic characterization of the liver-specific OPA1 KO (L-OPA1 KO), hepatic *fgf21* gene and plasma levels of the mitokine were increased in our mice model as well as the protein levels in OPA1-deficient cells. These cells were characterized by aberrant cristae organization, fragmented mitochondria and loss of mitochondria membrane potential. Moreover, FGF21 induction in OPA1-deficient SKM has previously been documented in our laboratory (Rodríguez-Nuevo et al. 2018).

FGF21 has been described to play a relevant role in glucose homeostasis and lipid metabolism leading to a better whole-body metabolism (reference). The primary physiological role of FGF21 induction is to respond and adapt to starvation and is mainly produced in liver (Inagaki et al., 2007). Besides, it has also described to be secreted by the cells during cellular stress. Moreover, OPA1 deletion in SKM has been demonstrated by Pereira et al. (2017) to eradicate diet-induced obesity susceptibility via FGF21 upregulation. Given the observations in OPA1-SKM KO together with the remarkable high hepatic and circulating levels of the mitokine in our model, we believed that FGF21 has a relevant role in the metabolic phenotype observed in L-OPA1 KO mice. We hypothesized that OPA1 loss-of-function associated mitochondrial dysfunction led to increased expression of FGF21 and contributed for the improvement in glucose homeostasis and concomitant protection against diet-induced obesity in L-OPA1 KO mice. Aiming to determine the contribution of FGF21 to the metabolic adaptation in L-OPA1 KO and the potential mediators of its induction upon OPA1 deletion, we performed transcriptomic analysis and other relevant *in vivo* and *in vitro* experiments on livers of L-OPA1 KO and OPA1-deficient MEF cells, respectively.

Special attention has been given to the association between eIF2a-phosphorylation-ATF4 axis, part of both UPRer and ISR, and the induction of FGF21 in conditions of mitochondrial dysfunction (Kim et al., 2015, Schaap et al., 2013; Pereira et al., 2017; Tezze

et al., 2017; Rodríguez-Nuevo et al., 2018). Indeed, studies have extensively associated the eIF2a-phosphorylation and downstream ATF4 activation, part of the endoplasmic reticulum unfolded protein response (UPRer) and ISR, to the induction of FGF21 (Kim et al., 2015, Schaap et al., 2013). Phosphorylation of eIF2α inhibits the loading of methioninyl-tRNAs thus preventing normal translation initiation by reducing the availability of this kind of tRNA. This favors the expression of ATF4 due to its double regulatory translation initiation regions which enables the translation of the ATF4 protein only in situation of low tRNAMet availability (Wek, Jiang and Anthony, 2006).

In this study, the activation of the 3 branches of the UPRer in the livers of L-OPA1 KO mice were detected. Recent studies have proposed the link between OPA1 deletion and consequent FGF21 induction via ER stress activation in the skeletal-muscle. For instance, Tezze et al. (2017) showed that OPA1 ablation in skeletal muscle resulted in FGF21 induction through the activation of ATF4 and alternative splicing of Xpb1, which was rescued by chemical chaperon administration. Similarly, Pereira et al. (2017) demonstrated that the induction of FGF21 in skeletal-muscle upon deletion of OPA1 was accompanied by increased eIF2a-phosphorylation and Atf4, Chop and BiP mRNA expression, as well as alternative splicing of Xpb1, recovered by chemical chaperon administration. These data support the role of ER stress in FGF21 induction in both models. Differently in our laboratory Rodriguez-Nuevo et al. (2018) reported that eIF2a-phosphorylation upon OPA1 ablation in skeletal muscle was independent on ER stress as no PERK induction was observed. Interestingly, in our study, even though livers from L-OPA1 KO mice revealed activation of ER stress, in OPA1-deficient cells the activation of UPRer was not observed, leading us to assumption that the activation of this pathway is a tissue-specific response to the lack of OPA1 and probably not the factor responsible for the phenotype observed in vivo, as stated up to date in the literature. Nonetheless, the activation of a specific mitochondrial unfolded protein response to stress was observed in both of our *in vivo* and *in vitro* models in our study.

Having discard ER stress as a major player in FGF21 induction associated to hepatic OPA1 deletion, we focused on UPRmt as the main mediator of the metabolic adaptation observed in L-OPA1 KO mice. The UPRmt transcriptional program was defined by the upregulation of ATF5 gene and its targets, the mitochondrial chaperone mtHSP70 and mitochondrial protease LONP1, and AFG3L2 at mRNA and protein levels in livers of L-OPA1 KO mice but no changes were observed in ClPp protease or the chaperonins HSP60

and HSP10 gene expression. Curiously, in OPA1-deficient cells mtHSP70 and AFG3L2 were upregulated but ClPp gene expression levels were downregulated and LONP1 expression was not altered. Bhaskaran et al. (2018) demonstrated that activation of ClpP is dispensable for the activation of UPRmt *in vivo*. The fact that LONP1 is not altered in OPA1-deficient cells led us to speculate that the proteotoxic effects associated to the ablation of OPA1 in cells could be slightly different in vitro. Unfolded proteins no longer capable of being folded by chaperones in mitochondria are turned over by mitochondrial proteases. For instance, LON protease functions in collaboration with chaperones in order to keep client proteins in an unfolded state until further proteolytic removal (Baker et al., 2011). Perhaps, in vitro, the accumulation of misfolded proteins is not as severe in vivo and therefore, the activation of mtHSP70 is sufficient to counteract the proteotoxic effects without the need to turn over by LON protease.

Another important observation worth noting in L-OPA1 KO livers is the presence of a mitochondrial stress-associated genes signature characterized by the synthesis of relevant amino acids of which normally occurs during mitochondrial stress as means to boost the synthesis of important protein effectors enzymes to counteract the proteotoxicity caused by the accumulation of misfolded proteins (Quirós et al., 2017).

As mentioned before in this discussion chapter, it is possible that loss of the OxPhos complexes stoichiometry is occurring caused by OPA1 deficiency. This can lead to the accumulation of misfolded proteins within the mitochondrial matrix and one strategy to escape proteotoxicity is to decrease mitochondrial protein import system as a means to avoid the entrance of proteins into the mitochondria while neutralizing the proteotoxic side effects (Ahola et al., 2019). It is relevant to mention that ATF5 has been described to specifically respond to perturbations in mitochondrial protein import by translocating from mitochondria and accumulating in the nucleus (Fiorese et al., 2017). Therefore, it is not surprising that upon deletion of OPA1, ATF5 and its targets are upregulated in livers of L-OPA1 KO mice and in OPA1-deficient MEF cells and made us reason that ATF5 could be the main key player of UPRmt activation. Additionally, we observed by confocal microscopy that ATF5 accumulated in the nuclei, rarely co-localized with mitochondria, and surprisingly formed agglomerates in the cytosol of MEF Opa1$^{-/-}$ cells, suggesting that ATF5 might not only mediate a mitochondrial retrograde response but also probably a cytosolic response to mistargeting of mitochondrial proteins, possibly similar to the unfolded protein response

activated by the accumulation of mistargeting of mitochondrial proteins in the cytosol (UPRam) observed in yeast but lacks of studies in mammals (Callegari and Dennerlein 2018).

Moreover, transcriptomics comparison between L-OPA1 KO and SKM-OPA1 KO mice models demonstrated that upon OPA1 deletion in SKM 10 out of 25 mt-stress associated genes in L-OPA1 KO were also activated, concomitantly with activation of ATF5, LONP1 and FGF21. This analysis supports our hypothesis that ATF5 could be a key player in the mitochondrial response caused by the ablation of OPA1, independently of the tissue context and possibly the main mediator in FGF21 induction. In Fiorese's model (2016), ATF5 is proposed to be activated downstream of eIF2α-phosphorylation but independent of ATF4 activity, however other studies have demonstrated the dependence of ATF5 activation on ATF4 activation.

With the aim of assessing the role of ATF5 as the key regulator of UPRmt activation, its modulation and FGF21 induction upon OPA1 deletion we, on the one hand (1) generated ATF5-silenced cells in wt MEF cells and on the other (2) we blocked the activity of phosphorylation of eIF2a in vitro using an inhibitor of the activity of p-eIF2a, ISRIB. ISRIB acts as a 'molecular staple' that specifically binds to p-eIF2a and rescues general translation (Rabouw et al., 2019). The former experiment was relevant to demonstrate that FGF21 induction in MEF cells is not dependent on ATF4 activation but rather on ATF5 action and later showed that ATF5 activation is independent of the eIF2a phosphorylation, differently from what has been described in the literature. Both experiments allow us to state that hypothesize that, in OPA1-deficient cells, the response to mitochondrial damage caused by the ablation of OPA1 is mediated by ATF5 which induces the expression of FGF21, both independent of eIF2a-phosphorylation.

While it is tempting to speculate that the induction of FGF21 in OPA1-deficient livers is exclusively mediated by ATF5 and that ATF5 activation is p-eIF2a-independent, futures studies should be performed. For instance, on the one hand, silencing ATF5 in vivo and assess FGF21 would help us understand whether ATF5 is the mediator of FGF21 in vivo and on the other hand, in vivo treatment with ISRIB would enlighten us whether ATF5 activation in liver is independent of p-eIF2a.

To sum up, our results showed that OPA1 ablation in liver leads to chronic mitochondrial stress and triggers the activation of UPRmt possibly mediated by ATF5. Moreover, our results suggest that the induction FGF21 relies on the activation of a

mitochondrial response to stress caused by the depletion of OPA1 which, consequently, becomes systemic and improves whole-body glucose homeostasis.

In this study I provide evidence for a link between OPA1 deficiency and the triggering of local mitonuclear retrograde signaling in the hepatic cell as an attempt to counteract the mitochondrial damage caused by the OPA1 loss-of-function, which in turn becomes systemic through FGF21 induction and is responsible for the metabolic adaptation experienced by L-OPA1 KO mice. From a translational perspective, it will be key to fully characterize this model and study the long-term effects of mitochondrial stress response.

5

Conclusions

5 Conclusions

Based on the results of this doctoral thesis, we propose the following conclusions:

1. The ablation of OPA1 results in mitochondrial dysfunction characterized by defects in mitochondrial respiratory capacity, mtDNA copy number reduction, perturbations in the mitochondrial cristae organization and mitochondrial proteostasis; This generates chronic mitochondrial stress that leads to the activation of a response to mitochondrial stress and UPRmt.

2. The response to the mitochondrial stress caused by liver-specific OPA1 loss-of-function leads to FGF21 induction.

3. OPA1 deficiency in liver causes improved glucose tolerance and protects against diet-induced obesity and insulin resistance possibly due to the action of FGF21.

4. The absence of OPA1 leads to the activation of UPRmt mediated by the accumulation of ATF5 in the nucleus and in the cytosol, which modulates FGF21 induction in FGF21 in OPA1-deficient cells.

5. We propose a model in which OPA1 deficiency causes chronic mitochondrial stress that triggers a specific mitochondrial response that eventually becomes systemic and improves glucose homeostasis. In addition, we suggest ATF5 as the main mediator of this response.

6

Material & Methods

6 Material and Methods

6.1 Material

The materials used in the development of this work are included in the following tables, classified in four different categories: reagents, diets, kits, cell culture reagents, antibodies and primers.

Table 2. Details of reagents used

A. Buffers preparation

Name	Storage	Source & Cat. No.
Benzonase ® Nuclease	-20 ºC	Sigma-Aldrich E1014
Chloroform	RT	Merck-Millipore #822265
cOmplete, Mini Protease Inhibitor Cocktail	4 ºC	Sigma-Aldrich #11836153001
Deoxycholate	RT	Sigma-Aldrich D6750
Ethanol	RT	Panreac AppliChem #131086.1211
KOH pellets	RT	Sigma-Aldrich #757551
Methanol	RT	Panreac AppliChem #131091.1611
NaCl	RT	Sigma- Aldrich #71376
Phosphatase Inhibitor Cocktail Set IV	-20 ºC	Merck-Millipore #524628
Proteinase K	4 ºC	Sigma-Aldrich P2308
SDS	RT	Sigma-Aldrich #11667289001
Tert-Butanol	RT	Sigma-Aldrich #471712
Tris-HCL	RT	Sigma-Aldrich #10812846001
Triton X-100	RT	Merck-Millipore #108603

B. Isolation buffer composition (final volume of 250 mL)*

Compound	Final concentration	Source & Cat. No.
EDTA	5 mM	Merck-Millipore #324503
KCL	50 mM	Sigma-Aldrich P9333
$MgCl_2$	5 mM	Sigma-Aldrich M8266
$Na_4P_2O_7$	1 mM	Sigma-Aldrich P8010
Sucrose	250 mM	Sigma-Aldrich S8501

*Adjust the pH to 7.4. Add protease inhibitors to working volume.

C. MiR05*

Compound	Final concentration	Source & Cat. No.
BSA, essentially fatty acid free	1 g/L	Sigma-Aldrich A6003
D-sucrose	110 mM	Sigma-Aldrich #84097
EGTA	0.5 mM	Sigma-Aldrich E4378
HEPES	20 mM	Sigma-Aldrich H7523
KH_2PO_4	10 mM	Merck-Millipore #104873
K-lactobionate solution**	60 mM	Sigma-Aldrich153516
$MgCl_2 \bullet 6\ H_2O$	3 mM	Scharlau MA0036
Taurine	20 mM	Sigma-Aldrich T0625

*1. Prepare stock solutions of K-lactobionate; 2. Weigh all the other components and dissolve in 800mL H_2O a 30ºC; 3. Add 120mL of K-lactobionate stock solution; 4. Dissolve BSA in a subsample of the solution (stir it gently to avoid to prevent foam building) and transfer back to the final solution; 5. Adjust with H_2O to the final volume; 6. Adjust pH to 7.1 (with 5 M KOH).

**Preparation K-lactobionate stock solution: dissolve K-lactobionate in 100mL H_2O; adjust pH to 7.0 with KOH; adjust volume to 200 mL with H_2O.

D. Assays

Name	Storage	Source & Cat. No.
ADP	-20 ºC	Sigma-Aldrich A5285
Antimycin A	-20 ºC	Sigma-Aldrich A8674
CCCP	-20 ºC	Sigma-Aldrich C2759
Cytochrome c	-20 ºC	Fluka #30398
D-(+)-Glucose	RT	Sigma-Aldrich G7021
DNA Pol	-20 ºC	Biotools #10043
dNTPs	-20 ºC	Roche # 11969064001
ECL	4 ºC	Amersham Biosciences RPN3244
Ethanol	RT	Panreac AppliChem #131086.1212
FCCP	4 ºC	Sigma-Aldrich C2920
Glutamate	4 ºC	Santa Cruz Biotechnology sc-211703
Glycine	RT	Sigma-Aldrich G7126
Hoechst 33342	4 ºC	Life technologies H3570
Humalog® 100U / mL insulin	4 ºC	Eli Lilly, Co. VL7510
Isopentane	RT	Sigma-Aldrich M32631
Isopropanol	RT	Panreac AppliChem #131090.1211
L-(-)-Malic acid	RT	Sigma-Aldrich M1000
Mitotracker™ Deep Red FM	-20 ºC	Invitrogen M22426
Mitotracker™ Red CMXRos	-20 ºC	Invitrogen M7513
NH_4Cl	RT	Sigma-Aldrich #31107
OCT	RT	TissueTek #4583
PFA 4%	RT	Santa Cruz Biotechnology sc-281692
Rotenone	RT	Sigma-Aldrich R8875
Saponin	RT	Sigma-Aldrich #47036
Sodium succinate dibasic hexahydrate	RT	Sigma-Aldrich S2378
TMRM	-20 ºC	Invitrogen T668
TRIzol	4 ºC	Invitrogen #15596026
Saponin	RT	Sigma-Aldrich #47036

Table 3. Details of diets used

Name	Storage	Source & Cat. No.
Rodent Diet with 60% kcal% fat	4 ºC	Research Diets D12492

Table 4. Details of kits used

Name	Applications	Storage	Source & Cat. No.
BM Cyclin kit	Mycoplasma decontamination	-20 ºC	Roche #10799050001
DNeasy Blood & Tissue	DNA purification	RT	Qiagen #69504
EZ-PCR Mycoplasma test kit	Mycoplasma test	-20 ºC	Biological Industries, Co #20-700-20
Pierce™ BCA Protein Assay Kit	Protein quantification	RT	ThermoFisher #23227
Purelink™ RNA Mini- High Yield	RNA purification	RT	Ambion, Life Technologies #12183025
qScript® cDNA Synthesis kit	cDNA synthesis	-20 ºC	QuantaBio #95048-025
SYBR Green PCR Master Mix	qRT-PCR	-20 ºC	Applied Biosystems #4367659

Table 5. Details of cell culture reagents

Reagent	Storage	Source & Cat. No.
DMEM	4 ºC	Gibco Invitrogen #41966
DMSO	RT	Sigma-Aldrich D2650
FBS	-20 ºC	Gibco Invitrogen #10270-106
HEPES	-20 ºC	Sigma-Aldrich H4034
Penicillin and streptomycin	-20 ºC	Invitrogen #15140-122
Trypsin	4 ºC	Invitrogen #25300-062
Trypsin phenol-red free	4 ºC	Gibco Invitrogen #15400-054

Table 6. Antibodies used and details of usage

A. PRIMARY ANTIBODIES

Target	Raised in	Working conditions	Source & Cat. No.
AFG3L2	Mouse	WB: 1/1000 4 °C O/N	Abcam ab68023
ATF4	Rabbit polyclonal	WB: 1/1000; 4 °C O/N	Aviva Systems Biology ARP37017
ATF5	Rabbit monoclonal	WB: 1/2000; 4 °C O/N IF: 1/1000; RT 1h	Abcam ab184923
ATF6	Mouse monoclonal	WB: 1/1000; 4 °C O/N	GeneTex IMG-273
CHOP	Mouse monoclonal	WB: 1/1000; 4 °C O/N	Santa Cruz Biotechnology sc-7351
eIF2a	Rabbit	WB: 1/1000; 4 °C O/N	Cell Signaling, #9722
FGF21	Rabbit monoclonal	WB: 1/1000; 4 °C O/N	Abcam ab171941
GCN2	Rabbit	WB: 1/1000; 4 °C O/N	Cell Signaling #3302
HRI	Goat	WB: 1/1000; 4 °C O/N	Santa Cruz Biotechnology sc-21949
IRE1α	Rabbit monoclonal	WB: 1/1000; 4 °C O/N	Cell Signaling #3294
LONP1	Rabbit	WB: 1/1000; 4 °C O/N	Sigma-Aldrich SAB1411647
mtHSP70	Mouse monoclonal	WB: 1/1000; 4 °C O/N	Abcam ab2799
OPA1	Rabbit	WB: 1/1000; 4 °C O/N	Novus Biologicals NB110-55290
OxPhos cocktail	Mouse	WB: 1/1000; 4 °C O/N	Abcam ab110413
PERK (C-terminal)	Rabbit	WB: 1/1000; 4 °C O/N	Sigma-Aldrich P0074
phospho-eIF2a (Ser51)	Rabbit	WB: 1/1000; 4 °C O/N	Cell Signaling #9721
phospho-GCN2 (T899)	Rabbit	WB: 1/1000; 4 °C O/N	Abcam ab75836
phospho-IRE1a (S724)	Rabbit	WB: 1/1000; 4 °C O/N	Abcam ab48187
phospho-PERK (Thr980)	Rabbit	WB: 1/1000; 4 °C O/N	Cell Signaling #3179
phospho-PKR (Thr451)	Rabbit monoclonal	WB: 1/1000; 4 °C O/N	Santa Cruz Biotechnology sc-101784
PKR	Rabbit	WB: 1/1000; 4 °C O/N	Santa Cruz Biotechnology sc-1702
PORIN (VDAC1)	Mouse monoclonal	WB: 1/1000; 4 °C O/N	Abcam ab14734
TFAM	Rabbit	WB: 1/1000; 4 °C O/N	Abcam ab131607
TIMM44	Mouse monoclonal	WB: 1/1000; 4 °C O/N	BD Biosciences #612582
Vinculin	Mouse	WB: 1/1000; 4 °C O/N	Abcam ab18058
α-tubulin	Mouse monoclonal	WB: 1/8000; 4 °C O/N	Sigma-Aldrich T5168
β-actin	Mouse monoclonal	WB: 1/20000; 4 °C O/N	Sigma-Aldrich A1978

B. SECONDARY ANTIBODIES

Target	Conjugated	Working conditions	Source & Cat. No.
Mouse	HRP	WB: 1/10 000; 1h RT	Jackson ImmunoResearch #715-035-150
Rabbit	Alexa-488	IF: 1/1000; 45min RT	Thermo Fisher Scientific A11034
Rabbit	HRP	WB: 1/10 000; 1h RT	Jackson ImmunoResearch #711-035-152

Table 7. Primers sequences used

A. REAL TIME PCR SYBR GREEN PRIMERS

Symbol	Forward	Reverse
actin	GGTCATCACTATTGGCAACGA	GTCAGCAATGCCTGGGTACA
atf4	CTCATGGGTTCTCCAGCGACAAG	GTCAAGAGCTCATCTGGCATGG
atf5	CCTTGCCCTTGCCCACCTTTGAC	CCAGAGGAGGAGGCTGCTGT
clpp	GCAACAAGAAGCCCATTCAT	CCCCTCTTCTCCAAACACTG
fgf21	ATGGAATGGATGAGATCTAGAGTTGG	TCTTGGTGGTCATCTGTGTAGAGG
hsp10	GGCCCGAGTTCAGAGTCC	TGTCAAAGAGCGGAAGAAACTT
hsp60	TCTTCAGGTTGTGGCAGTCA	CCCCTCTTCTCCAAACACTG
lonp1	CCTGACTGCAGAGATCGTGA	CCCATGTCGCTCAGGTAGAT
opa1	CTGAGGCCCTTCTCTTGTTAGG	CTGACACCTTCCTGTAATGCTTG

B. mtDNA COPY NUMBER ASSESSMENT PRIMERS

Symbol	Forward	Reverse
mtDNA12S	ACCGCAAGGGAAAGATGAAAG	AGGTAGCTCGTTTGGTTTCGG

C. GENOTYPING PCR PRIMERS

Symbol	Forward	Reverse
opa1 floxed	ATTGTCTGATGGCAGTGGTG	TTCTGTGCACACTGGTGTCC

6.2 In vivo methodology

6.2.1 Animal care

All animal experiments were done in compliance with the guidelines established by the Committee on Animal Care of the University of Barcelona. Mice were kept under a 12-h dark/light cycles and provided with a standard chow-diet and water *ad libitum*.

6.2.2 Generation of liver-specific OPA1 knockout model

$Opa1^{loxP/loxP}$ mice were previously generated in our group by Dr. Noguera and Dr. Diaz. This strain has 2 loxP recombination sites flanking the exon 5 that is common to the 5 mouse isoforms of OPA1 gene. In the presence of Cre recombinase, the exon 5 is removed, eliminating the formation of all isoforms of OPA1 isoforms.

To generate the liver-specific OPA1 knockout mouse model, we started our breeding strategy with crossing 2 females carrying the transgene Cre recombinase under the control of Albumin promoter specific to liver, thus yielding a transgene called Alb-Cre with an $Opa1^{loxP/loxP}$ male. The Alb-Cre transgene is first expressed at day E18 of the embryonic development in mice. A first generation of heterozygous mice $Opa1^{+/loxP}$ and Cre + or Cre- was obtained. Heterozygous mice crossed each other to get Alb-$Cre^{-/-}$ $Opa1^{loxP/loxP}$ (loxP) and Alb-$Cre^{+/-}$ $Opa1^{loxP/loxP}$ (L-OPA1 KO) mice.

In the different experiments carried out in this thesis using this animal model, animals with the genotype Alb-$Cre^{-/-}$ $Opa1^{loxP/loxP}$ have been used as controls of L-OPA1 KO mice. 8- to 12-week-old loxP and L-OPA1 KO mice were used in all experiments, unless indicated. Mice were in a C57BL/6J pure genetic background.

6.2.3 Model validation by genotyping

The genotyping of liver-specific OPA1 KO was performed by PCR amplification (section 7.8.1.3) of specific genomic DNA fragments from mouse tail tips.

6.2.3.1 Genomic DNA purification from mouse tail tips and detection

This DNA purification protocol is based on the digestion of a 0.5 cm tail piece of length with protein K and the subsequent precipitation of the DNA with ethanol. Mouse tail tips are obtained at the time of weaning of the mice and are stored in tubes eppendorf a -20 ºC.

The detailed Procedure of DNA purification is as follows:

1. Mouse tail tips (1-2mm) are obtained by a small incision in the tail at weaning and kept at -20 °C until processing.
2. Digest tail tips O/N at 55 °C and 450 rpm shaking, in 500 µl of Lysis Buffer [5mM EDTA; 200mM NaCl; 0.2 % SDS; 100mM Tris-HCl (pH8.5)] + 10 µl of Proteinase K.
3. Inactivate Proteinase K by 2 min 80 °C and cool down on ice.
4. Spin at 18,000 x g for 15 min at RT
5. Transfer supernatant to new eppendorf tubes containing 500 µl isopropanol.
6. Shake by inversion 10 times.
7. Spin at 14,000 x g for 10 min at R. Discard supernatant.
8. Wash pellet with 500 µl of EtOH 70 %.
9. Spin at 14,000 x g for 5 min at RT. Discard supernatant and let pellets dry capsized for 1h.
10. Before PCR, DNA is resuspended in 500 µL of water and heated for 2 min at 65 °C.

6.2.3.2 Genotyping

To detect the presence of one of the loxP sites, the oligonucleotides in Table 7.C. With this pair of starters, an 800 basepairsbp band is expanded into the case of wild type mice and a band of 1100bp in the case of $Opa1^{loxP/loxP}$ mice, thus in heterozygous mice the 2 bands are detected (Figure 47.A). Mice have also been genotyped to detect the presence or absence of Cre recombinase with the corresponding primers (Table7.C), thus the presence of a band of 600 bp indicates that the mice are Cre positive, while their absence indicates that they are Cre negative (Figure 47.B).

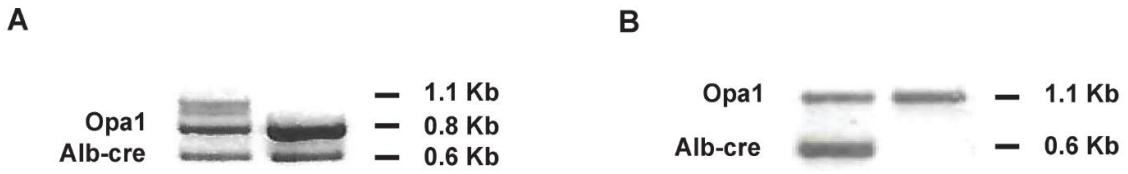

Figure 47. Genotype confirmation by PCR. (A) Genotyping PCR products of heterozygous (1.1 + 0.8 Kb bands; left lane) and wild type mice (0.8 Kb band; right lane). Both are cre positive represented by 0.6 Kb band in both lanes. (B) Genotyping PCR products of L-OPA1 KO (1.1 Kb band; presence of cre band; left lane) and loxP mice (1.1 Kb band; presence of cre band; right lane)

PCR master mix is prepared for the total number of samples of the run. Primers used are detailed in Table 6. For each sample the mix contains:

- 18.8 µl H2O
- 2.5 µl 10xBuffer
- 0.5 µl dNTPs (10 mM each)
- 0.5 µl of each primer at 10 µM
- 0.125 µl DNA Pol
- 1.5 µl DNA.

The PCR program is:

4 min at 95 °C

35 cycles of (30s 95 °C, 30s 60 °C and 3min 72 °C)

10 min 72 °C

Kept at 4 °C.

PCR products are resolved in an agarose gel and document the resulted bands using a trans-illuminator.

6.2.4 High-fat diet feeding

Such experiments were performed ad libitum for the 16 weeks. They imply extra housing care: due to diet fatty/slimy properties, and cages were changed once a week. The

diet used in the present study was High Fat Diet - 60% calories from fat, mainly lard and soybean oil.

6.2.5 Body composition measurement: Echo-MRI

Body composition was assessed by means of Echo-MRI equipment. The Echo-MRI utilizes quantitative nuclear magnetic resonance (qNMR) method to determine body fat mass, lean mass and free fluids very fast and easy, without the need for anesthesia utilization and free of radiation, body invasion, or other health issues. There are analyzers available on the market with a suitable dimension of the magnet and coil for normal and obese mice and rats, and even larger species such as dogs, piglets, and humans in clinical applications (Mitchell 2011). Typical scan times range from less than one minute to less than four min in different specific devices and applications. The accuracy of this method critically depends on the calibration strategy. Oil samples are used as calibration equivalents for lean mass and fat mass. Small glass tubes containing different volumes of physiological salt solution are used to calibrate free fluids.

To perform the scans the animals on chow diet and high-fat diet were placed in 40 and 60 x g animal holders, respectively and subjected to 1 minute-scan in triplicate. Mice need no anesthesia and no special preparation before measurement.

6.2.6 Food intake measurements

To monitor food intake, mice were housed individually and acclimatized for 1 week before the experiment. Feeding was measured as food disappearance in 24h periods for 7 consecutive days. The existent wasting was considered equal in every cage.

6.2.7 Glucose Tolerance Test

The glucose tolerance test is a technique used to evaluate the ability of glucose utilization presented by an individual. The technique is based on the administration of a glucose load and in the follow-up of its levels in the blood over time. In case insulin resistance is present, it will reach higher levels of blood glucose and it will take longer to return to the basal glycemic state. Each mouse was kept under a cardboard box to diminish stress. All unnecessary rumbles were avoided.

Procedure:

On the day before the Glucose Tolerance Test (GTT) mice are fasted 16h overnight.

1. GTT is initiated the following day with the measurement of glucose levels at timepoint 0 by means of a small tail incision in the animal which a drop of blood is extracted and applied to the glucometer strip (Accu-Check);
2. 2 g glucose / kg body weight [stock: glucose solution 20% (w / v)] is administrated via intraperitoneal (IP) injection to the animal by means of 0.5 mL syringes and 29G needles.
3. Blood samples are collected 5, 15, 30, 60, 90 and 120 min after the administration of glucose and glycemia is measured with the glucometer.
4. Each time, 50 µl of blood using microvettes with EDTA (Starstedt) are also obtained to later determine insulin levels in plasma.
5. The extracted blood is centrifuged at 2,500 x g for 20 min at 4 ºC, the supernatant is collected (plasma) and frozen at -20 ºC.

The plasma inulin concentration was determined using Ultra-Sensitive Mouse Insulin ELISA kit following the directions of the commercial house.

6.2.8 Insulin Tolerance Test

The Insulin Tolerance Test (ITT) has been performed in L-OPA1 KO mice 2 weeks after the GTT to evaluate the degree of responsiveness to insulin. The procedure is very similar to the GTT but the IP administration of insulin instead of glucose. The ITT was performed in mice after a 4h fast, which promotes glucose levels homogeneity. Upon 4h fasting, glycemia is measured at time 0 with the glucometer and then animals are injected intraperitoneally 0.75 U of insulin (Humalog) per kg. The concentration of glucose in blood is measured at 15, 30, 45, 60 and 90 min after the injection.

6.2.9 Blood Sampling and Plasma Measurements

Blood collection was generally done by tail/facial vein extraction, and exclusively by direct cardiac withdraws during necropsy. Microvettes with EDTA (Starstedt) were used.

Briefly afterwards, blood samples were centrifuged for 20 min at 2500 x g, 4 ºC, and plasmas was carefully obtained and kept at -80 ºC.

i. ELISA analysis

Plasma concentrations of insulin, FGF21 and glucagon were measured by ELISA assay following the manufacturer's instructions. Briefly, these assays are a Sandwich ELISA based, sequentially, on:

1. Capturing the molecules of interest from samples to the wells of a microtiter plate coated with a specific immobilized antibody, and binding of a second biotinylated specific antibody to the captured molecules;

2. Washing of unbound materials from samples;

3. Binding of a horseradish peroxidase conjugate to the immobilized biotinylated antibodies;

4. Washing of excess of free enzyme conjugates;

5. Quantifying the immobilized antibody-enzyme conjugates by monitoring horseradish peroxidase activities in the presence of the substrate 3,3',5,5'-tetramethylbenzidine (TMB).

6. Measuring the enzyme activity spectrophotometrically by the increased absorbance at 450 nm after acidification of formed products.

Since the increase in absorbance is directly proportional to the amount of captured molecule of interest in the unknown sample, the latter can be derived by interpolation from a reference curve generated in the same assay with reference standards of known concentrations of molecules of interest. Detailed information for each molecule detection procedure is depicted in table 8.

Table 8. Details for ELISA measurement of insulin, FGF21 and glucagon
(Sample type and amount, purchase information, assay general conditions and detection method)

Metabolite	Sample	Measurement kit	Special requirements and detection
FGF21	Frozen serum 10 µl	Ultra-Sensitive Mouse FGF21 ELISA Kit Merck-Millipore Cat. No. EZRMFGF21-26K	2h incubation, RT **Standard:** 0, 0.51, 1.54, 4.63, 13.89, 41.66, 125 pg/mL **Detection:** 450 nm
Glucagon	Frozen serum 10 µl	Ultra-Sensitive Mouse Glucagon ELISA Kit CrystalChem Cat. No. 81518	Overnight incubation, 4ºC **Standard:** 0, 0.781, 1.563, 3.125, 6.25, 12.5, 25 pg/mL **Detection:** 450 nm
Insulin	Frozen serum 5 µl	Ultra-Sensitive Mouse Insµlin ELISA Kit Crystal Chem Cat. No. 90080	2h incubation, 4ºC **Standard:** 0, 0.01, 0.02, 0.04, 0.08, 0.16, 0.32 ng / mL **Detection:** 450 nm

ii. Colorimetric assays

Colorimetric assays use reagents that undergo a measurable color change in the presence of the metabolite. Briefly, all different measures were made in duplicate of samples, standards or blank control. Standard curves are prepared in parallel, and respective reagents are added and incubated as detailed in the table 9.

Table 9. Details for colorimetric assays: sample type and amount, and general assay conditions
(Sample type and amount, purchase information, assay general conditions and detection method)

Metabolite	Sample	Conditions	Source & Cat. No.
Cholesterol	Frozen serum 2 µl	15 min incubation, RT **Standard:** 0, 100, 200, 400 mg / mL **Detection:** 500 nm	BioSystems #23505
NEFAS	Frozen serum 2µl	**Reagent 1:** 10 min 37 ºC **Reagent 2:** 10 min 37 ºC **Standard:**0, 0.25, 0.5, 1, 1.5, 2, 3, 4 mmol / L **Detection:** 550 nm	FujiFilm Wako Diagnostics Cat. No.
Triglycerides	Frozen serum 2 µl	15 min incubation 37ºC **Standard:**0, 100, 200, 400 mg / mL **Detection:** 500 nm	BioSystems #23528
β-hydroxybutyrate	Frozen serum 2.5 µl	**Reagent A (A1):** 3 min incubation, RT **Reagent B (A2):** 5 min incubation, RT **Calibrator:** 10.9mg / dL **Detection:** 560 nm	BioSystems #12525

*end reactions must be protected from light

The concentration of β-hydroxybutyrate is calculated as the following:

$$\frac{(A_2 - A_1)_{Sample} - (A_2 - A_1)_{Blank}}{(A_2 - A_1)_{Calibrator} - (A_2 - A_1)_{Blank}} x C_{Calibrator}$$

6.3 Methodology for ex vivo studies

6.3.1 Respirometry

The correct measurement of mitochondrial oxidative phosphorylation is key in the study of cellular energy metabolism and it contributes significantly to the study of mitochondrial physiology. One of the most widely used methods to estimate the function and dysfunction of mitochondria is the measure of on-site oxygen consumption in tissues homogenate of liver, brown adipose tissue (BAT) and white adipose tissue (WAT) and *in situ* O_2 consumption in permeabilized muscle fibers. These approaches allow to functionally characterize mitochondria in a more physiological situation and has important advantages over those mitochondria isolated. First of all, this method only requires some few milligrams of tissue, allows the analysis of mitochondria inside of the cellular context, in its physiological situation and maintaining the essential interactions with the cytoskeleton, the nucleus or the ER while the standard procedures of subcellular fractionation, based on the differential centrifugation of tissue homogenates (Frezza et al. 2007) present major drawbacks, as it needs a large amount of biological material to obtain an optimal quality of the preparation mitochondrial and in addition, the interactions between the mitochondria and other organelles are lost.

To analyze the global function of the mitochondrial respiratory chain, through the consecutive addition of different substrates and inhibitors in the oxygraph-2k chambers.

6.3.1.1 Equipment

To perform the experiments of O_2 consumption the OROBOROS Oxygraph-2k was used, a variant of the Clark oxygen electrode. This device is characterized by its high resolution in the measurements even in the case of low respiratory activity or low levels of O_2. In addition, it allows the measurement of the O_2 consumption in different types of samples, from isolated mitochondria to cells or small amounts of biopsies. Therefore, Oxygraph-2k has multiple applications, both clinics - diagnosis of mitochondrial disease, myopathy and other neuromuscular disorders (Pecina et al., 2004; Winkler et al., 2005; Boushel et al., 2007; Skovbro et al., 2011) - as in the field of the basic research - studies of the cellular function, apoptosis, necrosis, study of the stress oxidative and aging (Gnaiger et al., 2000; Hütter et al., 2006).

The data analysis has been carried out with the DatLab 4 and how-to-instructions manual of this software, as well as assembly and maintenance of the device and the polarographic sensors of oxygen can be consulted on the company's website, www.oroboros.at.

6.3.1.2 Preparation of media for tissue preparation and respiratory assay

Different media are used in high-resolution respirometry assays including media for tissue preparation and respiration buffer (MiR05 - Mitochondrial Respiration Medium; table 10.B). These media must contain compounds such as sucrose, mannitol, KCl, KMES or K-lactobionate to maintain the osmolarity similar to the physiological one. They are also necessary additional compounds to preserve the integrity of mitochondria, such as taurine and the bovine serum albumin (BSA), which are used as stabilizers of biological membranes and as ROS scavenger. Finally, these media also contain Mg^{2+}, since the activity of many enzymes depend on the presence of this cation, and EGTA as Ca^{2+} chelator.

6.3.1.3 Liver tissue homogenization

For liver tissue preparation, upon sacrificing animals by cervical dislocation, the following protocol was performed:

1. Harvest liver tissue, rinse free blood with ice cold lysis buffer (table 11) and transfer the tissues into a glass potter;
2. Homogenize the liver tissue in 4 mL of ice-cold lysis buffer, using a Teflon pestle operated at 800 rpm. and 15 strokes;
3. Centrifuge tissue homogenates at 1300 x g at 4 ºC for 10 min;
4. Collect the supernatant and quantify protein amount;
5. Transfer 500 μg of liver protein homogenate into the O2k-Respirometer chamber containing 2 mL of air-saturated MiR05 medium.

6.3.1.4 Measurement of oxygen consumption

All respiration measurements were made in duplicate and using the following protocol:

1. With a 25 mL Hamilton micro-syringe it is added to the 10mM glutamate chambers and 2 mM malate to record the consumption of basal oxygen using substrates for complex I. We denominate this basal respiration as state 4.

2. 2.5 mM ADP (saturation concentration) is added. The oxygen consumption stimulated by the ADP is the so-called respiratory state 3 (I).

3. 10 mM cytochrome c is added as a quality control of mitochondria, since it allows to check the integrity of the external mitochondrial membrane. An increase in respiration by the presence of cytochrome c would indicate that the external mitochondrial membrane is damaged. No stimulation was observed.

4. Then 10 mM succinate is added. The addition of succinate allows us to measure the respiratory capacity in the presence of substrates for the complexes I + II, to which we designate as state 3 (I+II).

5. Stepwise addition of 0.1 mM FCCP is done until it reaches the maximal oxygen consumption. Reaching the optimal FCCP concentration for maximal flux is important to avoid inhibitory effects. This state measures the maximum capacity of the electron transport chain, since FCCP uncouples respiratory chain of the ATP synthesis.

6. 0.5 mM rotenone is added, a specific inhibitor of the complex I. This will decrease the rate of respiration since it is only supported by the complex II substrates.

7. Finally, 2.5mM antimycin A, inhibitor of complex III, is added. This state is considered non-mitochondrial respiration. This state is called rox (residual oxygen consumption).

To express the results as mitochondrial oxygen consumption, this rox value of the above value is subtracted of the previous values.

6.3.2 Histological analysis

Mice were killed by cervical dislocation and tissue sampling is done immediately postmortem. Samples were embedded in OCT solution prior liquid nitrogen-cooled isopenthane or fixed with at least 10 parts of formaldehyde 4% solution. Livers are rinsed

once with phosphate buffered saline (PBS) prior each Procedure to remove any residual blood.

From here the members of Histopathology Facility of IRB processed the samples by performing tissues samples embedding, sectioning, microscope slides preparation and staining/immunohistochemistry. For light microscopy, liver sections were stained with hematoxylin and eosin (H&E). For lipid content, tissue slices were stained with Oil Red. Immunohistochemistry was performed with the indicated antibodies under indicated conditions (Table 6).

6.4 In vitro methodology

6.4.1 Cell culture

In the present work, Mouse Embryonic Fibroblasts (MEF) are used as a cellular model. Cells, if is not specified were grown in Dulbecco Modified Eagles Medium (DMEM) with 10% Fetal Bovine Serum (FBS), 25 mM of HEPES, 100 U/mL and 100 µg/mL of penicillin/streptomycin respectively, at 37oc in a humidified atmosphere of 5% CO2/95% air to maintain the pH of the medium. The medium is renewed three times per week. Since these cells show highly proliferating rates, the cultures might be sub-cultured at least twice a week.

6.4.2 Culture media

DMEM with 4.5g/L of D-glucose, L-glutamine and pyruvate have been used as basal medium for cultured cells in the present thesis. The culture media must be kept at 4 ºC until the expiration date. Once supplied with additional components, media should not be stored for more than one month at 4 ºC, as the components can precipitate or degrade. The medium for cell growth is prepared with 10% of FBS, 25 mM of HEPES and penicillin/streptomycin at 100 U / mL/100 µg / mL, respectively. FBS provides to the medium a high content of embryonic growth promoting factors that are necessary for cellular proliferation. FBS must be inactivated prior to use, the treatment is performed at 56 ºC for 30 min. FBS must be kept at -20 ºC. HEPES (4-(2-hydroxyethyl)-1-piperazineethanesµlfonic acid) 1.25 M pH 7.4 is

used as buffering agent in cell culture media, providing a buffer solution additional to the bicarbonate of the medium. HEPES must be keep at -20 ºC. Penicillin and streptomycin are two different types of antibiotics that prevent bacterial growth and minimize culture contamination. Penicillin inhibits the synthesis of the bacterial growth and streptomycin inhibits bacterial protein synthesis. Both antibiotics must be kept at -20 ºC. Culture media needs to be replaced often, the frequency increases with the cell metabolic rate. Normally culture media is supplied with a pH indicator that change color media from red to yellow when the media needs to be refreshed. Pre-heating (37 ºC) the media and other solutions before use is recommended to minimize the exposure of cells to stressful conditions.

6.4.3 Maintenance and subculture

The number of cells growing in a common space cannot exceed a certain maximum, which is determined by the confluence on the surface. Once the maximum limit is reached, the culture must be divided by splitting. This process is known as sub-culturing or passaging, the medium is removed, and the cells are transferred from the previous cell plate into a new cell plate with fresh growth medium, enabling the further propagation of the cell line. Cells are seeded on 10 cm dishes and attached to the surface through several proteins belonging to the cellular membrane. Maintenance cultures are normally plated at low confluences, with 10% being the minimal percentage recommended. Once cells reach a threshold confluence (70 %), the culture needs to be sub-cultured by splitting and seeding into a new dish:

1. Cell culture medium and trypsin are pre-warmed at 37 ºC bath.
2. Cell culture media is removed and discarded from the culture plate.
3. Cells are washed using PBS (approximately 5 mL per 10 cm cell culture dish). The wash solution is added to the side of the cell plate gently, to avoid cell layer disturbing.

Note: The wash step removes any traces of serum, calcium, and magnesium that would inhibit the action of the trypsin reagent.

4. The wash solution is removed and discarded from the culture plate.

5. Trypsin is added to the side of the flask (3mL per 10 cm cell culture dish) and must cover the entire cell layer. Trypsin is a serine protease that disrupts the proteins bonding the cultured cells to the dish.

6. The culture plate is incubated at 37 ºC for 3 min in the incubator.

7. Once the cells have been detached, 6 mL of pre-warmed growth medium is added to the cell plate. The medium is dispersed by pipetting over the cell layer surface several times to homogenize.

8. Transfer the cells to a 15 mL conical tube and centrifuge then at 800 x g for 5 min.

Note: this step is only needed in cell lines that are slightly sensitive to trypsin. In other cases, the dilution with the media is enough.

9. The supernatant is removed, and the cell pellet is resuspended in 10 mL of pre-warmed complete growth medium. 12 µL of cell suspension are removed for counting.

10. The cells are counted in a Neubauer chamber.

11. The cell suspension is diluted to the seeding density desired. The seeding density is a function of the time and amounts in which cells are needed.
12. Finally, the cells are returned to the incubator.

Procedure for counting cells in a Neubauer chamber:

The cells are counted using a Neubauer chamber. The two semi-reflective rectangles are the counting chambers. Each chamber is engraved with a laser-etched grid of perpendicular lines. The device is carefully crafted so that the area bounded by the lines is $1mm^2$, and the depth of the chamber is 0.1 mm, making possible to count the number of cells in a specific volume of fluid, and thereby calculate the concentration of cells in the mixture the sample come from.

1. 12 µL of the cell suspension is applied between the coverslip 24 x 50 mm (Menzel-Glaser) and the Neubauer chamber (Neubauer improved de Brand Gmbh). The cell

suspension is applied to the edge of the coverslip to be sucked into the void by capillary action which completely fills the chamber with the sample.

2. The number of cells in the chamber can be determined by direct counting using a microscope (Nikon Eclipse TS100). The Neubauer chamber contains 4 squares (1 x 1 mm). The number of cells per each square is counted and the average of the 4 squares is calculated

3. To calculate the number of cells per mL of cell suspension, the average value is multiplied per 10^4.

6.4.4 Freezing and defrosting

Both freezing and thawing out procedures must be carefully performed to minimize the risk of cellular death. The best method for cryopreserving cultured cells is storing them in liquid nitrogen in complete medium in the presence of a cryoprotective agent, such as dimethylsulfoxide (DMSO). Cryoprotective agents reduce the freezing point of the medium and also allow a slower cooling rate, greatly reducing the risk of ice crystal formation, which can damage cells and cause cell death. The cultured cells must be frozen at a high concentration and at as low a passage number as possible to have sufficient stock and preserve their original characteristics, respectively. The cells must be 90% confluence in the culture plate and viable before freezing.

6.4.5 Procedure for freezing cells:

1. The cells are detached from the culture plate using trypsin as it has been described in Procedure point 7.5.2

2. Once the cells have been detached, 10 mL of pre-warmed growth medium is added to the cell plate. The medium is dispersed by pipetting over the cell layer surface several times to homogenize.

3. The cells are transferred to a 15 mL conical tube and centrifuged at 800 x g for 5 min at RT;

4. The supernatant is removed without disturbing the cell pellet, and then the cell pellet is resuspended in 5 mL of complete growth medium with 10% DMSO sterile (v/v). The exposure of the cells to the solution of DMSO at room temperature should be kept to a minimum for toxic reasons.

5. The cell suspension is dispensed in 5 aliquots of 1 mL into sterile cryogenic storage vials, which are on ice.

6. The cells are frozen at -80 °C in the freezer for 24 hours.

7. The next day the cells are immersed in the liquid nitrogen tank. The cells can be stored in liquid nitrogen for years. Defrosting must be rapidly performed to minimize the exposure of cells to DMSO at RT to minimize the risk of cellular death.

i. Procedure for defrosting cells:

1. Cell culture medium is pre-warmed at 37 ºC bath.

2. The cryogenic storage vial is taken from the liquid nitrogen tank and defrosted in a 37 ºC bath for 1 minute.

3. The cell suspension is then diluted in a 15 mL conical tube containing 10 mL of pre-warmed fresh complete growth medium, homogenized and centrifuged at 800 x g for 5 min at RT.

4. The supernatant is removed without disturbing the cell pellet to eliminate DMSO, and then the cell pellet is resuspended in 10 mL of pre-warmed fresh complete growth medium.

6.4.6 Mycoplasma test

In addition to bacterial and fungal contaminations, which are easily detectable and treatable, other types of contamination can critically affect the culture without being readily apparent. Mycoplasma cell culture contamination is very common; it can produce abnormal behavior of the cells such as decrease of the cell culture growth rates, loss of cell adhesion, decrease in the transfection efficiency, as well as, DNA, RNA and protein synthesis alteration. To confirm the type of contamination and the species of parasite involved, several commercially available tests are used. In the present thesis periodic controls have been

performed to discard mycoplasma contamination using the EZ-PCR Mycoplasma Test Kit, which is based on PCR amplification of the mycoplasma genome. It contains primers with broad range that allow the detection of twelve mycoplasma species. A sample of 1 mL of culture media that has been in contact with the cells for 48 hours is used as a template for the reaction. If the result is positive the cells are eliminated or treated with BM cyclin kit.

6.4.7 Cell decontamination

BM cyclin kit is an effective mycoplasma removal agent and is used to treat cell lines infected by mycoplasma. BM cyclin is a well-established anti-mycoplasma reagent; treatment with BM Cyclin includes three or more cycles. Each cycle grows cells for 3 days in BM Cyclin 1 alternating with 4 days in BM Cyclin 2 containing medium.

Protocol

1. Remove culture medium from culture vessels by aspiration and add new medium containing BM Cyclin 1 at a final concentration 10 g / mL. Let it act for 3 days.
2. Sub-cultivate the cells for another 3 days in the usual way.
3. The next day remove culture medium and add new culture medium containing BM Cyclin 2 at a final concentration 5g / mL. Let it act for 4 days.
4. Repeat the cycle twice.
5. Check for mycoplasma contamination

6.4.8 Measurement of mitochondrial membrane potential

Measurement of mitochondrial membrane potential was performed using TMRM from Invitrogen. TMRM is a fluorescent dye that accumulates in mitochondria in a potential-dependent manner. The TMRM emits fluorescence at 573 nm when it is excited at 540 nm. Thus, TMRM positive cells can be quantified using flow cytometry. The concentration of TMRM in the mitochondria increases proportionally to the membrane potential, and its accuracy is validated using simultaneously carbonyl cyanide m-chlorophenyl hydrazone (CCCP). CCCP is used to dissipate the mitochondrial membrane potential decreasing the TMRM incorporation and the fluorescent signal. Thus, CCCP allows determining the

unspecific fluorescence signal, and is used as a blank. The stock solutions of TMRM and CCCP are prepared using DMSO, at 500 μM and 1 mM, respectively, and they are stored at -20 ºC avoiding light exposure.

Protocol for measurement of mitochondrial membrane potential

1. The cells are seeded in a 6-well plate and the next day the treatment is performed.
2. Next day the media is removed and cells are washed with PBS;
3. 1 mL of growth medium ± CCCP (30 μM) is added to each 6-well plate. The cells are incubated with CCCP for 30 min at 37 ºC. Duplicates are performed for each condition.
4. Then, the medium is removed and 1 mL of growth medium + TMRM (100 nM) is added to each 6-well plate. The cells are incubated 30 min at 37 ºC;
5. The cells are washed twice in PBS to eliminate dye excess.
6. The cells are tripsinized and diluted in 500 μL of growth medium.
7. The fluorescence emitted by the cells is analyzed by flow cytometry Sony SA3800 in the Centres Cientifics i Tecnològics de la Universitat de Barcelona (CCiTUB).

6.4.9 Immunofluorescence studies

Protocol for ATF5 detection by immunocytochemistry

1. The cells are seeded in 12mm round coverslips placed on a 6-well plate
2. Next day the media is removed, and cells are washed with PBS prior Mitotracker treatment
3. Incubate cells with mitotracker Deep Red (Cf=50-100nM) in culture media for 2 min at 37 ºC;
4. Rinse cells with culture medium and incubate for 10’ at 37 ºC;

5. Wash cells briefly with PBS for 5 min before fixation

6. Cells are incubated with paraformaldehyde 4% (1 mL for each 6-well plate) for 15 min at RT to fix the cells. Light exposure is avoided.

7. Wash cells with PBS for 10 min, 2 times

8. Treat cells with each quenching solutions for 10': glycine 20mM and NH4Cl 50mM

9. Wash with PBS (3x) for 10 min

10. Cell permeabilization: PBS + 0.1% Triton for 10 min.

11. Blockade: PBS+10% FBS for 30'

12. Incubate with primary antibody in blockade buffer 1h at RT

13. Wash with PBS for 10 min, 3 times

14. Incubate with secondary antibody 45 min at RT

15. Wash with PBS 1x for 10 min

16. To specifically dye the cell nucleus, incubate the cell with DAPI-PBS (1:2000) for 10 min

17. Then, carefully wash with PBS for 10 min, 2 times

18. Each round coverslip is washed quickly in filtered milliQ water to eliminate the salts contained in PBS solution and dried with a tissue paper to eliminate water.

19. Mount the round coverslips disposing drops of 10 µL of Fluoromount® on a microscope slide. The side with cells of the coverslip must be in contact with Fluoromount.

20. The microscope slides with the round coverslips are incubated overnight at room temperature avoiding light exposure.

21. The microscope slides are stored at 4°C avoiding light exposure.

6.4.10 Cell treatments and genetic manipulation

6.4.10.1 Chemical treatments

Cultured cells are exposed to a variety of compounds to study and evaluate the role of ER stress and phosphorylation-eIF2α in the signaling pathways involved in the L-OPA1 KO phenotype. To prevent insoluble problems, all the compounds used in the thesis were dissolved in either DMSO or absolute ethanol. A final 1% DMSO or 1% absolute ethanol, without showing toxic effects, were established in the media exposed to cells in the different conditions (details in table 10). The compounds should reach the cell and be introduced without compromising cell survival. In the present thesis we performed assays to block the the activity of p-eIF2α in MEF OPA1$^{-/-}$ cells. To inhibit the phosphorylation-eIF2α and inhibit the activity of p-eIF2α, 1μM ISRIB was used (details in table 10).

Table 10. Details for cell treatments
(Treatment applied, concentration and incubation times)

Treatment	Concentration	Solvent (1%)	Incubation time
ISRIB	1μM	DMSO	24h

Upon treatments, cells were harvested for protein and RNA extraction, as described in sections 7.5.2 and 7.5.3 of Material & Methods and frozen until needed for studies.

6.4.10.2 Generation of ATF5$^{-/-}$ MEF cells: transient transfection using CRISPR-Cas9 technology

CRISPR/Cas9 technology enables the rapid and efficient generation of total loss-of-function mutations in a targeted gene in mammalian cells, allowing the establishment of a new cell line, thereby creating a CRISPR-induced knockout clone. The generation of these clonal cell lines serve as crucial tool for exploring protein function, analyzing the consequences of gene loss or investigating the specificity of various biological reagents.

To generate ATF5$^{-/-}$MEF cells Santa Cruz CRISPR/Cas9 products are used, as described below in table 11. Plasmid Transfection Medium is a reduced-serum modification of Eagle's Minimal medium, buffered with HEPES and sodium bicarbonate, and supplemented hypoxanthine, thymidine, sodium pyruvate, L-glutamine, trace elements, growth factors and phenol red, suitable for addition to CRISPR/Cas9 Plasmid suspension

and to Plasmid Transfection Reagent, immediately prior to cell transfection. UltraCruz™ Transfection Reagent delivers CRISPR/Cas9 Plasmid into cells with minimal cell toxicity and enables highly transfection DNA; enables highly efficient DNA transfection.

Table 11. Details for CRISPR/Cas9 technology used
(Working solutions, preparation conditions and catalogue number – Cat.No.)

Working solutions	Preparation	Products & Cat. No.
Solution A	For each transfection, dilute 2.0-3.0 µg of Plasmid DNA into antibiotic-free Plasmid Transfection Medium to bring final volume to 150 µL. Vortex for 1-2 seconds	Plasmid Transfection Medium sc-108062
Solution B	For each transfection, dilute 5.0-15 µl of UltraCruz™ Transfection Reagent: with enough Plasmid Transfection Medium to bring final volume to 150 µl. Vortex 1-2 seconds	UltraCruz™ Transfection Reagent sc-395739

Plasmids DNA consist of ATF5 specific guideline of 20nt RNA, obtained from the GeCKO library (v2), which direct the Cas9 protein to generate a double-stranded cut (DSB) specifically in the DNA of the gene (Figure 48).

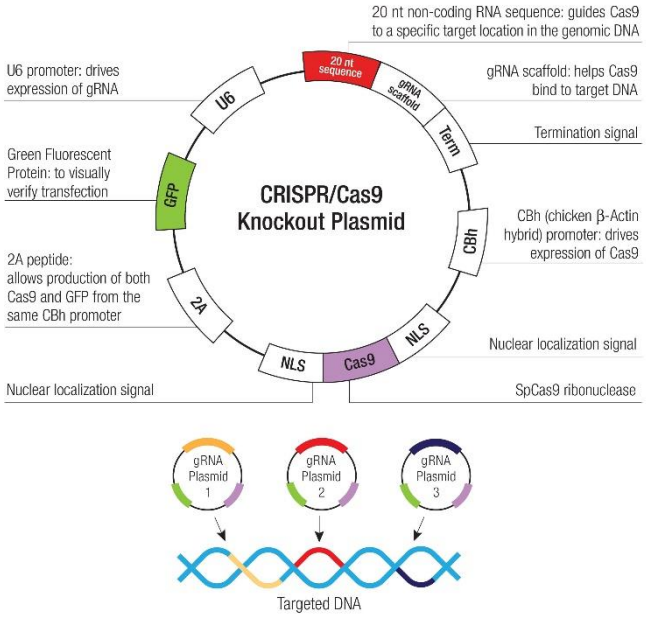

Figure 48. Breaking-down of the double chain (DSB) directed by CRISPR / Cas9 technology

Protocol

1. Seed approximately 2.5 x10^5 cells per well in a 6-well tissue culture plate, 24 hours prior to transfection. Grow cells to a 70-90% confluency in antibiotic-free normal growth medium supplemented with FBS. Healthy and sub-confluent cells are required for successful CRISPR/Cas9 associated plasmid transfection.

2. Add the Plasmid DNA solution (Solution A) dropwise directly to the dilute UltraCruz™ Transfection Reagent (Solution B) using a pipette. Vortex immediately and incubate for no less than 5 minutes at room temperature.

3. Add the 300 µl Plasmid DNA/UltraCruz™ Transfection Reagent Complex (Solution A + Solution B) dropwise to well. Gently mix by swirling the plate.

4. Incubate the cells for 48-72 hours under conditions normally used to culture the cells. No media replacement is necessary.

5. After incubation, successful transfection of CRISPR/Cas9 KO Plasmid may be visually confirmed and sorted by detection of the green fluorescent protein (GFP)

6.5 Molecular Biology Techniques

6.5.1 DNA protocols

6.5.1.1 General considerations

The manipulation of DNA must be performed using sterile material to avoid DNAses and exogenous DNA contamination. The material can be sterilized using autoclave 20 min at 120 ºC and 1 atmosphere of pressure. The working bench surface and the micropipettes should be carefully cleaned with 100% ethanol, and all solutions and reagents must be prepared with ultra-pure water and then further sterilized by autoclaving or filtered by 0.22 µm diameter filters. DNA samples must be kept on ice when preparing an experiment, and never vortex genomic DNA. Genomic DNA is stored at 2-8 ºC.

6.5.1.2 DNA purification from liver tissue

Total genomic DNA was extracted from cells from using DNeasy® Blood & Tissue Kit columns following the manufacturer's instructions:

1. Add 10 µl of protein K stock solution (20 mg / mL) to 290 µl of lysis buffer and add this mix to 25 mg of frozen liver tissue. The composition of the lysis buffer is 100 mM Tris-HCl pH 8.5; 200 mM NaCl; SDS 0.2% (w / v) and EDTA 5mM.
2. Incubate at 56 ° C for 16 hours in agitation (400rpm)
3. Resuspend in pellet fractions in 200 µL of PBS.
4. Add 20 µL of proteinase K to cytosolic enriched fractions or resuspended cell suspensions/pellet fractions.
5. Add 200 µL of Buffer AL. Mix thoroughly by vortexing.
6. Incubate the samples at 56 °C for 10 min.
7. Add 200 µL ethanol (96-100%). Mix thoroughly by vortexing.
8. Pipet the mixture into a DNeasy Mini spin column placed in a 2 mL collection tube.
9. Centrifuge at 6000 x g for 1 min.
10. Add 500 µL of Buffer AW1.
11. Centrifuge for 1 min at 6000 x g.
12. Add 500 µL of Buffer AW2
13. Centrifuge for 3 min at 20000 x g.
14. Transfer the spin column to a new 1.5 mL Eppendorf tube.
15. Elute DNA from cell suspensions/pellet fractions with 100 µL of Buffer AE, and cytosolic fraction with 50 µL of Buffer AE.
16. Incubate for 1 min at RT and centrifuge for 1 min at 6000 x g.

6.5.1.3 Basis of quantitative polymerase chain reaction (qPCR) using SYBR Green

Due to its sensitivity and dynamic range, PCR is the ideal technique to quantify nucleic acids. The polymerase chain reaction amplifies a DNA fragment from a DNA template. The fragment amplified is determined by the use of two primers that anchor to opposite DNA strands, and which are extended in different directions (towards each other). Thus, the fragment flanked by the primers is the amplified DNA. The enzymatic activity that catalyzes the synthesis of DNA from the primers is the DNA polymerase. This amplification relies on several cycles of three step-process:

1. Denaturalization (to generate single-stranded templates)

2. Primer annealing over the single-stranded templates

3. Chain extension, which is driven by the polymerase

Repeated cycles of synthesis and denaturation result in an exponential increase in the number of segments replicated. Several parameters determine the success of the reaction, such as the template (the quality of the DNA source), the primer annealing (the primers must be specific for the desired sequence) and the DNA polymerase. In conventional PCR, the amplified DNA product (amplicon) is detected in an end point analysis by visualizing the DNA product in an agarose gel after the reaction has finished. In contrast real time PCR offers an alternative method for qualitative and quantitative analysis measuring the accumulation of PCR products during amplification with fluorescent dyes as the reaction progresses, and data is recorded. Quantitative real time PCR (qPCR) detects a fluorescent dye and yields increased fluorescence signal with an increased amount of PCR product during the reaction. The measured fluorescence is proportional to the total amount of amplicon; the change in fluorescence over time is used to calculate the amount of amplicon produced in each cycle. Thus, real time PCR allows determining the initial number of copies of template DNA (the amplification target sequence) with accuracy and high sensitivity.

SYBR® Green is used as a dye for the quantification of double stranded DNA in quantitative real time PCR. When SYBR® Green I dye intercalates into double-stranded DNA (dsDNA) molecules, its fluorescence greatly increases. The designed primers must not form dimers, in contrary the SYBR Green will intercalate in the dimers producing unspecific fluorescence. During annealing, PCR primers hybridize to the target and form small regions

of dsDNA where SYBR® Green intercalates; the fluorescent signal slightly increases. In the exponential phase, more dsDNA is formed and more SYBR® Green dye can intercalate; higher fluorescence signal. At the end of the exponential phase, all DNA has become double stranded and the maximum amount of SYBR® Green is intercalated.

The fluorescence is measured at the end of each elongation phase. The resulting DNA-dye-complex absorbs blue light λmax = 497nm and emits green light λmax = 520 nm). The SYBR® Green PCR Master Mix is a convenient premix of the components (except primers, template and water), it is supplied in a 2X concentration and contains SYBR® Green I Dye, AmpliTaq Gold® DNA Polymerase, dNTPs, and optimized buffer components to perform real-time.

6.5.1.4 Mitochondrial DNA quantification by qPCR

The quantification of mtDNA of the liver of L-OPA1 KO and control loxP mice have been performed using qPCR in which the number of copies of mitochondrial DNA is calculated relative to the content of nuclear DNA (nDNA). The basis of qPCR it is the same as that described in section 7.5.1.3 with the difference that DNA is amplified genomic instead of complementary DNA (cDNA).

Protocol for SYBR® Green

qPCR is achieved in 384-well plates with a final volume of 16 µL for each well. Each sample is measured per duplicate, and each well contains 10 ng of cDNA. The primers are used at optimized concentration (625 nM). 6 µL of SYBR Green PCR Master Mix is added per each well and H_2O miliQ until 16 µL.

The qPCR consists of a first step of 10 min at 95 ºC and 40 cycles of two steps: one of 15 s at 95 ºC and one min at 60 ºC. After 40 cycles the melting step is performed by the thermocycler. During the melting step the DNA double helix is dissociated into single strands increasing the temperature gradually. The dissociation will be detected as a fluorescence decrease and it will be represented as a curve. The melting temperature is specific for each DNA molecule. Thus, if only one product has been amplified, there will be a unique curve. The thermocycler used in the present thesis is QuantStudio 6 Flex Real-Time PCR System (Applied Biosystems).

6.5.2 RNA protocols

6.5.2.1 General considerations

Working with RNA is more demanding than working with DNA, because of the chemical instability of the RNA and the ubiquitous presence of RNases especially on the skin and ambient dust. RNA work requires extreme caution since RNases enzymes potentially degrade any kind of RNA. Any work with RNA samples must be performed under strict conditions using gloves and sterile material. The working bench surface and the micropipettes should be carefully cleaned with 100% ethanol, and all solutions and reagents must be prepared with ultra-pure water to avoid RNases and contamination.

6.5.2.2 RNA purification and quantification

RNA extraction from tissues and cells was performed using a protocol that combined TRIzol reagent and Purelink™ RNA Mini High-Yield columns, following the manufacturer's instructions.

Liver tissue and cell material preparation

Place 20-30 mg of liver tissue slices in tubes containing 3 beads and 800 µL of TRIzol per tissue and homogenize for one 1 rounds of 30s at maximal speed in the Mini-Beadbeater cell disruptor (Bio Spec Products Inc.). In the case of cells, Harvest cells by scrapping with the chemical aid of 800 µL of TRIzol.

RNA extraction protocol

Preparations of liver tissue or cellular homogenates followed the next protocol:

1. Add chloroform (200 µL per every 800 µL of TRIzol) and mix tubes thoroughly, without vortexing, to separate aqueous and organic phases.

2. Centrifuge samples at 12,000 x g for 15 min at 4 °C and transfer aqueous phase to a new tube. From this point the protocol is accordingly to the manufacturer's instructions.

3. Add one volume of absolute ethanol to aqueous phase.

4. Transfer up to 700 µL of the sample to the spin cartridge with a collection tube.
5. Centrifuge at 12,000 x g for 30 s at RT. Discard the flow-through.
6. Repeat steps 7-8 until the entire sample is processed.
7. Add 350 µL Wash Buffer I to the spin cartridge.
8. Centrifuge at 12000 x g for 15 s at RT.
9. Add 80 µL of DNase solution to each spin cartridge:
    - 8 µL of Pure Link 10x DNase Buffer
    - 10 µL DNase stock solution (Thermo Scientific)
    - 62 µL RNase-free water)
10. Incubate 15min at RT.
11. Add 350 µL Wash Buffer I to the spin cartridge.
12. Centrifuge at 12,000 x g for 15 s at RT Discard the flow-through.
13. Add 500 µL Wash Buffer II to the spin cartridge.
14. Centrifuge at 12,000 x g for 15 s at RT Discard the flow-through.
15. Repeat steps 11-12 once.
16. Centrifuge the spin cartridge at maximal speed for 1-2 min to dry the membrane with bound RNA.
17. Add 30 µL RNase-free water warmed 70 °C.
18. Incubate at RT for 1 minute.
19. Elute by centrifugation at 12,000 x g for 2 min at RT.
20. Store the purified RNA at -80 °C.

Once the RNA is extracted, it is necessary to check its quantity and purity, which can be evaluated by spectrophotometry. In the present thesis RNA was measured by NanoDrop 2000 UV-Vis Spectrophotometer, which provides the concentration of the RNA in ng / μL and its purity is assessed at two different ratios of absorbance. Nucleotides, RNA and DNA absorb at 260 nm. RNA samples are measured at the ratio of absorbance at 260/280 nm to assess their purity. A ratio of 2.0 is generally accepted as pure, if the ratio is appreciably lower, it may indicate the presence of protein, or other contaminants that absorb strongly at or near 280 nm. The ratio 260/230 is used as a secondary measure of nucleic acid purity. The 260/230 values for pure nucleic acid are often higher than the respective 260/280 values. Expected 260/230 values are commonly in the range of 2.0-2.2. If the ratio is appreciably lower than expected, it may indicate the presence of contaminants which absorb at 230 nm, such as ethanol.

6.5.2.3 Reverse transcription polymerase chain reaction (RT-PCR)

RT-PCR is used to clone expressed genes by reverse transcribing the single-stranded RNA of interest into its complementary single-stranded DNA, a process termed reverse transcription. Reverse transcriptase (RT) is the enzyme used to generate complementary DNA (cDNA) from the RNA template. Complementary DNA is synthesized using qScript® cDNA Synthesis Kit following the manufacturer's instructions:

1. Add 1 μg RNA to a mix of 1 μL of qScript RT, 4 μL of qScript® Reaction Mix, and MiliQ water to a final volume of 20 μL
2. Gently vortex the mixture of RNA and reagents and centrifuge for 10 seconds to collect contents.
3. Samples are run in thermal cycle programmed as follows:

   1 cycle: 22°C, 5 min

   1 cycle: 42°C, 30 min

   1 cycle: 85°C, 5 min

   4°C hold

qRT-PCR quantification is then performed as described in section 1.7.1.4, using the primers described in table 12.

6.5.2.4 Housekeeping genes and negative controls

Housekeeping genes are typically constitutive genes that are required for the maintenance of basic cellular function and are expressed in all cells of an organism at relatively constant levels genes such as GAPDH, actin-related protein (ARP), and β-actin. Relative quantitation of the desired gene against an internal standard (housekeeping gene) is particularly useful for gene expression measurements. When performing qPCR is important to run negative controls to be sure there is no DNA contamination. The negative control will contain all the reagents used to perform the qPCR without cDNA to be sure that the primers and the master mix are free of contamination.

6.5.3 **Protein protocols**

6.5.3.1 Protein extraction

Homogenates for western blot analysis were obtained from either cell culture or tissues. To obtain total cellular protein extracts for western blot analysis the protocol is the following:

i. Cellular protein extraction

- Rinse cells in ice-cold PBS
- Scrape from culture plates in RIPA lysis buffer (10 mM Tris-HCl pH 7.2, 150 mM NaCl, 1% Triton X-100, 0.1% SDS, 5 mM EDTA, 1% deoxycholate, phosphatase inhibitors cocktail and protease inhibitors cocktail tablets, and 250U/µl benzonase.
- Homogenize cellular primary homogenates from the plate by passing them through a 25G syringe avoiding the generation of bubbles or foam.
- Centrifuge the homogenates at 10000 x g for 15 min at 4 °C to remove nuclei, cell debris and floating cells.
- Transfer supernatants protein extracts to new tubes and kept at -20 °C.

ii. Liver tissue protein extraction

1. Tissue samples were placed in tubes containing 3 beads and 700 µl of lysis buffer and subjected to 1 round of 30s at maximal speed in the Mini-Beadbeater cell disruptor (Bio Spec Products Inc.).
2. Homogenates were then rotated for 1h at 4°C in an orbital shaker and centrifuged at 13,000 rpm for 15 min at 4 °C.

3. Centrifuge the homogenates at 10000 x g for 15 min at 4 °C to remove nuclei, cell debris and floating cells.

4. Transfer supernatants protein extracts to new tubes and kept at -20 °C.

6.5.3.2 Protein quantification

Once the cellular protein components are obtained, the next step is their quantification. In the present thesis the bicinchoninic acid (BCA) method was used.

The BCA Protein Assay Reagent was purchased at Thermo scientific. The BCA method relies on the Biuret reaction, in which proteins reacting with Cu^{2+} cations liberate Cu^{1+}, in an alkaline medium, which in turn, reacts with the BCA, thereby providing a highly sensitive and selective colorimetric detection because of the generation of a violet compound. Since the amount of the newly generated compound is a function of the protein amount in solution, its absorbance (spectrophotometrically measurable at 562 nm) is proportional to the sample protein concentration.

To perform protein assays accurate standard curves and calibration controls are required. In the present thesis Pierce BSA Protein Assay Standards was used for this purpose. These BSA solutions are protein concentration reference standards for use in BCA. BSA is the universally accepted reference protein for total protein quantitation. The albumin standard is formulated at 2 mg / mL in an ultrapure 0.9% sodium chloride (saline) solution.

Protocol for protein quantification using the BCA method:

1. The volumes of diluted copper-containing buffer are prepared, taking into account the amounts needed for duplicated measures of samples, standard curve and blank

control (200 µL/well). BCA reagent B is diluted 50 times with BCA reagent A, and mixed for 1 min.

2. The standard curve is prepared adding different volumes of the BSA protein and a blank control (0, 2.5, 5, 10, 15, 20 µg per well) in a 96-well plate.

3. The samples (1-5 µL) are added to the 96-well plate and the diluted copper containing buffer is added (200 µL).

4. The 96-well plate is incubated at 37 ºc for 30 min to favor the reaction.

5. Finally, the plate is read at 562 nm using the software Magellan 2 in an ELISA Sunrise Remote/Touch screen (Tecan) lector. The gradient of the straight line is calculated from the BSA standard curve and protein concentrations are determined.

6.5.3.3 Western Blot assay

The western blot is an analytical technique used to detect specific proteins in a given sample. It consists of three parts:

- Polyacrylamide gel electrophoresis to separate denatured proteins by the length of the polypeptide (protein size)

- The proteins are transferred to a membrane (typically nitrocellulose or PVDF)

- The target proteins are detected with specific antibodies

i. Gel preparation and polymerization

The electrophoresis system used in the present thesis was Mini-Protean (BioRad). All the gels were prepared with a depth of 1.5 mm. The glass-plate sandwich of the electrophoresis apparatus is prepared according to manufacturer's instructions using two clean glass plates and 1.5 mm spacer and is locked to the casting stand. The separating gel (7.5 mL) is prepared using 6, 10 or 12,5 % of acrylamide, Tris-Base 0.375 M, pH 8.8, SDS 0.1%, ammonium persulfate (APS) 0.05 % and TEMED 2.2 Mm and is added among the

glass-plate sandwich. Before polymerization acrylamide is a neurotoxic agent and is compulsory the use of gloves. APS and TEMED are added just before polymerization because they are the initiators and catalyst of the polymerization reaction, respectively. Once the separation gel is added in the glass-plate sandwich, isopropanol (100 μL) is added to provide a barrier to oxygen that inhibits polymerization, to avoid SDS bubbles, and to achieve a straight edge of the gel. The gel is allowed to polymerize at room temperature. Meanwhile, the stacking gel is prepared using 3.3 % of acrylamide, Tris-HCl 0.125 M, pH 6.8, SDS 0.1 %, APS 0.1 % and TEMED 6.6 mM. Then, isopropanol is eliminated from the top of the separating gel, and 2.5 mL of the stacking gel are added. A teflon comb of 1.5 mm is inserted into the layer of the stacking gel to form the wells and polymerization is allowed at room temperature. Maximum attention is required to not trap air bubbles into the comb, which will lead to distortion in the protein bands during separation.

ii. Samples preparation

Protein samples are mixed with Loading Sample Buffer (LSB) to ensure that the proteins will be properly denatured and heated for 5 min at 95 oc. The LSB 4X is composed by Tris-HCl 0.4 M, pH 6.8, glycerol 69.6 %, SDS 8 % (p/v), bromophenol blue 0.05 mg / mL (allows sample visualization), and DTT 100 mM. DTT is used to break disulphide bridges among proteins. Once the samples are boiled, the samples are centrifuged at maximum speed. Usually 10-50 μg of protein are loaded in each well.

iii. Gel electrophoresis

The polymerized gel sandwich is placed in the electrophoresis system and the buffer chamber is filled with electrophoresis buffer, which contains Tris-Base 25 mM, glycine 0.19 M and SDS 0.1 %. The Teflon® comb is carefully removed without tearing the edges of the polyacrylamide gels. If well walls are not upright, they can be manipulated with a micropipette (10 μL). After the comb is removed, the samples and the ladder are loaded into the wells. The ladder use is the pre-stained SDS-PAGE standards Broad Range (BioRad). Empty wells are also loaded with loading buffer to run gels straighter, and samples are always loaded in the central wells. Finally, electrophoresis buffer is added to completely cover the platinum electrode within the upper chamber, and the electrophoresis chamber is closed and connected to the power supply. The 1.5 mm electrophoresis gel is run at a fix 25 mA/gel until the bromophenol blue dye reaches the bottom of the separating gel.

iv. Protein transfer to PVDF membranes

In order to make the proteins accessible to antibody detection they are moved from within the gel onto a membrane made of nitrocellulose or polyvinylidene difluoride (PVDF). In the present thesis PVDF Immobilon™ membranes (Millipore) were used since they have very high protein binding capacities, with good handling characteristics, and in addition, they are highly chemically inert, and effective for low-background staining. The method for transferring the proteins is called electroblotting and uses an electric current to pull proteins from the gel into the PVDF according to the charge of the protein. The proteins move from within the gel onto the membrane while maintaining the organization they had within the gel. The transfer equipment used in the present thesis was Mini Protean TransBlot Cell (BioRad), which employs a transfer tank apparatus filled with transfer buffer, in which the gel/membrane sandwich is placed. The transfer buffer contains Tris-Base 25 mM, Glycine 0.19 M pH 8.3, and 20% of methanol. Once electrophoresis is finished electrophoresis buffer is discarded and the glass sandwich is opened to remove the gel and the following protocol is performed:

1. The gel is equilibrated in transfer buffer

2. The PVDF transfer membrane (6 x 9 cm) and the Whatman paper (7 x 9 cm) are cut. The PVDF membrane is marked at the bottom right side with a pen to know the orientation later.

3. The PVDF membrane is activated in 100% MeOH for 1 min.

4. Set up the sandwich from black (-) to red/white (+) side in transfer buffer with the following order: sponge, Whatman paper, gel (the gel is oriented that the order of the samples is well-known), the activated membrane (the written side of the membrane is collocated towards the gel), Whatman paper and sponge. All the process is performed in a tray full of transfer buffer to equilibrate all the material. Bubbles must be avoided for a correct transfer, since air bubbles prevent the transfer of proteins.

5. The sandwich is inserted in the transfer cassette into the tank with the gel on the cathode (black) side and the membrane on the anode (red) side. Proteins

proceeding from an SDS-Page gel have a negative charge and will migrate towards the anode.

6. The transfer container is filled with transfer buffer and a block of ice is collocated inside

   the transfer container next to the sandwich to prevent overheating caused by the high current rates. The system is connected to the power supply and the transfer is performed at a constant current of 250 mA for 90 min.

7. Once the transfer was done, the power supply is disconnected and the gel and the PVDF membrane are removed from the transfer system. The membrane will be used for immunodetection, and the gel can be stained with Coomassie Brilliant Blue dye to check the uniformity and overall effectiveness of the protein transfer.

v. Immunodetection of the target protein

Once the transferred proteins are bound to the PVDF membrane surface, they are available to react with immunodetection reagents. This process consists of 4 steps: blocking, primary and secondary antibody exposure, and detection:

1. The non-specific binding sites should be blocked with a rich protein solution to avoid unspecific binding of the primary antibody to the membrane. In the present thesis the PVDF membranes were immersed in blocking solution (PBS + 0.1% Tween-20 with 5 % (p/v) of skimmed milk) for 1 h at room temperature and incubated with agitation on a rocking platform.

2. The membrane is incubated with the primary (specific) antibody solution (6 mL) for 16h at 4oc with agitation. All the primary antibodies used in the thesis were diluted in blocking solution, and their concentration was based on the information provided by the supplier. After the incubation, the membrane is washed with Tween 20 0.1 % (v/v) in PBS (10 min, 3 times) at room temperature with agitation. The washes are performed to eliminate the primary antibody excess.

3. Once formed, the antibody-antigen complexes are recognized by secondary antibodies (anti- IgG) that are labeled with probes allowing their detection. All the secondary antibodies used in this thesis were labeled with Horse Radish

Peroxidase (pHRP) and were purchased from Jackson. The secondary antibody solution is prepared with PBS-Tween 20 0.1 % and skimmed milk 1% (p/v). The secondary antibodies that recognize rabbit IgG (antirabbit) and mouse IgG (anti-mouse) were diluted in 1/10,000 and 1/2500, respectively. The membrane was incubated with the secondary antibody solution for 1 h at room temperature with agitation. Then, the membrane is washed with Tween 20 0.1 % (v/v) in PBS (10 min, 3 times) at room temperature with agitation.

4. Secondary antibodies after exposure to chromogenic or luminescent substrates, serve to visualize the protein location. HRP signal is developed with Enhanced ChemioLuminiscence reagents (ECL). The two reagents from the kit are mixed (1:1) and the membrane is incubated with the mix for 3 min. The membrane is collocated between a plastic folder in a film cassette (Wolf), drained removing the bubbles with paper tissue, and finally exposed to film in the dark room at different exposition times. The film can be exposed for a few seconds to several hours depending on the protein amounts and the primary antibody potency. The films used in the present thesis were (Amersham Biosciences) and were developed in a Hyper Processor Model AM4 (Amersham Pharmacia Biotech). The membrane can be used to detect another protein and stored in PBS at 4 ºC or discarded.

Once the film has been developed a quantitative protein analysis can be performed by densitometry. α-tubulin, β-actin and porin were used to determine the proportion of protein levels referred to total mitochondrial and total mass, respectively. In the present thesis different antibodies were used (Table 6).

6.5.3.4 Stripping

Once a membrane is blotted with specific antibodies, further incubations can be performed. Several factors determine whether or not it is necessary to eliminate the antibodies primarily bound to the membrane before the second incubation. It depends on the similarity of the molecular weight of the target proteins and the secondary antibody recognition. Thus, if the antibodies used recognize protein sufficiently separated, or if the secondary antibody is different (anti-mouse and anti-rabbit o vice versa), blotted membranes can be directly used, since overlapping events should not occur. In contrast, if either the

molecular range or the secondary antibody producer is similar, membranes should be properly treated to detach antibodies. The stripping allows the clearance of antibodies attached to a membrane, leaving the transferred protein amounts almost intact. The stripping consists in washings of boiling H_2O (90º C) (3 x 10 min). Once the stripping is performed, the Procedure for immunodetection of the target protein is followed (Section 7.9.3.5).

6.5.3.5 Densitometry analysis

Densitometry is the quantitative measurement of optical density in light-sensitive materials, such as photographic paper or photographic film, due to exposure to light. Optical density is a result of the darkness of a developed picture and in this thesis it has been used to quantify the levels of the target protein in the film obtained from the western blot. The films are scanned (HP photosmart) and the software used to quantify the protein levels is Image J (Fiji).

6.6 Transmission electron microscopy (TEM)

To study mitochondria and cellular ultrastructure, transmission electron microscopy was performed. In this thesis, only the pre-fixation and fixation by perfusion of liver tissue/cells steps were performed. Steps of post-fixation, dehydration and embedding of the tissue were performed by Unitat de Crio-Microscòpica in the Centres Cientifics i Tecnològics de la Universitat de Barcelona (CCiTUB).

i. Protocol of perfusion fixation of liver tissue

1. Anesthetize the animals and allow 10 to 15 min for anesthesia to occur, indicated by the loss of sensory/reflex response;

2. Once anesthetized, mice are trans-cardiac perfused with PBS containing 2.5% glutaraldehyde and 2% paraformaldehyde (PFA);

3. After 5 min of continuous perfusion, liver can be harvested and appropriately dissected to obtain fragments;

4. Let the tissue fragments immersed in fixative O/N at 4 ºC to complete the fixation Procedure;

5. The next day, dispose the fixative solution and rinse the fragment samples with PBS for 10 min with occasional shaking (4 times);

ii. Protocol of fixation of cells

1. Cell culture media is removed and discarded from the culture plate;

2. Cells are washed using PBS (approximately 5 mL per 10 cm cell culture dish). The wash solution is added to the side of the cell plate gently, to avoid cell layer disturbing.

3. Fixative solution is added to the cells with PBS containing 2.5% glutaraldehyde and let it for 30 min, RT (2x);

4. Harvest cells by gently scrapping cells;

5. Centrifuge at 2500 rpm for 10 min, 4 ºC;

6. Remove the fixative solution and resuspend the pellet with PBS and centrifuge for 10 min, 4 ºC (4 times).

6.7 Statistics

Reads were aligned to the mm10 genome using STAR 2.3.0e with default parameters. Counts per genomic feature were computed with the R package Rsubread, function featureCounts. Differential expression between conditions was performed using the DESeq2 R package. The regularized log transformed matrix was used for boxplots and heatmaps. The log2FC information was considered to rank all genes in the genome and Gene set enrichment analysis (GSEA) was performed using the Broad Institute's implementation on public collections. Statistics analysis were performed by the Biostatistics & Bioinformatics facility at the IRB Barcelona.

7

Resumen en Castellano

7 Resumen en Castellano

7.1 Sumario

OPA1 es una proteína relacionada con la dinamina que es responsable de la fusión de la membrana mitocondrial interna y esencial para controlar la morfología de las crestas mitocondriales, afectando directamente la eficiencia de OxPhos y la estabilidad del DNA mitocondrial. En este estudio, hemos explorado los efectos de la eliminación hepática de OPA1 sobre la función mitocondrial y el metabolismo. Hemos demostrado que la ablación de OPA1 en el hígado produce una disfunción mitocondrial caracterizada por alteraciones en la estructura de las crestas mitocondriales, concomitante con una capacidad respiratoria reducida y menor número de copias de DNA miocondrial, y perturbación en la proteostasis mitocondrial. La disfunción mitocondrial causada por la ablación de OPA1 en el hígado desencadena la activación de una respuesta al estrés mitocondrial, incluyendo la respuesta a las proteínas mal plegadas de la mitocondria, que probablemente es mediada por el factor de transcripción ATF5. Curiosamente, hemos observado que la deficiencia de OPA1 en el hígado causa una mejor tolerancia a la glucosa y protege contra la obesidad y resistencia a la insulina inducida por la dieta, en paralelo con un aumento de los niveles de FGF21 circulante, un factor involucrado en la modulación metabólica.

Con este estudio proponemos que los efectos sistémicos protectores asociados a la ablación de OPA1 se deben a la acción de FGF21 que probablemente es mediada por la respuesta al estrés mitocondrial asociada a la pérdida de función de OPA1 a través de la activación de ATF5.

7.2 Introducción

Las mitocondrias juegan un papel crítico en el mantenimiento de la homeostasis energética del organismo para una multitud de procesos y supervivencia celular. La presencia de mitocondrias saludables es, por lo tanto, esencial para la generación adecuada de energía y la homeostasis celular. La función óptima y la adaptabilidad funcional de las mitocondrias dependen de la acción concertada de un sistema de control de calidad de proteínas

estrechamente relacionado con un proceso dinámico coordinado de fusión y fisión que actúa para auditar y mantener la homeostasis de los orgánulos, permitiendo que las mitocondrias adapten su morfología, satisfagan las demandas metabólicas, respondan a diferentes niveles de daño y, en última instancia, garanticen la eliminación de las mitocondrias severamente dañadas (Baker et al. 2011).

La dinámica de las mitocondrias está regulada por una gran familia de GTPasas relacionadas con la dinamina en la membrana mitocondrial externa (OMM) y la membrana mitocondrial interna (IMM) de las mitocondrias (Liesa et al. 2009). Por un lado, la fisión mitocondrial está regulada por la proteína 1 relacionada con la dinamina (DRP1) y por sus adaptadores en la OMM, incluida la proteína de fisión mitocondrial 1 (Fis1), el factor de fisión mitocondrial (MFF) y las proteínas dinámicas mitocondriales de 49 (MiD49) y 51kDa (MiD51) (Palmer et al.2011; Otera et al.2010; Loson et al.2013). Por otro lado, la fusión mitocondrial está regulada por mitofusina 1 (MFN1) y mitofusina 2 (MFN2) en el OMM (Chen et al. 2003) y por *Optic Atrophy 1* (OPA1) en la IM (Cipolat et al., 2004).

Independientemente de su papel en la fusión de la IMM, OPA1 controla la morfología de las crestas mitocondriales. Al remodelar la estructura de las crestas, OPA1 no solo determina la redistribución del citocromo c dentro de las células, lo que protege las mitocondrias de los estímulos apoptóticos (Frezza et al. 2006) sino que también asegura la organización funcional de los supercomplejos mitocondriales adaptados para la producción eficiente de ATP y mantiene el DNA mitocondrial (mtDNA) intacto (Cogliati et al.2013; Civiletto et al.2015; Varanita et al.2015).

Al igual que el retículo endoplásmico (RE), las mitocondrias poseen una maquinaria de control de calidad de proteínas que proporciona un control estricto del plegamiento y degradación de proteínas, preservando la función de las proteínas mitocondriales. Por lo tanto, cuando se perturba la proteostasis mitocondrial, las mitocondrias activan una respuesta de estrés núcleo-mitocondrial, comúnmente llamada UPRmt, en un intento de aliviar los defectos de proteostasis (Haynes & Ron 2010). Se ha descrito que los defectos en la traducción mitocondrial y las alteraciones en el mtDNA perturban la proteostasis mitocondrial, ya que ambas condiciones conducen a un desequilibrio entre las proteínas mitocondriales codificadas por el mtDNA o el genoma nuclear, posiblemente provocando la acumulación de subunidades de los complejos de la fosforilación oxidativa (OxPhos) (Moehle et al.2019). Además, defectos en OxPhos conducen a un desacoplamiento o

disipación del potencial de membrana de la membrana interna, lo que inhibe directamente la translocación de proteínas a la mitocondria, que también se ha relacionado con la activación del UPRmt (Naresh & Haynes 2019).

En las células de mamíferos, la activación de UPRmt está mediada por múltiples factores de transcripción tales como ATF4, CHOP y ATF5 tras la fosforilación de eIF2a. La activación de UPRmt da como resultado la inducción de un programa transcripcional que incluye la acción de las chaperonas mitocondriales Hsp60, Hsp10 y mtHsp70, que promueve el plegamiento de proteínas y evita la formación de agregados y elimina la acumulación de proteínas dañadas o mal plegadas a través de la actividad de proteasas mitocondriales, tales como ClpP, LONP1 y AFG3L2 (Melber y Haynes 2018).

La activación de ATF4, CHOP y ATF5 tras la fosforilación de eIF2a está asociada a la respuesta integrada al estrés (ISR), que se ha caracterizado mejor como una respuesta al estrés de ER. El inicio de ISR está mediado por cuatro quinasas que responden a factores de estrés específicos y fosforilan eIF2α: proteína quinasa dependiente de RNA (PKR), quinasa ER similar a PKR (PERK), quinasa eIF2α regulada por hemo (HRI) y control general no represible 2 (GCN2). PKR, PERK y HRI responden específicamente (1) a la presencia de RNA de doble cadena en el citosol, (2) a las perturbaciones en el ER, y (3) a la disponibilidad de hemo, respectivamente, mientras que GCN2 se activa por numerosas tensiones, que incluyen la privación de aminoácidos o glucosa, y la disfunción mitocondrial (Pakos-Zebrucka et al. al.2016). En última instancia, la fosforilación de eIF2α causa la atenuación de la síntesis global de proteínas al tiempo que promueve la traducción selectiva de los factores de transcripción CHOP, ATF4 y ATF5, lo que sugiere que UPRmt está íntimamente asociado con ISR (Melber y Haynes 2018). Sin embargo, aún se desconoce cómo la disfunción mitocondrial está directamente relacionada con la inducción de ATF4 / CHOP y ATF5.

Recientemente, nuestro grupo ha demostrado que tras la ablación específica de OPA1 en el músculo esquelético, los niveles del gen *fgf21* aumentan en el músculo juntamente con los niveles circulantes de FGF21, posiblemente bajo la regulación por ATF4 ya que se detectó la activación de varias dianas de ATF4 en el músculo, lo que sugiere que FGF21 está actuando como una hormona del estrés (Rodríguez-Nuevo et al.2018). Por otra parte, Pereira et al. (2017) ha demostrado que la secreción de FGF21 asociada a la deficiencia de OPA1 en el músculo previene la obesidad y la resistencia a la insulina.

FGF21 se expresa principalmente en el hígado durante el ayuno y tiene un papel fundamental en la regulación del metabolismo energético sistémico, al aumentar la absorción de glucosa en los tejidos, ya que aumenta la sensibilidad a la insulina, y la oxidación de ácidos grasos libres en paralelo con la inhibición de la lipogénesis en el hígado. A pesar de que la activación de UPRer, inducida por el estrés en el retículo endoplásmico, a menudo se conoce como un promotor primario de la inducción de FGF21 a través de la vía de PERK-eIF2a-ATF4, también se ha demostrado que FGF21 se induce en modelos caracterizados por una mayor acumulación de deleciones de mtDNA, defectos en OxPhos, mitofagia alterada y fisión mitocondrial aberrante (Tezze et al.2019). Sin embargo, los mecanismos moleculares por los cuales el estrés mitocondrial induce FGF21 aún deben aclararse.

7.3 Objetivos

En base a las observaciones anteriores, el objetivo de la presente tesis doctoral es evaluar la respuesta mitocondrial a la pérdida de función hepática OPA1 y caracterizar el impacto metabólico asociado en un modelo de ratón knockout específico para hígado. Con este fin, se han realizado los siguientes estudios principales:

1. Estudio del efecto inducido por el agotamiento hepático de OPA1 en la función mitocondrial;

2. Caracterización de los efectos metabólicos de todo el cuerpo inducidos por la ablación de OPA1 en el hígado;

3. Identificación de jugadores clave en la respuesta metabólica adaptativa asociada a la deficiencia de OPA1 en el hígado.

7.4 Resultados y Discussión

Evaluación del impacto de la pérdida de función de OPA1 en el hígado

La generación del modelo se realizó cruzando ratones homocigotos Opa1loxP / loxP (Rodríguez-Nuevo et al.2018) con una cepa de ratón que expresa Cre recombinasa bajo el control del promotor de albúmina (Alb-Cre). Cuando el gen Opa1 se interrumpió en el hígado usando el sistema Alb-Cre / loxP (Figura 49.A), los niveles de OPA1 fueran prácticamente inexistentes en el hígado (Figura 49.B-C), pero no se veían afectados en otros tejidos (Figura 49.C). Estos animales demostraron ser fértiles, mostraron una esperanza de vida normal y la descendencia respetó la proporción mendeliana.

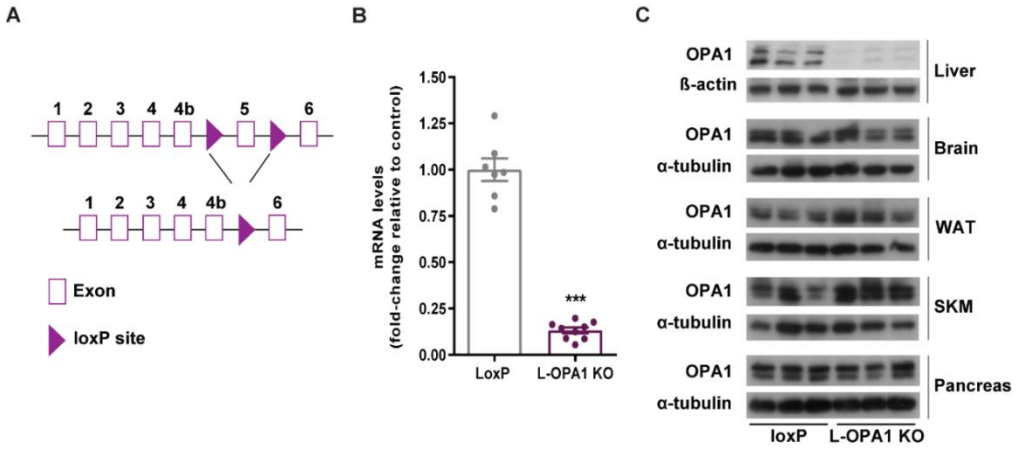

Figura 49. Generación del modelo de ratón knockout OPA1 específico de hígado. (A) Estructura genómica parcial del gen Opa1 que muestra la escisión del exón 5, eliminando así todas las isoformas de la proteína OPA1. (B) Niveles de mRNA de Opa1 en el hígado de ratones loxP y L-OPA1 KO (n = 7-8). (C) Western blot representativo de los niveles de proteína OPA1 en el hígado, el cerebro, el tejido adiposo blanco (WAT), el músculo esquelético (SKM) y los homogeneizados de tejido pancreático de control loxP (loxP, Cre negativo Opa1loxP / loxP) y ratones knockout OPA1 específico de hígado (L-OPA1 KO) (n = 7-8). Los datos representan la media ± SEM. *** p <0,001 frente a ratones control loxP.

Tras la generación exitosa del modelo de ratón knockout OPA1 específico de hígado (L-OPA1 KO), evaluamos la función mitocondrial, exploramos las alteraciones metabólicas causadas por la pérdida de función de OPA1 en el hígado y buscamos los posibles efectores-clave y el mecanismo de la respuesta metabólica desencadenada.

Como OPA1 participa en el mantenimiento de la estructura de las crestas y, por lo tanto, afecta directamente la capacidad oxidativa mitocondrial, analizamos la estructura

mitocondrial mediante microscopía electrónica en hígados de L-OPA1 KO y ratones control loxP, de 8 semanas de edad. Como se esperaba, las mitocondrias en L-OPA1 KO revelaron crestas desorganizadas (Figura 50).

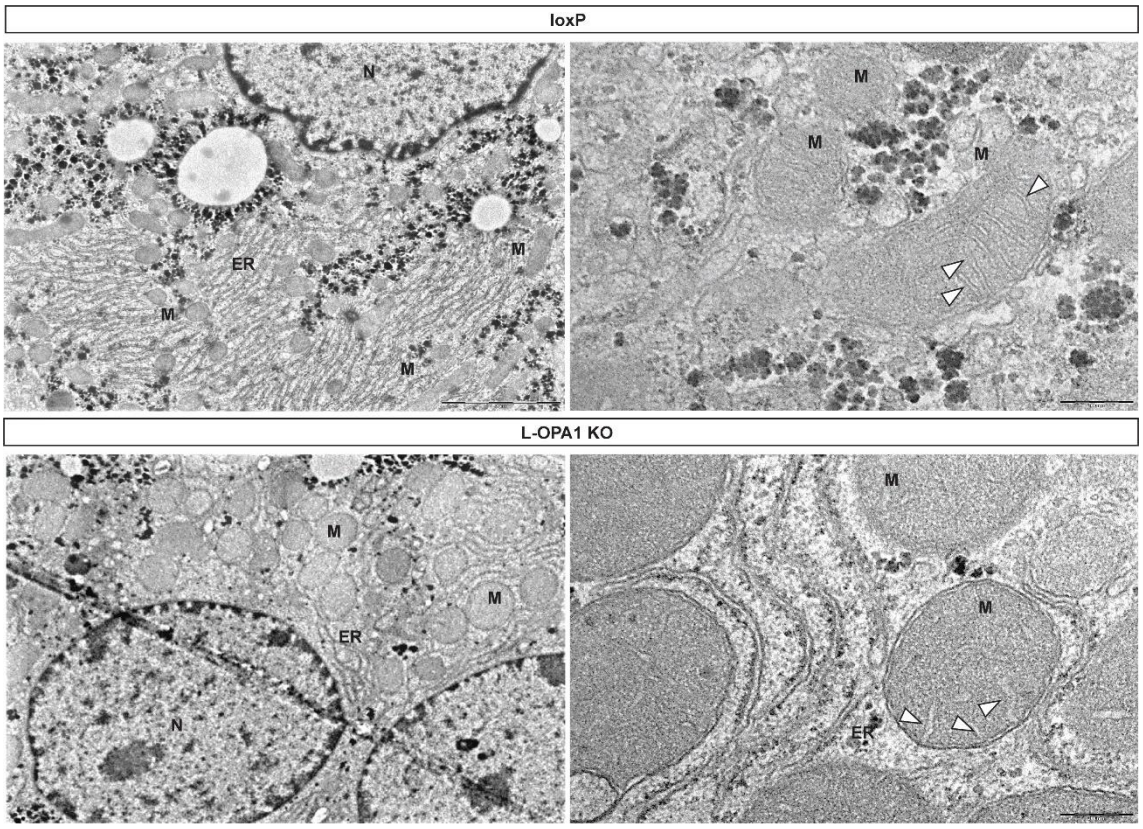

Figura 50. La morfología de las crestas mitocondriales está perturbada en ratones L-OPA1 KO. Representación de micrografías electrónicas de hígados de ratones control loxP y L-OPA1 KO. (n = 3) (ER) Retículo endoplasmático. (M) Mitocondria. (N) Núcleos. Cretas mitocondriales indicadas por las flechas en la figura, en ambos paneles. Barra de escala 2 μm.

Para evaluar más a fondo la capacidad oxidativa mitocondrial, a las 8 semanas de edad realizamos un análisis de respirometría de alta resolución en homogeneizados totales de hígado. La respiración del estado 4 (I) se midió después de la adición de glutamato (2 mmol / L) y malato (10 mmol / L), luego se añadió ADP (250 μmol / L) para medir el estado 3 (I) de la respiración. Posteriormente, la respiración mitocondrial fue estimulada con succinato (10 mmol / L) para medir el estado respiratorio 3 (I + II). Los hígados de ratones L-OPA1 KO mostraron una menor capacidad oxidativa mitocondrial caracterizada por una actividad del estado 4 (I) (Figura 51).

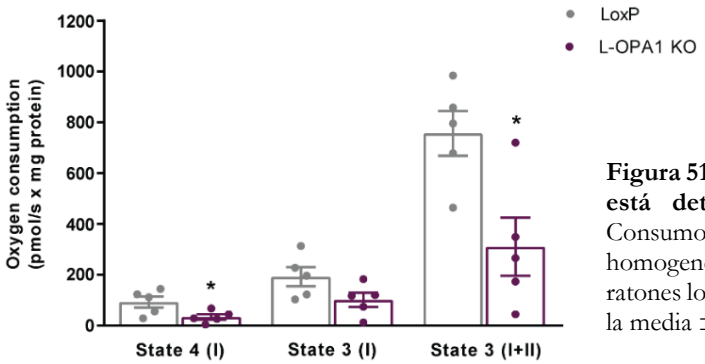

Figura 51. La respiración mitocondrial hepática está deteriorada en ratones L-OPA1 KO. Consumo de oxígeno analizado en homogeneizados totales de hígado aislados de ratones loxP o KO (n = 4-5). Los datos representan la media ± SEM. * p <0.05 vs. loxP.

Estas diferencias nos llevaron a analizar más a fondo la expresión de complejos de subunidades mitocondriales que reflejan una disminución sustancial en los complejos nucleares codificados con el genoma I, II, III y V, y la subunidad del complejo IV codificada con mtDNA (Figura 52.A-B)

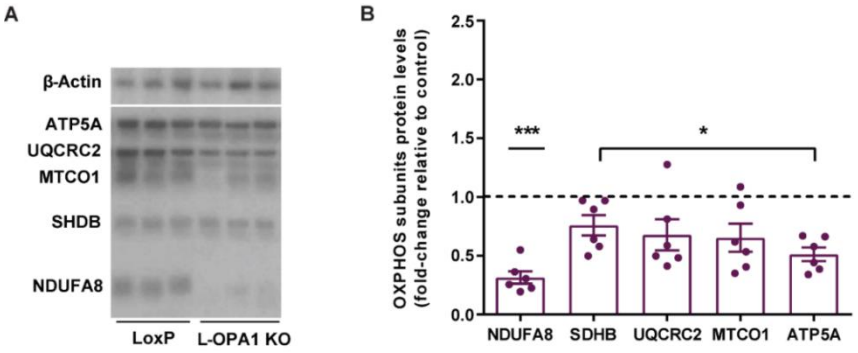

Figura 52. La expresión de las subunidades OxPhos se reduce en L-OPA1 KO. (A) Western blot representativo de la expresión de subunidades OxPhos mitocondriales relativas del hígado de loxP y L-OPA1 KO. (n = 6). (B) Niveles de expresión de la subunidad NDUFA8 del complejo I, subunidad SDHB del complejo II, subunidad UQCRC2 del complejo III, subunidad MTCO1 del complejo IV y subunidad ATP5A del complejo V. Los datos representan la media ± SEM. * p <0.05, *** p <0.001 vs loxP

Sin embargo, mientras que la expresión de las subunidades OxPhos se redujo, el análisis de proteínas mitocondriales en los homogenizados hepáticos totales reflejó un aumento en la porina mitocondrial y el nivel de expresión de TIMM44 que muestra que los ratones L-OPA1 KO mostraron un contenido mitocondrial más alto (Figura 53.A-B).

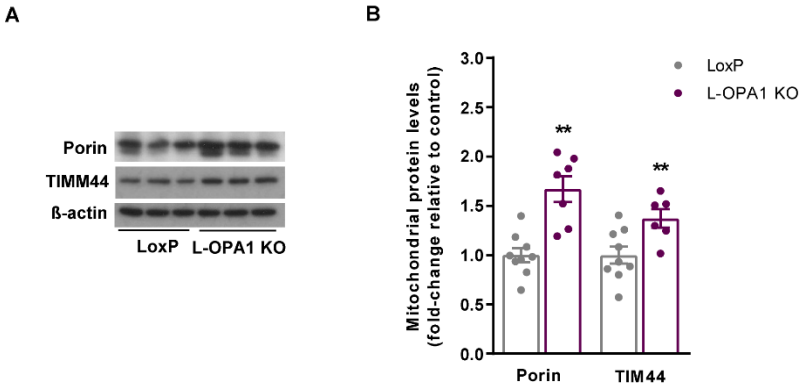

Figura 53. El agotamiento hepático de OPA1 aumenta la abundancia de algunas proteínas mitocondriales. (A) Transferencia western representativa de los niveles de proteína mitocondrial en homogeneizados de hígado de ratones de 8 semanas de edad (B) Niveles de expresión de proteínas de Porin y TIMM44 (n = 6-7). Los datos representan la media ± SEM. ** p <0.01 vs. loxP

Según el vínculo entre la pérdida de función de OPA1 y la inestabilidad del mtDNA, evaluamos el contenido de mtDNA y los niveles de proteína del factor de transcripción mitocondrial A (TFAM) en el hígado y, de hecho, la deficiencia de OPA1 en el hígado condujo a una reducción de menos del 55% en la cuantificación de número de copias de mtDNA (Figure 54.A), medido por la amplificación de una región única de mtDNA en la posición 1212 a 1352, en paralelo con una reducción del 32,4% de los niveles de proteína TFAM (Figure 54.B-C).

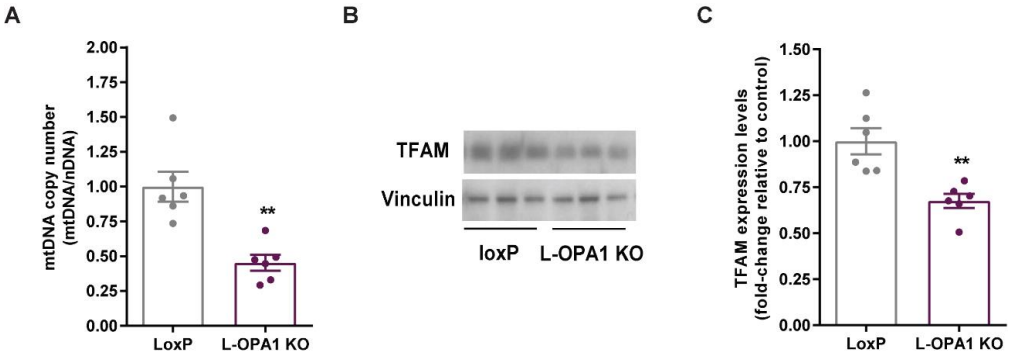

Figura 54. El agotamiento de OPA1 reduce el contenido de mtDNA y la abundancia de TFAM en el hígado. (A) Niveles de mtDNA relativos al DNA nuclear. (B) Blot representativo de los niveles de la proteína TFAM. (C) Níveles de expresión de la proteína TFAM en homogeneizados de tejido hepático de ratones de 8 semanas de edad, n = 6. Los datos representan la media ± SEM. ** p <0.01 vs. ratones control loxP.

Caracterización del impacto metabólico asociado a la ablación de OPA1 en el hígado.

Para determinar si la disfunción mitocondrial asociada con la pérdida de la función de OPA1 en el hígado afecta a la homeostasis de glucosa en ratones L-OPA1 KO, llevamos a cabo una serie de estudios metabólicos en dieta normal y dieta rica en grasas (HFD), tales como el control semanal del peso corporal, test de tolerancia a la glucosa (GTT) y test de tolerancia a la tolerancia a la insulina (ITT), ingesta de alimentos y calorimetría indirecta. Como a las 8 semanas de edad, L-OPA1 KO ya demostraba una disfunción mitocondrial constante, se eligió esta edad para todos los análisis metabólicos posteriores, caso contrario se indicará.

El peso corporal se midió cada 2 semanas hasta que los animales alcanzaron las 24 semanas de edad. El peso corporal de L-OPA1 KO era indistinguible del de los ratones loxP, así como la distribución de masa magra y grasa (Figura 55. A-B). La ingesta de alimentos se evaluó en animales estabulados individualmente durante 7 días y no se observaron diferencias entre los ratones control loxP y L-OPA1 KO (Figura 55.C).

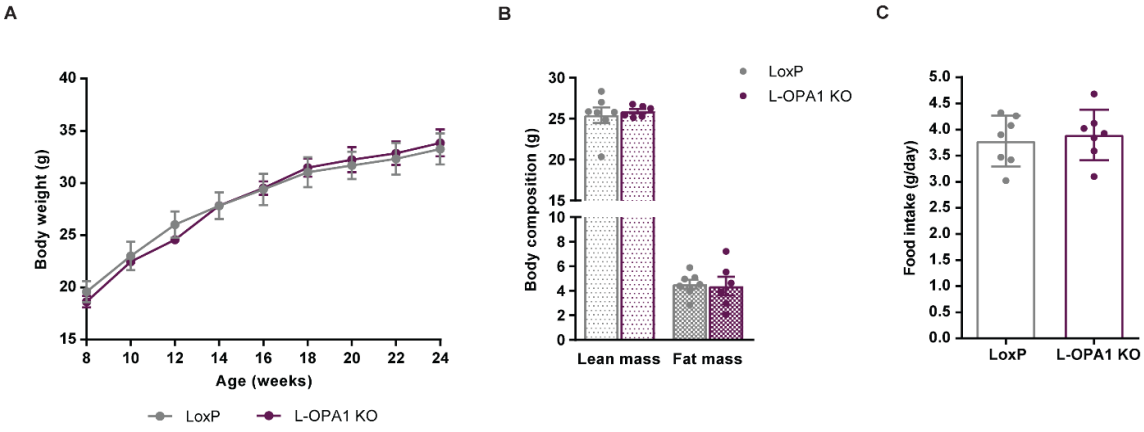

Figura 55. Los ratones L-OPA1 KO no presentan cambios en el peso corporal o en la ingesta de alimentos. (A) Mediciones de peso corporal de ratones entre 8 y 24 semanas de edad (n = 7-6). (B) Composición corporal medida por EchoMRI a las 16 semanas de edad. (C) Consumo de alimentos como gramos de ingesta por día (7 días consecutivos; n = 7). Los datos representan la media ± SEM.

La GTT evalúa la eliminación de una carga de glucosa administrada mediante inyección intraperitoneal, brindándonos también información sobre la secreción de insulina. Después de un ayuno de 16 h, se administró 1U / kg de glucosa y se midió la glucosa en la

sangre durante un tiempo de 2 horas. Sorprendentemente, a pesar de no haber cambios en el peso corporal o diferencias en la ingesta de alimentos, los ratones L-OPA1 KO mostraron una mejor tolerancia a la glucosa que se producida con menores niveles plasmáticos de insulina en comparación con su control loxP. Estos datos demostraron que L-OPA1 KO exhibe una mejor capacidad para manejar la glucosa en presencia de menos insulina circulante (Figura 56.A-B).

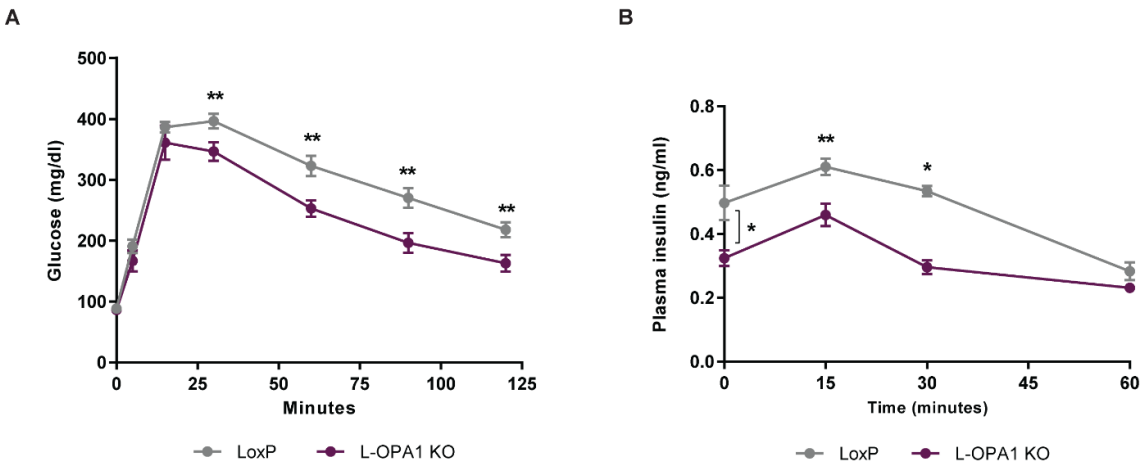

Figura 56. Los ratones L-OPA1 KO muestran un mejor manejo de la glucosa en un contexto de menor insulina circulante. (A) Ratones macho de 8 semanas de edad en ayunas de 16 h sometidos a un test de tolerancia a la glucosa (2 g / kg; n = 6). (B) Niveles de insulina en plasma durante la GTT (n = 6). Los datos representan la media ± SEM. * p <0.05, ** p <0.01 vs. ratones control loxP.

Debido a que los ratones L-OPA1 KO mostraron una mayor tolerancia a la glucosa caracterizada por menores niveles de insulina en plasma, decidimos evaluar la capacidad de respuesta a la insulina realizando un test de intolerancia a la insulina (ITT). La ITT consiste en controlar la glucosa durante 90 minutos tras la administración de una dosis máxima de insulina después de un ayuno de 4 horas, y es indicativa de la acción de la insulina en todo el cuerpo. Los resultados de ITT revelaron que los ratones L-OPA1 KO eran más hipoglucémicos en comparación con los controles, lo que sugiere una mayor sensibilidad a la insulina (Figura 57.A-B).

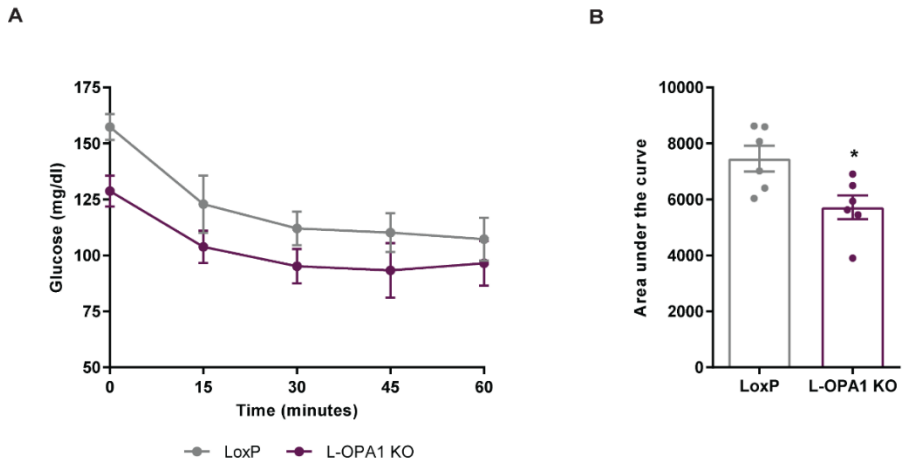

Figura 57. Los ratones L-OPA1 KO exhiben una mayor respuesta a la insulina. (A) Ratones macho de 10 semanas de edad sometidos a un ayuno de 4h fueron estimulados con insulina y sometidos a un test de tolerancia a la insulina (ITT). (B) Área bajo la curva. 0.5U / kg; n = 6. Los datos representan la media ± SEM. * p <0.05 vs ratones control loxP.

A continuación, expusimos a los ratones L-OPA1 KO y control loxP a una sobrecarga crónica de lípidos para evaluar si los ratones L-OPA1 KO mantienen su mejor manejo de glucosa en presencia de una sobrecarga lipídica. Con este fin, pusimos a los animales en una dieta con alto contenido de grasa (60% kcal% de grasa), que fue introducida por primera vez a las 6 semanas de edad y durante 16 semanas. Someter a los animales a 16 semanas de dieta alta en grasas es el procedimiento estándar para observar el fenotipo completo de la obesidad inducida por la dieta (Wang y Liao 2012). El peso corporal se midió cada dos semanas hasta el punto final del experimento y, sorprendentemente, los ratones L-OPA1 KO fueron significativamente más delgados en comparación con el control, lo que indica que los ratones L-OPA1 KO están protegidos contra la obesidad inducida por la dieta (Figura 58.A-B).

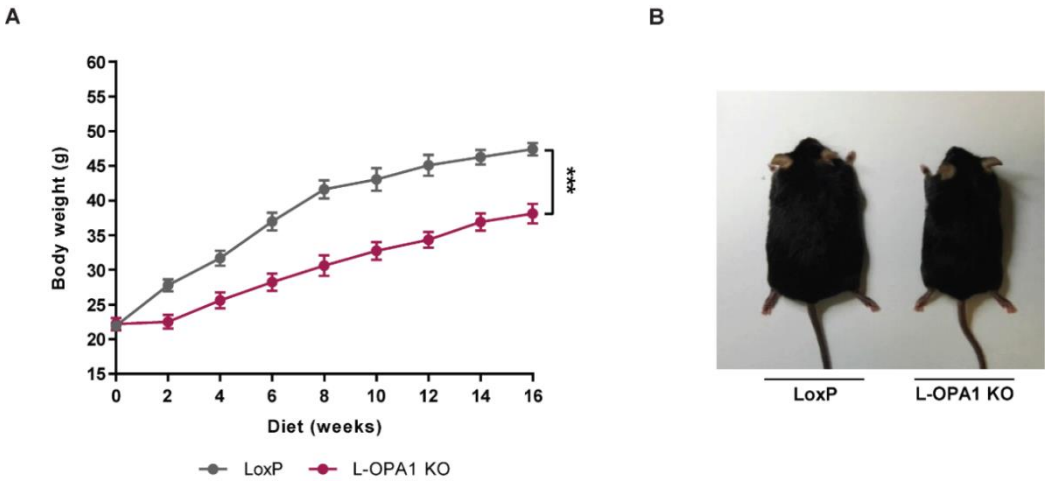

Figura 58. Los ratones L-OPA1 KO están protegidos contra la obesidad inducida por la dieta. (A) Mediciones de peso corporal de ratones cada 2 semanas durante 16 semanas de dieta rica en grasa (HFD; n = 6-8). (B) Imagen del control loxP y L-OPA1 KO a las 16 semanas de dieta. *** p <0,001 frente a ratones control loxP.

Además, L-OPA1 KO reveló una reducción del 50% en la composición de masa grasa en comparación con el control loxP que corrobora con el menor peso corporal observado, a pesar de que no se observaron diferencias en la ingesta de alimentos entre los ratones control loxP y el L-OPA1 KO (Figura 59.A-B).

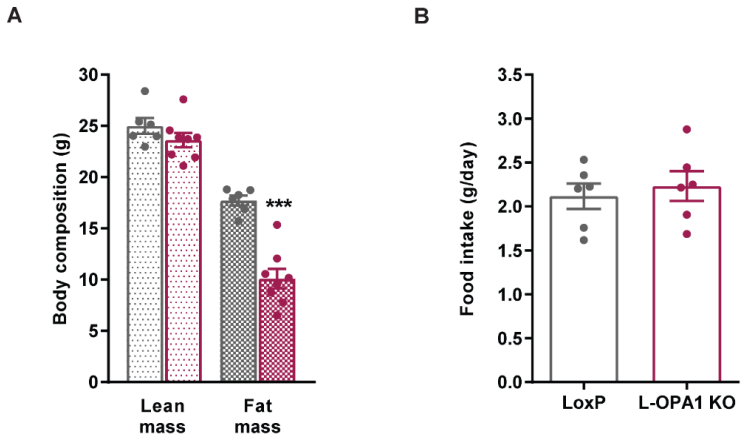

Figura 59. El contenido de masa de grasa es menor en L-OPA1 KO a pesar de no haber diferencias en la ingesta de alimentos. (A) Composición corporal medida por EchoMRI a las 16 semanas de dieta. (B) Consumo de alimentos como gramos de ingesta por día (7 días consecutivos; n = 7). Los datos representan la media ± SEM. *** p <0,001 frente a ratones control loxP.

Como se observaron diferencias consistentes al inicio de la dieta, (8 semanas de dieta), los animales fueron sometidos a una GTT, lo que reveló que el mejor manejo de glucosa en ratones L-OPA1 KO se exacerbó en una dieta rica en grasas. De manera similar a la dieta normal, los niveles de insulina de los ratones L-OPA1 KO en una dieta rica en grasas fueron más bajos en comparación con el control loxP (Figura 60.A-B).

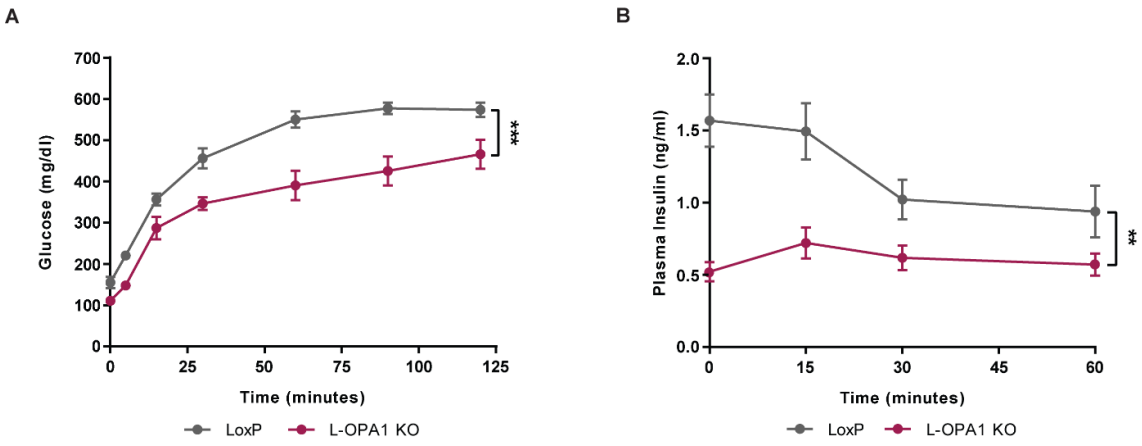

Figura 60. Los ratones L-OPA1 KO mantienen una mayor tolerancia a la glucosa en HFD. (A) A las 8 semanas de dieta rica en grasa ratones macho en ayuno de 16 h fueron sometidos a un test de tolerancia a la glucosa (GTT) (2 g / kg; n = 6). (B) Niveles de insulina en plasma durante la GTT (n = 6). Los datos representan la media ± SEM. ** p <0.01, *** p <0.001 vs. ratones control loxP.

Considerando el resultado anterior, decidimos administrar insulina para analizar la respuesta de la insulina en el manejo de glucosa en una dieta rica en grasas. Los resultados de ITT mostraron que L-OPA1 KO mostró una mayor respuesta a la insulina en comparación con los ratones control loxP. Estos resultados demostraron que L-OPA1 KO están protegidos contra la resistencia a la insulina inducida por la dieta debido a su mejor capacidad en el manejo de glucosa (Figura 61).

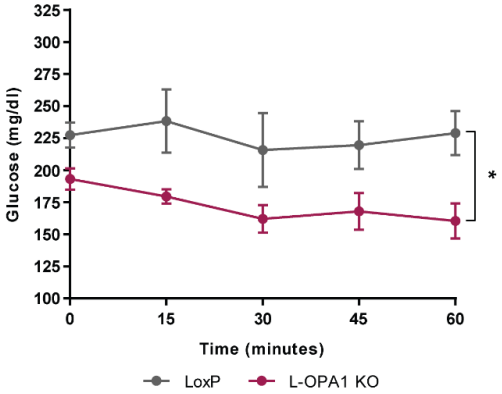

Figura 61. Los ratones L-OPA1 KO exhiben una mayor respuesta a la insulina. A las 10 semanas de dieta rica en grasa ratones macho en ayuno de 4 h fueron estimulados con insulina y sometidos a un test de tolerancia a la insulina (ITT). 1U / kg; n = 6. Los datos representan la media ± SEM. * p <0.05 vs. ratones control loxP.

Identificación de factores clave en la respuesta metabólica adaptativa asociada a la deficiencia de OPA1 en el hígado

Después de evaluar la función mitocondrial y caracterizar el fenotipo metabólico en ratones L-OPA1 KO, nuestro objetivo fue determinar el participante o los participantes moleculares responsables de la adaptación metabólica en respuesta a la disfunción mitocondrial causada por la deficiencia de OPA1 en el hígado. Para identificar aún más los reguladores potenciales de la inducción de FGF21, se realizó un análisis de transcriptómica en hígados de ratones L-OPA1 KO y control loxP. Un total de 2059 genes únicos se expresaron diferencialmente (aumento o disminución de 1.5 veces, valor de p ajustado <0.01), entre los que 1214 (59%) estaban significativamente sobrexpresados y 845 (41%) estaban significativamente disminuidos.

El análisis de enriquecimiento del conjunto de genes (GSEA) reveló que la pérdida de OPA1 en el hígado resultó en patrones de expresión génica alterados en L-OPA1 KO en comparación con los ratones de control loxP, revelando entre las vías que están reguladas positivamente, un enriquecimiento en las vías de respuesta al estrés, entre ellas la respuesta al mal plegamiento de proteínas del retículo endoplásmico (UPRer) y genes asociados al estrés mitocondrial (Figura 62.A-B). Entre las vías reguladas negativamente, se observó un enriquecimiento en las vías relacionadas con la capacidad oxidativa, lo que confirma la disfunción mitocondrial provocada por la ablación de OPA1 (Figura 62.A). Los genes asociados al estrés mitocondrial (mt-stress) se refieren a una firma de estrés mitocondrial compartida por muchas condiciones mitocondriales en modelos celulares y animales, y que se caracteriza principalmente por la activación de las vías de biosíntesis de aminoácidos (Figura 62.C).

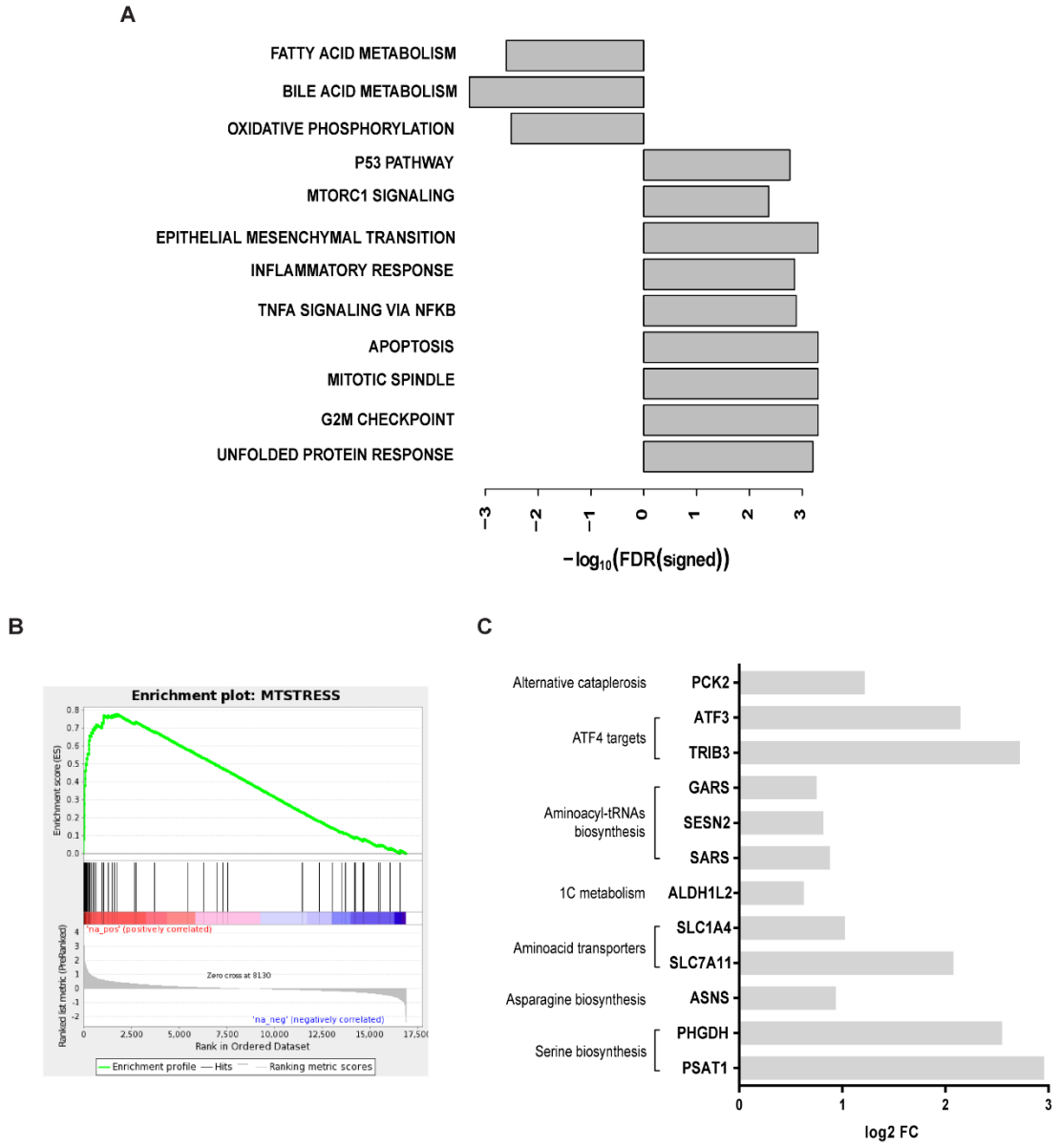

Figura 62. La deleción de OPA1 en el hígado conduce a alteraciones en la expresión génica. Gráfico de barras que muestra las vías enriquecidas en análisis de GSEA filtradas por FDR <0.01. n = 6, se usaron hígados de ratones de 8 semanas de edad en dieta normal. Los datos representan la media clasificada de -log10 fold-change. vs ratones control loxP.

Además, el análisis de genes individuales y la validación independiente por PCR cuantitativa (qPCR) indicaron una mayor expresión de genes involucrados en la respuesta de UPRmt, como *hspa9*, *lonp1*, *atf5* y *atf4*, que codifica para mtHSP70, proteasa LON, ATF5 y ATF4 (Figura 63).

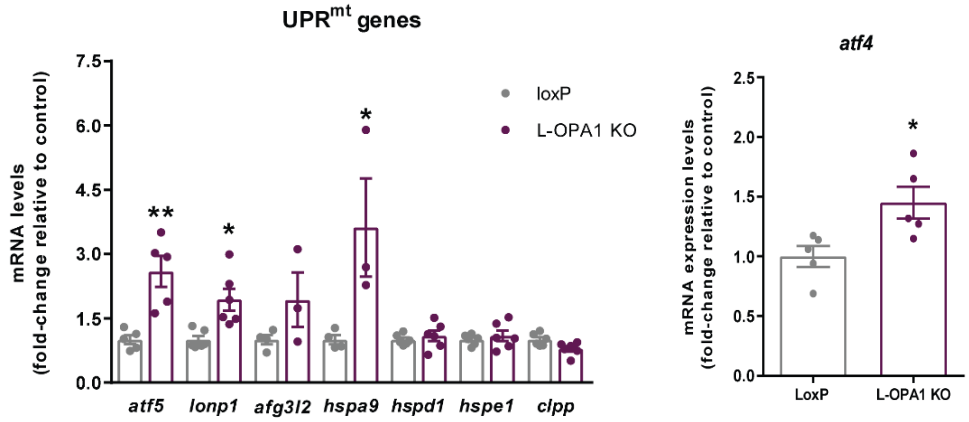

Figura 63. Los genes de UPRmt mediados por ATF5 se activan en hígado OPA1-KO. Panel izquierdo: expresión de los *genes atf5, lonp1, afg3l2, hspa9, hspd1, hspe1* y *clpp* en el hígado de los ratones loxP y L-OPA1 KO (n = 5). Panel derecho: expresión del gen atf4 en hígado de ratones loxP y OPA1-KO (n = 5). Los datos representan la media ± SEM. * p <0,05, ** p <0,01 frente a ratones control loxP.

Dada la observación de que tanto los genes del UPRer como de UPRmt están activados, examinamos también la activación de estas vías mediante el análisis de expresión de proteínas. Los resultados de western blot confirmaron la activación de las ramas del UPRer, mediadas por IRE1a y ATF6 (Figura 64.A-B).

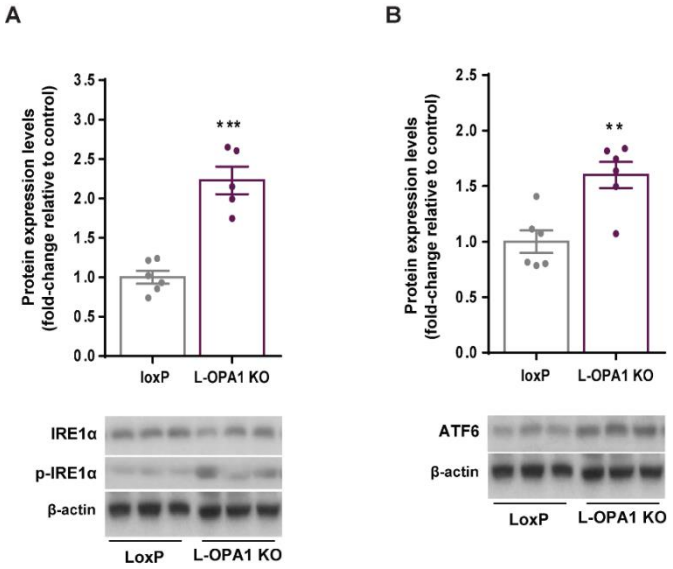

Figura 64. p-IRE1α y ATF6 se activan en hígados deficientes en OPA1. (A) Blot representativo y niveles de expresión de proteínas de p-IRE1α / IRE1α. (B) Blot representativo y niveles de expresión de proteínas de ATF6 en homogeneizados de hígado de control loxP y L-OPA1 KO. Valores corregidos por β-actina. Los datos representan la media ± SEM. ** p <0,01 y *** p <0,001 frente a ratones control loxP.

En paralelo con la activación de efectores del UPRmt como las proteasas ATF5, mtHSP70, LON (Figura 65.A) y AFG3L2 en homogenizados totales de hígado de ratones L-OPA1 KO (Figura 65.B).

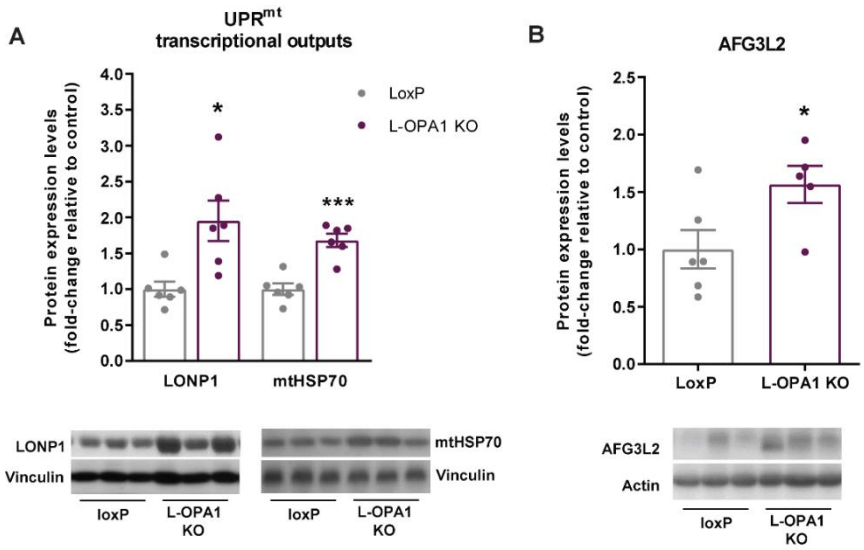

Figura 65. El programa de transcripción UPRmt se activa en hígados L-OPA1 KO. (A) Representación de Western blot y proteína representativa de dianas ATF5, mtHSP70 y LONP1. (B) Expresión representativa de Western blot y proteína de AFG3L2, en homogenados de tejido hepático de ratones loxP y L-OPA1 KO de 8 semanas de edad (n = 5-6). Los datos representan la media ± SEM. * p <0,05; *** p <0,001 frente a ratones control loxP.

Dada la observación de que la eliminación de OPA1 específica del músculo esquelético conduce a una sobreexpresión de los genes abajo del gen *atf4* en paralelo y mayores niveles de FGF21 en el músculo y en plasma (Rodríguez-Nuevo et al.2018), que ha sido descrito como una molécula que mejora el metabolismo, decidimos evaluar más a fondo el papel de FGF21 en la adaptación metabólica observada en ratones L-OPA1 KO. Evaluamos los niveles de expresión del gen fgf21 en el hígado y los niveles circulantes de FGF21 y, como sospechábamos, la expresión del gen fgf21 aumentó mucho en el hígado en paralelo con los niveles de FGF21 circulantes 20 veces mayores en ratones con deficiencia de L-OPA1 (Figura 66.A-B).

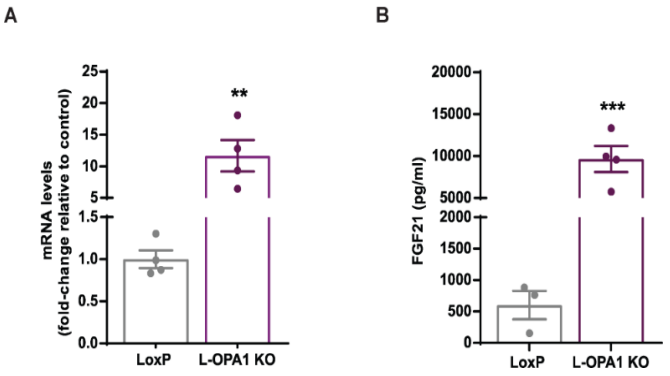

Figura 66. FGF21 se potencia con la pérdida de función OPA1 en el hígado. (A) Expresión del gen Fgf21 en hígado de lox y L-OPA1 KO (n = 4). (B) Niveles de FGF21 en plasma de ratones loxP y L-OPA1 KO (n = 4). Los datos representan la media ± SEM. ** p <0,01 frente a ratones control loxP.

La inducción de UPRmt y FGF21 también se observó en células de fibroblastos embrionarios de ratón con deficiencia de OPA1 (MEF Opa1$^{-/-}$) (Figura 67.A-B).

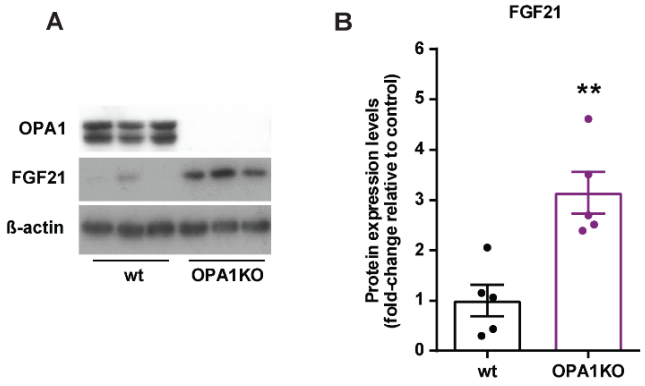

Figura 67. FGF21 se induce en células OPA1 - / - MEF. (A) Western blot representativo de los niveles de proteína OPA1 y FGF21 en el extracto celular total de fibroblastos embrionarios de ratón de tipo salvaje control (wt) y fibroblastos embrionarios de ratón OPA1-KO (OPA1KO). (B) Niveles de proteína FGF21 en el extracto celular total de células wt y OPA1KO (n = 3). Los datos representan la media ± SEM. ** p <0.01 vs. células control.

Sin embargo, solo se observó en este modelo celular la fosforilación de eIF2α y la activación de ATF4 (Figura 68.A-D), también parte de ISR, lo que sugiere que la activación de la respuesta al estrés del ER podría ser una reacción colateral específica del tejido causada por el estrés asociado a la eliminación de OPA1 en el hígado y, por otro lado, FGF21 posiblemente es inducida por la activación de la respuesta al estrés mitocondrial desencadenada por la ablación de OPA1 de manera celular autónoma. Debido a que las células MEF Opa1$^{-/-}$ demostraron una regulación positiva de FGF21, a partir de este momento decidimos establecer estas células como nuestro modelo para los estudios mecanicistas.

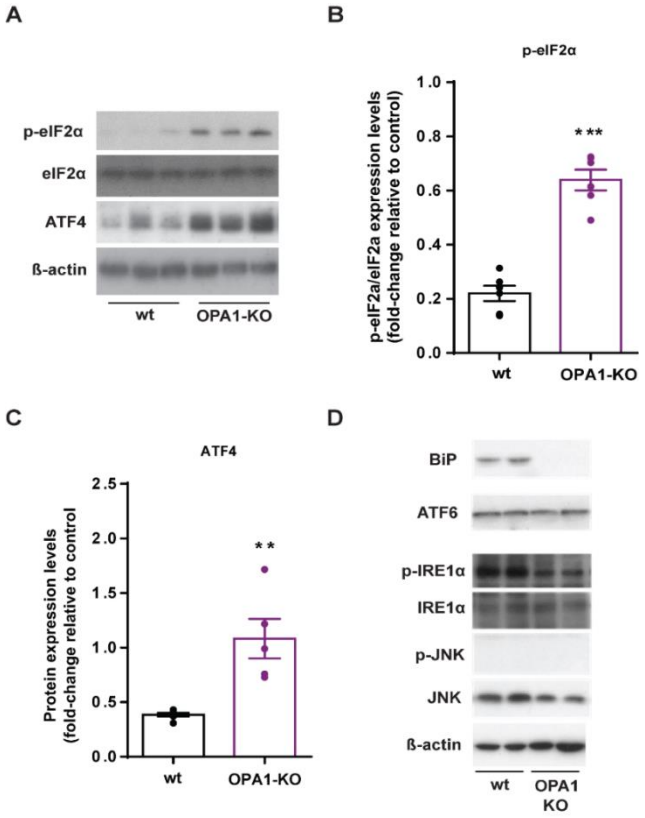

Figura 68. p-eIF2a y ATF4 se inducen en células OPA1 - / - MEF en ausencia de ER estrés. (A) Western blot representativo de los niveles de proteína p-eIF2a, eIF2a y ATF4 en el extracto celular total de fibroblastos embrionarios de ratón de tipo salvaje de control (wt) y fibroblastos embrionarios de ratón OPA1-KO (OPA1KO). (B-C) Niveles de proteína de p-eIF2α / eIF2α y extracto de células ATF4 total de células wt y OPA1KO (D) Niveles de proteínas de marcadores UPRer de ramas ATF6 e IRE1α (n = 3). Los datos representan la media ± SEM. ** p <0.01 vs. células control.

Seguidamente, evaluamos la activación de UPRmt en células MEF Opa1$^{-/-}$ y observamos y tal y como habíamos observado en el hígado, ATF5 y sus dianas, LONP1 y mtHSP70 se también se activan en la ausencia de OPA1 en estas células (Figura 69.A-B).

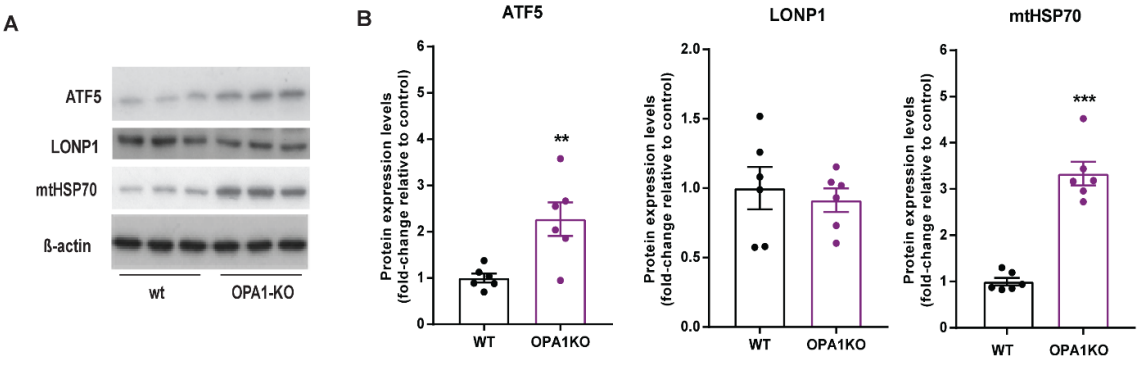

Figura 69. El programa transcripcional UPRmt se activa en las células OPA1 - / - MEF. (A) Western blot representativo de ATF5 y sus dianas LONP1 y mtHSP70 en extractos celulares totales de células MEF control (wt) y MEF OPA1-KO (OPA1KO). (B) Niveles de proteínas de ATF5, LONP1 y mtHSP70 en extractos celulares totales de células wt y OPA1KO (n = 3). Los datos representan la media ± SEM. ** p <0.01, *** p> 0.001 vs. células control.

Como observamos anteriormente, la eliminación de OPA1 en el hígado condujo a la reducción de las subunidades de los complejos OxPhos, a la inestabilidad del mtDNA y la reducción de los niveles de TFAM que posiblemente podrían conducir a la acumulación de péptidos en las mitocondrias y bloquear la importación de proteínas, nos llevó a la sospecha de que ATF5 jugaría un papel en la activación de UPRmt tras la eliminación de OPA1. Se ha descrito que ATF5 responde específicamente a las perturbaciones en la importación de proteínas mitocondriales mediante la translocación de ATF5 desde las mitocondrias al núcleo y consecuente acumulación en el mismo.

Por microscopía confocal, examinamos la localización de ATF5 en las células MEF Opa1$^{-/-}$. ATF5 se acumuló en los núcleos, rara vez se co-localizó con las mitocondrias y sorprendentemente formó aglomerados en el citosol de las células MEF Opa1$^{-/-}$, lo que sugiere que ATF5 podría no solo mediar en una respuesta retrógrada mitocondrial, sino también probablemente en una respuesta citosólica al error de las proteínas mitocondriales, posiblemente similar a la UPRam observada en levaduras (Callegari y Dennerlein 2018).

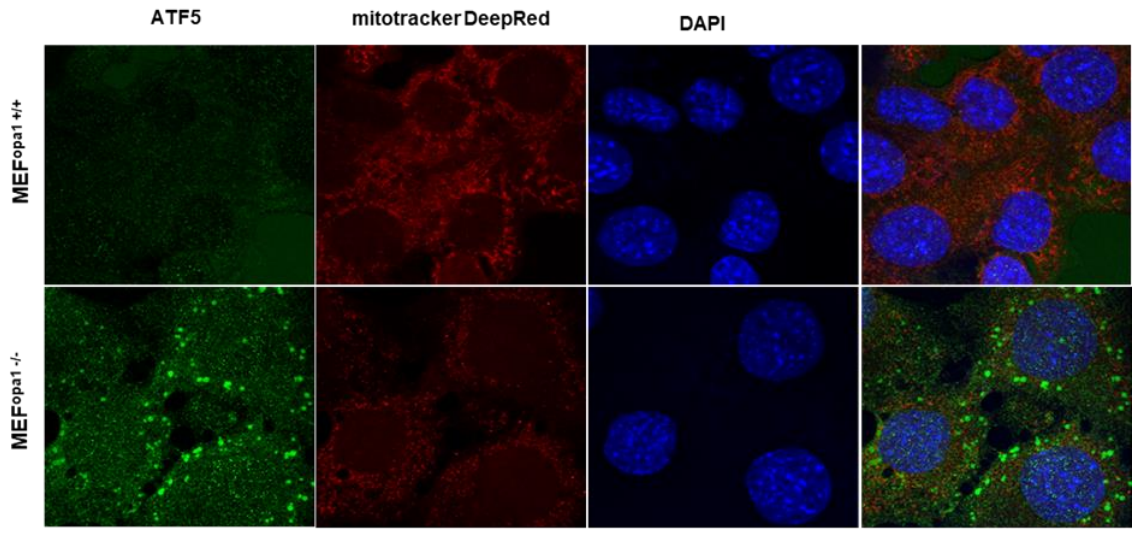

Figura 70. ATF5 se acumula en el citosol y se localiza conjuntamente en los núcleos de las células con deficiencia de OPA1. Inmunofluorescencia de ATF5 y del marcador mitocondrial DeepRed mitotracker en MEF wt (panel superior) frente a células MEF Opa1 - / - (panel inferior). El ATF5 se localiza en los núcleos de las células MEF Opa1 - / - como se demuestra mediante la localización conjunta con el marcador nuclear DAPI.

OPA1 controla la morfología de la cresta que no solo asegura la organización funcional de los supercomplejos mitocondriales adaptados para la producción eficiente de ATP y mantiene intacto el DNA mitocondrial (mtDNA) (Frezza et al. 2006). Nuestros

resultados mostraron que, de hecho, la ablación de OPA1 conduce a un estrés mitocondrial crónico y desencadena la activación de UPRmt en el hígado, lo que sugiere que OPA1 tiene un papel importante en la proteostasis mitocondrial. El propio ATF5 alberga una secuencia de direccionamiento mitocondrial que potencialmente le permite responder específicamente a la reducción de la eficiencia de importación de proteínas mitocondriales causada por una proteostasis mitocondrial deteriorada (Fiorese et al.2016). Nuestros resultados revelaron la acumulación de ATF5 en el núcleo y el citosol de las células deficientes de OPA1, por lo que nos proponemos lo a ATF5 como el factor clave en la activación de UPRmt.

Para obtener más información sobre el papel de ATF5 en la inducción de FGF21 tras la eliminación de OPA1, desarrollamos un modelo celular deficiente en Atf5 utilizando la tecnología CRISPR-Cas9. Usando esta tecnología, pudimos obtener una eliminación del 61.9% del mRNA de Atf5. Al eliminar el gen Atf5, observamos una reducción sustancial en los genes de Opa1 y Fgf21, mientras que el gen Atf4 permaneció inalterado (Figura 61), lo que sugiere que, por un lado, ATF5 interactúa con OPA1 y, por otro lado, la inducción de FGF21 depende bastante de Activación ATF5 (Figure 61).

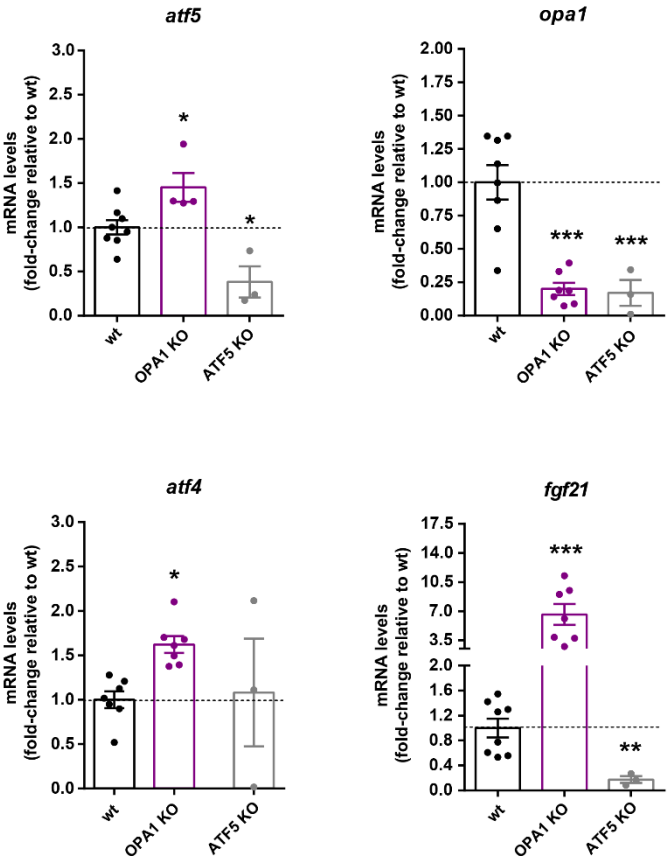

Figura 61. La eliminación de ATF5 en células wt MEF provoca una reducción en OPA1 y FGF21 pero no en los niveles de ARNm de ATF4. atf5 (panel superior izquierdo), opa1 (panel superior derecho), atf4 (panel inferior izquierdo) y fgf21 (panel inferior derecho) niveles de expresión génica de células wt, OPA1 y ATF5 KO. n = 3-8. Los datos representan la media ± SEM. * p <0.05, ** p <0.01, *** p <0.001 vs células control.

7.5 Conclusiones

En base a los resultados de esta tesis doctoral, proponemos las siguientes conclusiones:

1. La ablación de OPA1 da como resultado una disfunción mitocondrial caracterizada por defectos en la capacidad respiratoria mitocondrial, reducción del número de copias de ADNmt, perturbaciones en la organización de las crestas mitocondriales y proteostasis mitocondrial; Esto genera estrés mitocondrial crónico que conduce a la activación de una respuesta al estrés mitocondrial y al UPRmt.

2. La respuesta al estrés mitocondrial causado por la pérdida de función OPA1 específica del hígado conduce a la inducción de FGF21.

3. La deficiencia de OPA1 en el hígado provoca una tolerancia mejorada a la glucosa y protege contra la obesidad y la resistencia a la insulina inducidas por la dieta, posiblemente debido a la acción de FGF21.

4. La ausencia de OPA1 conduce a la activación de UPRmt mediada por la acumulación de ATF5 en el núcleo y en el citosol, que modula la inducción de FGF21 en FGF21 en células deficientes en OPA1.

5. Proponemos un modelo en el que la deficiencia de OPA1 causa estrés mitocondrial crónico que desencadena una respuesta mitocondrial específica que eventualmente se vuelve sistémica y mejora la homeostasis de la glucosa. Además, sugerimos ATF5 como el principal mediador de esta respuesta.

8

References

8 References

Akepati, Vasudheva Reddy; Müller, Eva-Christina; Otto, Albrecht; Strauss, Holger M.; Portwich, Michael; Alexander, Christiane (2008): Characterization of OPA1 isoforms isolated from mouse tissues. In *Journal of neurochemistry* 106 (1), pp. 372–383. DOI: 10.1111/j.1471-4159.2008.05401.x.

Alexander, C.; Votruba, M.; Pesch, U. E.; Thiselton, D. L.; Mayer, S.; Moore, A. et al. (2000): OPA1, encoding a dynamin-related GTPase, is mutated in autosomal dominant optic atrophy linked to chromosome 3q28. In *Nature genetics* 26 (2), pp. 211–215. DOI: 10.1038/79944.

Anand, Ruchika; Wai, Timothy; Baker, Michael J.; Kladt, Nikolay; Schauss, Astrid C.; Rugarli, Elena; Langer, Thomas (2014): The i-AAA protease YME1L and OMA1 cleave OPA1 to balance mitochondrial fusion and fission. In *The Journal of cell biology* 204 (6), pp. 919–929. DOI: 10.1083/jcb.201308006.

Ayala, Julio E.; Samuel, Varman T.; Morton, Gregory J.; Obici, Silvana; Croniger, Colleen M.; Shulman, Gerald I. et al. (2010): Standard operating procedures for describing and performing metabolic tests of glucose homeostasis in mice. In *Disease models & mechanisms* 3 (9-10), pp. 525–534. DOI: 10.1242/dmm.006239.

Baker, Brooke M.; Nargund, Amrita M.; Sun, Tiffany; Haynes, Cole M. (2012): Protective coupling of mitochondrial function and protein synthesis via the eIF2α kinase GCN-2. In *PLoS genetics* 8 (6), e1002760. DOI: 10.1371/journal.pgen.1002760.

Baker, Michael J.; Lampe, Philipp A.; Stojanovski, Diana; Korwitz, Anne; Anand, Ruchika; Tatsuta, Takashi; Langer, Thomas (2014): Stress-induced OMA1 activation and autocatalytic turnover regulate OPA1-dependent mitochondrial dynamics. In *The EMBO Journal* 33 (6), pp. 578–593. DOI: 10.1002/embj.201386474.

Baricault, Laurent; Ségui, Bruno; Guégand, Laurie; Olichon, Aurélien; Valette, Annie; Larminat, Florence; Lenaers, Guy (2007): OPA1 cleavage depends on decreased mitochondrial ATP level and bivalent metals. In *Experimental cell research* 313 (17), pp. 3800–3808. DOI: 10.1016/j.yexcr.2007.08.008.

Bender, Tom; Lewrenz, Ilka; Franken, Sebastian; Baitzel, Catherina; Voos, Wolfgang (2011): Mitochondrial enzymes are protected from stress-induced aggregation by mitochondrial chaperones and the Pim1/LON protease. In *Molecular Biology of the Cell* 22 (5), pp. 541–554. DOI: 10.1091/mbc.E10-08-0718.

Bereiter-Hahn, J.; Vöth, M. (1994): Dynamics of mitochondria in living cells: shape changes, dislocations, fusion, and fission of mitochondria. In *Microscopy research and technique* 27 (3), pp. 198–219. DOI: 10.1002/jemt.1070270303.

Bhaskaran, Shylesh; Pharaoh, Gavin; Ranjit, Rojina; Murphy, Ashley; Matsuzaki, Satoshi; Nair, Binoj C. et al. (2018): Loss of mitochondrial protease ClpP protects mice from diet-induced obesity and insulin resistance. In *EMBO reports* 19 (3). DOI: 10.15252/embr.201745009.

Bleazard, W.; McCaffery, J. M.; King, E. J.; Bale, S.; Mozdy, A.; Tieu, Q. et al. (1999): The dynamin-related GTPase Dnm1 regulates mitochondrial fission in yeast. In *Nature cell biology* 1 (5), pp. 298–304. DOI: 10.1038/13014.

Bota, Daniela A.; Davies, Kelvin J. A. (2002): Lon protease preferentially degrades oxidized mitochondrial aconitase by an ATP-stimulated mechanism. In *Nature cell biology* 4 (9), pp. 674–680. DOI: 10.1038/ncb836.

Brand, M. D.; Reynafarje, B.; Lehninger, A. L. (1976): Re-evaluation of the H+/site ratio of mitochondrial electron transport with the oxygen pulse technique. In *The Journal of biological chemistry* 251 (18), pp. 5670–5679.

Callegari, Sylvie; Dennerlein, Sven (2018): Sensing the Stress: A Role for the UPRmt and UPRam in the Quality Control of Mitochondria. In *Frontiers in cell and developmental biology* 6, p. 31. DOI: 10.3389/fcell.2018.00031.

Chacinska, Agnieszka; Koehler, Carla M.; Milenkovic, Dusanka; Lithgow, Trevor; Pfanner, Nikolaus (2009): Importing mitochondrial proteins: machineries and mechanisms. In *Cell* 138 (4), pp. 628–644. DOI: 10.1016/j.cell.2009.08.005.

Chan, David C. (2012): Fusion and fission: interlinked processes critical for mitochondrial health. In *Annual review of genetics* 46, pp. 265–287. DOI: 10.1146/annurev-genet-110410-132529.

Chen, Hsiuchen; Chan, David C. (2004): Mitochondrial dynamics in mammals. In *Current topics in developmental biology* 59, pp. 119–144. DOI: 10.1016/S0070-2153(04)59005-1.

Chen, Hsiuchen; Chomyn, Anne; Chan, David C. (2005): Disruption of fusion results in mitochondrial heterogeneity and dysfunction. In *The Journal of biological chemistry* 280 (28), pp. 26185–26192. DOI: 10.1074/jbc.M503062200.

Chen, Hsiuchen; Detmer, Scott A.; Ewald, Andrew J.; Griffin, Erik E.; Fraser, Scott E.; Chan, David C. (2003): Mitofusins Mfn1 and Mfn2 coordinately regulate mitochondrial fusion and are essential for embryonic development. In *The Journal of cell biology* 160 (2), pp. 189–200. DOI: 10.1083/jcb.200211046.

Chen, Hsiuchen; McCaffery, J. Michael; Chan, David C. (2007): Mitochondrial fusion protects against neurodegeneration in the cerebellum. In *Cell* 130 (3), pp. 548–562. DOI: 10.1016/j.cell.2007.06.026.

Chen, J. J.; London, I. M. (1995): Regulation of protein synthesis by heme-regulated eIF-2 alpha kinase. In *Trends in biochemical sciences* 20 (3), pp. 105–108. DOI: 10.1016/s0968-0004(00)88975-6.

Cipolat, Sara; Martins de Brito, Olga; Dal Zilio, Barbara; Scorrano, Luca (2004): OPA1 requires mitofusin 1 to promote mitochondrial fusion. In *Proceedings of the National Academy of Sciences of the United States of America* 101 (45), pp. 15927–15932. DOI: 10.1073/pnas.0407043101.

Civiletto, Gabriele; Varanita, Tatiana; Cerutti, Raffaele; Gorletta, Tatiana; Barbaro, Serena; Marchet, Silvia et al. (2015): Opa1 overexpression ameliorates the phenotype of two mitochondrial disease mouse models. In *Cell Metabolism* 21 (6), pp. 845–854. DOI: 10.1016/j.cmet.2015.04.016.

Cogliati, Sara; Enriquez, Jose A.; Scorrano, Luca (2016): Mitochondrial Cristae: Where Beauty Meets Functionality. In *Trends in biochemical sciences* 41 (3), pp. 261–273. DOI: 10.1016/j.tibs.2016.01.001.

Cogliati, Sara; Frezza, Christian; Soriano, Maria Eugenia; Varanita, Tatiana; Quintana-Cabrera, Ruben; Corrado, Mauro et al. (2013): Mitochondrial cristae shape determines respiratory chain supercomplexes assembly and respiratory efficiency. In *Cell* 155 (1), pp. 160–171. DOI: 10.1016/j.cell.2013.08.032.

Curtis, Jessica M.; Hahn, Wendy S.; Stone, Matthew D.; Inda, Jacob J.; Droullard, David J.; Kuzmicic, Jovan P. et al. (2012): Protein carbonylation and adipocyte mitochondrial function. In *The Journal of biological chemistry* 287 (39), pp. 32967–32980. DOI: 10.1074/jbc.M112.400663.

D'Amico, Davide; Sorrentino, Vincenzo; Auwerx, Johan (2017): Cytosolic Proteostasis Networks of the Mitochondrial Stress Response. In *Trends in biochemical sciences* 42 (9), pp. 712–725. DOI: 10.1016/j.tibs.2017.05.002.

Delettre, C.; Lenaers, G.; Griffoin, J. M.; Gigarel, N.; Lorenzo, C.; Belenguer, P. et al. (2000): Nuclear gene OPA1, encoding a mitochondrial dynamin-related protein, is mutated in dominant optic atrophy. In *Nature genetics* 26 (2), pp. 207–210. DOI: 10.1038/79936.

Dell'agnello, Carlotta; Leo, Sara; Agostino, Alessandro; Szabadkai, György; Tiveron, Cecilia; Zulian, Alessandra et al. (2007): Increased longevity and refractoriness to Ca(2+)-dependent neurodegeneration in Surf1 knockout mice. In *Human molecular genetics* 16 (4), pp. 431–444. DOI: 10.1093/hmg/ddl477.

Deng, Jing; Harding, Heather P.; Raught, Brian; Gingras, Anne-Claude; Berlanga, Juan Jose; Scheuner, Donalyn et al. (2002): Activation of GCN2 in UV-irradiated cells inhibits translation. In *Current biology : CB* 12 (15), pp. 1279–1286.

Desautels, M.; Goldberg, A. L. (1982): Liver mitochondria contain an ATP-dependent, vanadate-sensitive pathway for the degradation of proteins. In *Proceedings of the National Academy of Sciences of the United States of America* 79 (6), pp. 1869–1873. DOI: 10.1073/pnas.79.6.1869.

Dever, T. E.; Feng, L.; Wek, R. C.; Cigan, A. M.; Donahue, T. F.; Hinnebusch, A. G. (1992): Phosphorylation of initiation factor 2 alpha by protein kinase GCN2 mediates gene-specific translational control of GCN4 in yeast. In *Cell* 68 (3), pp. 585–596.

Dogan, Sukru Anil; Pujol, Claire; Maiti, Priyanka; Kukat, Alexandra; Wang, Shuaiyu; Hermans, Steffen et al. (2014): Tissue-specific loss of DARS2 activates stress responses independently of respiratory chain deficiency in the heart. In *Cell Metabolism* 19 (3), pp. 458–469. DOI: 10.1016/j.cmet.2014.02.004.

Duvezin-Caubet, Stéphane; Jagasia, Ravi; Wagener, Johannes; Hofmann, Sabine; Trifunovic, Aleksandra; Hansson, Anna et al. (2006): Proteolytic processing of OPA1 links mitochondrial dysfunction to alterations in mitochondrial morphology. In *The Journal of biological chemistry* 281 (49), pp. 37972–37979. DOI: 10.1074/jbc.M606059200.

Eiberg, H.; Kjer, B.; Kjer, P.; Rosenberg, T. (1994): Dominant optic atrophy (OPA1) mapped to chromosome 3q region. I. Linkage analysis. In *Human molecular genetics* 3 (6), pp. 977–980. DOI: 10.1093/hmg/3.6.977.

Elachouri, Ghizlane; Vidoni, Sara; Zanna, Claudia; Pattyn, Alexandre; Boukhaddaoui, Hassan; Gaget, Karen et al. (2011): OPA1 links human mitochondrial genome maintenance to mtDNA replication and distribution. In *Genome research* 21 (1), pp. 12–20. DOI: 10.1101/gr.108696.110.

Falkenberg, Maria; Larsson, Nils-Göran; Gustafsson, Claes M. (2007): DNA replication and transcription in mammalian mitochondria. In *Annual review of biochemistry* 76, pp. 679–699. DOI: 10.1146/annurev.biochem.76.060305.152028.

Fiorese, Christopher J.; Schulz, Anna M.; Lin, Yi-Fan; Rosin, Nadine; Pellegrino, Mark W.; Haynes, Cole M. (2016): The Transcription Factor ATF5 Mediates a Mammalian Mitochondrial UPR. In *Current biology : CB* 26 (15), pp. 2037–2043. DOI: 10.1016/j.cub.2016.06.002.

Frezza, Christian; Cipolat, Sara; Martins de Brito, Olga; Micaroni, Massimo; Beznoussenko, Galina V.; Rudka, Tomasz et al. (2006): OPA1 controls apoptotic cristae remodeling independently from mitochondrial fusion. In *Cell* 126 (1), pp. 177–189. DOI: 10.1016/j.cell.2006.06.025.

Frezza, Christian; Cipolat, Sara; Scorrano, Luca (2007): Organelle isolation: functional mitochondria from mouse liver, muscle and cultured fibroblasts. In *Nature protocols* 2 (2), pp. 287–295. DOI: 10.1038/nprot.2006.478.

Friedman, Jonathan R.; Lackner, Laura L.; West, Matthew; DiBenedetto, Jared R.; Nunnari, Jodi; Voeltz, Gia K. (2011): ER tubules mark sites of mitochondrial division. In *Science (New York, N.Y.)* 334 (6054), pp. 358–362. DOI: 10.1126/science.1207385.

Granot, Zvi; Kobiler, Oren; Melamed-Book, Naomi; Eimerl, Sarah; Bahat, Assaf; Lu, Bin et al. (2007): Turnover of mitochondrial steroidogenic acute regulatory (StAR) protein by Lon protease: the unexpected effect of proteasome inhibitors. In *Molecular endocrinology (Baltimore, Md.)* 21 (9), pp. 2164–2177. DOI: 10.1210/me.2005-0458.

Gray, M. W. (1999): Evolution of organellar genomes. In *Current opinion in genetics & development* 9 (6), pp. 678–687. DOI: 10.1016/s0959-437x(99)00030-1.

Gray, M. W.; Burger, G.; Lang, B. F. (2001): The origin and early evolution of mitochondria. In *Genome biology* 2 (6), REVIEWS1018. DOI: 10.1186/gb-2001-2-6-reviews1018.

Griparic, Lorena; Kanazawa, Takayuki; van der Bliek, Alexander M. (2007): Regulation of the mitochondrial dynamin-like protein Opa1 by proteolytic cleavage. In *The Journal of cell biology* 178 (5), pp. 757–764. DOI: 10.1083/jcb.200704112.

Guerrieri, F.; Nelson, B. D. (1975): Studies on the characteristics of a proton pump in phospholipid vesicles inlayed with purified complex III from beef heart mitochondria. In *FEBS letters* 54 (3), pp. 339–342. DOI: 10.1016/0014-5793(75)80935-5.

Guillery, Olwenn; Malka, Florence; Landes, Thomas; Guillou, Emmanuelle; Blackstone, Craig; Lombès, Anne et al. (2008): Metalloprotease-mediated OPA1 processing is modulated by the mitochondrial membrane potential. In *Biology of the cell* 100 (5), pp. 315–325. DOI: 10.1042/BC20070110.

Gunter, T. E.; Buntinas, L.; Sparagna, G. C.; Gunter, K. K. (1998): The Ca2+ transport mechanisms of mitochondria and Ca2+ uptake from physiological-type Ca2+ transients. In *Biochimica et biophysica acta* 1366 (1-2), pp. 5–15. DOI: 10.1016/s0005-2728(98)00117-0.

Hansen, Jakob; Gregersen, Niels; Bross, Peter (2005): Differential degradation of variant medium-chain acyl-CoA dehydrogenase by the protein quality control proteases Lon and ClpXP. In *Biochemical and Biophysical Research Communications* 333 (4), pp. 1160–1170. DOI: 10.1016/j.bbrc.2005.06.024.

Harding, H. P.; Zhang, Y.; Ron, D. (1999): Protein translation and folding are coupled by an endoplasmic-reticulum-resident kinase. In *Nature* 397 (6716), pp. 271–274. DOI: 10.1038/16729.

Haynes, Cole M.; Ron, David (2010): The mitochondrial UPR - protecting organelle protein homeostasis. In *Journal of cell science* 123 (Pt 22), pp. 3849–3855. DOI: 10.1242/jcs.075119.

Hermann, G. J.; Shaw, J. M. (1998): Mitochondrial dynamics in yeast. In *Annual review of cell and developmental biology* 14, pp. 265–303. DOI: 10.1146/annurev.cellbio.14.1.265.

Hockenbery, D.; Nuñez, G.; Milliman, C.; Schreiber, R. D.; Korsmeyer, S. J. (1990): Bcl-2 is an inner mitochondrial membrane protein that blocks programmed cell death. In *Nature* 348 (6299), pp. 334–336. DOI: 10.1038/348334a0.

Hoppins, Suzanne; Lackner, Laura; Nunnari, Jodi (2007): The machines that divide and fuse mitochondria. In *Annual review of biochemistry* 76, pp. 751–780. DOI: 10.1146/annurev.biochem.76.071905.090048.

Horibe, Tomohisa; Hoogenraad, Nicholas J. (2007): The Chop Gene Contains an Element for the Positive Regulation of the Mitochondrial Unfolded Protein Response. In *PLoS ONE* 2 (9). DOI: 10.1371/journal.pone.0000835.

Hüttemann, Maik; Lee, Icksoo; Samavati, Lobelia; Yu, Hong; Doan, Jeffrey W. (2007): Regulation of mitochondrial oxidative phosphorylation through cell signaling. In *Biochimica et biophysica acta* 1773 (12), pp. 1701–1720. DOI: 10.1016/j.bbamcr.2007.10.001.

Ingerman, Elena; Perkins, Edward M.; Marino, Michael; Mears, Jason A.; McCaffery, J. Michael; Hinshaw, Jenny E.; Nunnari, Jodi (2005): Dnm1 forms spirals that are structurally tailored to fit mitochondria. In *The Journal of cell biology* 170 (7), pp. 1021–1027. DOI: 10.1083/jcb.200506078.

Ishihara, Naotada; Fujita, Yuu; Oka, Toshihiko; Mihara, Katsuyoshi (2006): Regulation of mitochondrial morphology through proteolytic cleavage of OPA1. In *The EMBO Journal* 25 (13), pp. 2966–2977. DOI: 10.1038/sj.emboj.7601184.

Ishihara, Naotada; Mihara, Katsuyoshi (2005): Mitochondrial dynamics regulated by fusion and fission. In *Tanpakushitsu kakusan koso. Protein, nucleic acid, enzyme* 50 (8), pp. 931–939.

Jayashankar, Vaishali; Mueller, Irina A.; Rafelski, Susanne M. (2016): Shaping the multi-scale architecture of mitochondria. In *Current opinion in cell biology* 38, pp. 45–51. DOI: 10.1016/j.ceb.2016.02.006.

Kang, Dongchon; Hamasaki, Naotaka (2002): Maintenance of mitochondrial DNA integrity: repair and degradation. In *Current genetics* 41 (5), pp. 311–322. DOI: 10.1007/s00294-002-0312-0.

Kaser, Michael; Kambacheld, Melanie; Kisters-Woike, Brigitte; Langer, Thomas (2003): Oma1, a novel membrane-bound metallopeptidase in mitochondria with activities overlapping with the m-AAA protease. In *The Journal of biological chemistry* 278 (47), pp. 46414–46423. DOI: 10.1074/jbc.M305584200.

Khan, Nahid A.; Nikkanen, Joni; Yatsuga, Shuichi; Jackson, Christopher; Wang, Liya; Pradhan, Swagat et al. (2017): mTORC1 Regulates Mitochondrial Integrated Stress Response and Mitochondrial Myopathy Progression. In *Cell Metabolism* 26 (2), 419-428.e5. DOI: 10.1016/j.cmet.2017.07.007.

Kim, Seong Hun; Kim, Kook Hwan; Kim, Hyoung-Kyu; Kim, Mi-Jeong; Back, Sung Hoon; Konishi, Morichika et al. (2015): Fibroblast growth factor 21 participates in adaptation to endoplasmic reticulum stress and attenuates obesity-induced hepatic metabolic stress. In *Diabetologia* 58 (4), pp. 809–818. DOI: 10.1007/s00125-014-3475-6.

Klionsky, Daniel J.; Abdelmohsen, Kotb; Abe, Akihisa; Abedin, Md Joynal; Abeliovich, Hagai; Acevedo Arozena, Abraham et al. (2016): Guidelines for the use and interpretation of assays for monitoring autophagy (3rd edition). In *Autophagy* 12 (1), pp. 1–222. DOI: 10.1080/15548627.2015.1100356.

Koshiba, Takumi; Detmer, Scott A.; Kaiser, Jens T.; Chen, Hsiuchen; McCaffery, J. Michael; Chan, David C. (2004): Structural basis of mitochondrial tethering by mitofusin complexes. In *Science (New York, N.Y.)* 305 (5685), pp. 858–862. DOI: 10.1126/science.1099793.

Kovermann, Peter; Truscott, Kaye N.; Guiard, Bernard; Rehling, Peter; Sepuri, Naresh B.; Müller, Hanne et al. (2002): Tim22, the essential core of the mitochondrial protein insertion complex, forms a voltage-activated and signal-gated channel. In *Molecular cell* 9 (2), pp. 363–373. DOI: 10.1016/s1097-2765(02)00446-x.

Kulkarni, Sameer S.; Joffraud, Magali; Boutant, Marie; Ratajczak, Joanna; Gao, Arwen W.; Maclachlan, Catherine et al. (2016): Mfn1 Deficiency in the Liver Protects Against Diet-Induced Insulin Resistance and Enhances the Hypoglycemic Effect of Metformin. In *Diabetes* 65 (12), pp. 3552–3560. DOI: 10.2337/db15-1725.

Liesa, Marc; Palacín, Manuel; Zorzano, Antonio (2009): Mitochondrial dynamics in mammalian health and disease. In *Physiological reviews* 89 (3), pp. 799–845. DOI: 10.1152/physrev.00030.2008.

Lill, Roland; Mühlenhoff, Ulrich (2008): Maturation of iron-sulfur proteins in eukaryotes: mechanisms, connected processes, and diseases. In *Annual review of biochemistry* 77, pp. 669–700. DOI: 10.1146/annurev.biochem.76.052705.162653.

Lin, Michael T.; Beal, M. Flint (2006): Mitochondrial dysfunction and oxidative stress in neurodegenerative diseases. In *Nature* 443 (7113), pp. 787–795. DOI: 10.1038/nature05292.

Livnat-Levanon, Nurit; Glickman, Michael H. (2011): Ubiquitin-proteasome system and mitochondria - reciprocity. In *Biochimica et biophysica acta* 1809 (2), pp. 80–87. DOI: 10.1016/j.bbagrm.2010.07.005.

Losón, Oliver C.; Song, Zhiyin; Chen, Hsiuchen; Chan, David C. (2013): Fis1, Mff, MiD49, and MiD51 mediate Drp1 recruitment in mitochondrial fission. In *Molecular Biology of the Cell* 24 (5), pp. 659–667. DOI: 10.1091/mbc.E12-10-0721.

Malka, Florence; Guillery, Olwenn; Cifuentes-Diaz, Carmen; Guillou, Emmanuelle; Belenguer, Pascale; Lombès, Anne; Rojo, Manuel (2005): Separate fusion of outer and inner mitochondrial membranes. In *EMBO reports* 6 (9), pp. 853–859. DOI: 10.1038/sj.embor.7400488.

Martin, Lee J. (2010): Mitochondrial and Cell Death Mechanisms in Neurodegenerative Diseases. In *Pharmaceuticals (Basel, Switzerland)* 3 (4), pp. 839–915. DOI: 10.3390/ph3040839.

Martinus, R. D.; Garth, G. P.; Webster, T. L.; Cartwright, P.; Naylor, D. J.; Høj, P. B.; Hoogenraad, N. J. (1996): Selective induction of mitochondrial chaperones in response to loss of the mitochondrial genome. In *European journal of biochemistry* 240 (1), pp. 98–103. DOI: 10.1111/j.1432-1033.1996.0098h.x.

Matsushima, Yuichi; Goto, Yu-ichi; Kaguni, Laurie S. (2010): Mitochondrial Lon protease regulates mitochondrial DNA copy number and transcription by selective degradation of mitochondrial transcription factor A (TFAM). In *Proceedings of the National Academy of Sciences of the United States of America* 107 (43), pp. 18410–18415. DOI: 10.1073/pnas.1008924107.

Mercer, Tim R.; Neph, Shane; Dinger, Marcel E.; Crawford, Joanna; Smith, Martin A.; Shearwood, Anne-Marie J. et al. (2011): The human mitochondrial transcriptome. In *Cell* 146 (4), pp. 645–658. DOI: 10.1016/j.cell.2011.06.051.

Merkwirth, Carsten; Dargazanli, Sascha; Tatsuta, Takashi; Geimer, Stefan; Löwer, Beatrix; Wunderlich, F. Thomas et al. (2008): Prohibitins control cell proliferation and apoptosis by regulating OPA1-dependent cristae morphogenesis in mitochondria. In *Genes & development* 22 (4), pp. 476–488. DOI: 10.1101/gad.460708.

Meurs, E.; Chong, K.; Galabru, J.; Thomas, N. S.; Kerr, I. M.; Williams, B. R.; Hovanessian, A. G. (1990): Molecular cloning and characterization of the human double-stranded RNA-activated protein kinase induced by interferon. In *Cell* 62 (2), pp. 379–390.

Michel, Sebastien; Canonne, Morgane; Arnould, Thierry; Renard, Patricia (2015): Inhibition of mitochondrial genome expression triggers the activation of CHOP-10 by a cell signaling dependent on the integrated stress response but not the mitochondrial unfolded protein response. In *Mitochondrion* 21, pp. 58–68. DOI: 10.1016/j.mito.2015.01.005.

Mishra, Prashant; Chan, David C. (2014): Mitochondrial dynamics and inheritance during cell division, development and disease. In *Nature reviews. Molecular cell biology* 15 (10), pp. 634–646. DOI: 10.1038/nrm3877.

Mishra, Prashant; Chan, David C. (2016): Metabolic regulation of mitochondrial dynamics. In *The Journal of cell biology* 212 (4), pp. 379–387. DOI: 10.1083/jcb.201511036.

Moehle, Erica A.; Shen, Koning; Dillin, Andrew (2019): Mitochondrial proteostasis in the context of cellular and organismal health and aging. In *The Journal of biological chemistry* 294 (14), pp. 5396–5407. DOI: 10.1074/jbc.TM117.000893.

Naresh, Nandhitha Uma; Haynes, Cole M. (2019): Signaling and Regulation of the Mitochondrial Unfolded Protein Response. In *Cold Spring Harbor perspectives in biology* 11 (6). DOI: 10.1101/cshperspect.a033944.

Nargund, Amrita M.; Fiorese, Christopher J.; Pellegrino, Mark W.; Deng, Pan; Haynes, Cole M. (2015): Mitochondrial and nuclear accumulation of the transcription factor ATFS-1 promotes OXPHOS recovery during the UPR(mt). In *Molecular cell* 58 (1), pp. 123–133. DOI: 10.1016/j.molcel.2015.02.008.

Neupert, Walter; Herrmann, Johannes M. (2007): Translocation of proteins into mitochondria. In *Annual review of biochemistry* 76, pp. 723–749. DOI: 10.1146/annurev.biochem.76.052705.163409.

Nunnari, Jodi; Suomalainen, Anu (2012): Mitochondria: in sickness and in health. In *Cell* 148 (6), pp. 1145–1159. DOI: 10.1016/j.cell.2012.02.035.

Okamoto, Koji; Shaw, Janet M. (2005): Mitochondrial morphology and dynamics in yeast and multicellular eukaryotes. In *Annual review of genetics* 39, pp. 503–536. DOI: 10.1146/annurev.genet.38.072902.093019.

Olichon, Aurélien; Baricault, Laurent; Gas, Nicole; Guillou, Emmanuelle; Valette, Annie; Belenguer, Pascale; Lenaers, Guy (2003): Loss of OPA1 perturbates the mitochondrial inner membrane structure and integrity, leading to cytochrome c release and apoptosis. In *The Journal of biological chemistry* 278 (10), pp. 7743–7746. DOI: 10.1074/jbc.C200677200.

Olivares, Shantel; Henkel, Anne S. (2017): Induction of fibroblast growth factor 21 does not require activation of the hepatic X-box binding protein 1 in mice. In *Molecular metabolism* 6 (12), pp. 1616–1624. DOI: 10.1016/j.molmet.2017.09.006.

Osman, Christof; Voelker, Dennis R.; Langer, Thomas (2011): Making heads or tails of phospholipids in mitochondria. In *The Journal of cell biology* 192 (1), pp. 7–16. DOI: 10.1083/jcb.201006159.

Otera, Hidenori; Wang, Chunxin; Cleland, Megan M.; Setoguchi, Kiyoko; Yokota, Sadaki; Youle, Richard J.; Mihara, Katsuyoshi (2010): Mff is an essential factor for mitochondrial recruitment of Drp1 during mitochondrial fission in mammalian cells. In *The Journal of cell biology* 191 (6), pp. 1141–1158. DOI: 10.1083/jcb.201007152.

Pakos-Zebrucka, Karolina; Koryga, Izabela; Mnich, Katarzyna; Ljujic, Mila; Samali, Afshin; Gorman, Adrienne M. (2016): The integrated stress response. In *EMBO reports* 17 (10), pp. 1374–1395. DOI: 10.15252/embr.201642195.

Pathak, V. K.; Schindler, D.; Hershey, J. W. (1988): Generation of a mutant form of protein synthesis initiation factor eIF-2 lacking the site of phosphorylation by eIF-2 kinases. In *Molecular and cellular biology* 8 (2), pp. 993–995. DOI: 10.1128/mcb.8.2.993.

Pereira, Renata Oliveira; Tadinada, Satya M.; Zasadny, Frederick M.; Oliveira, Karen Jesus; Pires, Karla Maria Pereira; Olvera, Angela et al. (2017): OPA1 deficiency promotes secretion of FGF21 from muscle that prevents obesity and insulin resistance. In *The EMBO Journal* 36 (14), pp. 2126–2145. DOI: 10.15252/embj.201696179.

Pharaoh, Gavin; Pulliam, Daniel; Hill, Shauna; Sataranatarajan, Kavithalakshmi; van Remmen, Holly (2016): Ablation of the mitochondrial complex IV assembly protein Surf1 leads to increased expression of the UPR(MT) and increased resistance to oxidative stress in primary cultures of fibroblasts. In *Redox biology* 8, pp. 430–438. DOI: 10.1016/j.redox.2016.05.001.

Pulliam, Daniel A.; Deepa, Sathyaseelan S.; Liu, Yuhong; Hill, Shauna; Lin, Ai-Ling; Bhattacharya, Arunabh et al. (2014): Complex IV-deficient Surf1(-/-) mice initiate mitochondrial stress responses. In *The Biochemical journal* 462 (2), pp. 359–371. DOI: 10.1042/BJ20140291.

Quirós, Pedro M.; Prado, Miguel A.; Zamboni, Nicola; D'Amico, Davide; Williams, Robert W.; Finley, Daniel et al. (2017): Multi-omics analysis identifies ATF4 as a key regulator of the mitochondrial stress response in mammals. In *The Journal of cell biology* 216 (7), pp. 2027–2045. DOI: 10.1083/jcb.201702058.

Quirós, Pedro M.; Ramsay, Andrew J.; Sala, David; Fernández-Vizarra, Erika; Rodríguez, Francisco; Peinado, Juan R. et al. (2012): Loss of mitochondrial protease OMA1 alters processing of the GTPase OPA1 and causes obesity and defective thermogenesis in mice. In *The EMBO Journal* 31 (9), pp. 2117–2133. DOI: 10.1038/emboj.2012.70.

Rahn, Jennifer J.; Stackley, Krista D.; Chan, Sherine S. L. (2013): Opa1 is required for proper mitochondrial metabolism in early development. In *PLoS ONE* 8 (3), e59218. DOI: 10.1371/journal.pone.0059218.

Rehling, Peter; Model, Kirstin; Brandner, Katrin; Kovermann, Peter; Sickmann, Albert; Meyer, Helmut E. et al. (2003): Protein insertion into the mitochondrial inner membrane by a twin-pore translocase. In *Science (New York, N.Y.)* 299 (5613), pp. 1747–1751. DOI: 10.1126/science.1080945.

Rodolfo, Carlo; Ciccosanti, Fabiola; Di Giacomo, Giuseppina; Piacentini, Mauro; Fimia, Gian Maria (2010): Proteomic analysis of mitochondrial dysfunction in neurodegenerative diseases. In *Expert review of proteomics* 7 (4), pp. 519–542. DOI: 10.1586/epr.10.43.

Rodríguez-Nuevo, Aida; Díaz-Ramos, Angels; Noguera, Eduard; Díaz-Sáez, Francisco; Duran, Xavier; Muñoz, Juan Pablo et al. (2018): Mitochondrial DNA and TLR9 drive muscle inflammation upon Opa1 deficiency. In *The EMBO Journal* 37 (10). DOI: 10.15252/embj.201796553.

Ryan, M. T.; Naylor, D. J.; Høj, P. B.; Clark, M. S.; Hoogenraad, N. J. (1997): The role of molecular chaperones in mitochondrial protein import and folding. In *International review of cytology* 174, pp. 127–193. DOI: 10.1016/s0074-7696(08)62117-8.

Sagan, Lynn (1967): On the origin of mitosing cells. In *Journal of Theoretical Biology* 14 (3), 225-IN6. DOI: 10.1016/0022-5193(67)90079-3.

Sagarra, M. R. de; Mayo, I.; Marco, S.; Rodríguez-Vilariño, S.; Oliva, J.; Carrascosa, J. L.; Casta ñ, J. G. (1999): Mitochondrial localization and oligomeric structure of HClpP, the human homologue of E. coli ClpP. In *Journal of molecular biology* 292 (4), pp. 819–825. DOI: 10.1006/jmbi.1999.3121.

Santagata, S.; Bhattacharyya, D.; Wang, F. H.; Singha, N.; Hodtsev, A.; Spanopoulou, E. (1999): Molecular cloning and characterization of a mouse homolog of bacterial ClpX, a novel mammalian class II member of the Hsp100/Clp chaperone family. In *The Journal of biological chemistry* 274 (23), pp. 16311–16319. DOI: 10.1074/jbc.274.23.16311.

Satoh, Masaaki; Hamamoto, Toshiro; Seo, Norimasa; Kagawa, Yasuo; Endo, Hitoshi (2003): Differential sublocalization of the dynamin-related protein OPA1 isoforms in mitochondria. In *Biochemical and Biophysical Research Communications* 300 (2), pp. 482–493. DOI: 10.1016/S0006-291X(02)02874-7.

Sebastián, David; Hernández-Alvarez, María Isabel; Segalés, Jessica; Sorianello, Eleonora; Muñoz, Juan Pablo; Sala, David et al.: Mitofusin 2 (Mfn2) links mitochondrial and endoplasmic reticulum function with insulin signaling and is essential for normal glucose homeostasis. In *Proceedings of the National Academy of Sciences of the United States of America* 109 (14), pp. 5523–5528.

Seo, Arnold Y.; Joseph, Anna-Maria; Dutta, Debapriya; Hwang, Judy C. Y.; Aris, John P.; Leeuwenburgh, Christiaan (2010): New insights into the role of mitochondria in aging: mitochondrial dynamics and more. In *Journal of cell science* 123 (Pt 15), pp. 2533–2542. DOI: 10.1242/jcs.070490.

Silva, Jillian M.; Wong, Alice; Carelli, Valerio; Cortopassi, Gino A. (2009): Inhibition of mitochondrial function induces an integrated stress response in oligodendroglia. In *Neurobiology of disease* 34 (2), pp. 357–365. DOI: 10.1016/j.nbd.2009.02.005.

Smirnova, E.; Griparic, L.; Shurland, D. L.; van der Bliek, A. M. (2001): Dynamin-related protein Drp1 is required for mitochondrial division in mammalian cells. In *Molecular Biology of the Cell* 12 (8), pp. 2245–2256. DOI: 10.1091/mbc.12.8.2245.

Song, Zhiyin; Chen, Hsiuchen; Fiket, Maja; Alexander, Christiane; Chan, David C. (2007): OPA1 processing controls mitochondrial fusion and is regulated by mRNA splicing, membrane potential, and Yme1L. In *The Journal of cell biology* 178 (5), pp. 749–755. DOI: 10.1083/jcb.200704110.

Song, Zhiyin; Ghochani, Mariam; McCaffery, J. Michael; Frey, Terrence G.; Chan, David C. (2009): Mitofusins and OPA1 mediate sequential steps in mitochondrial membrane fusion. In *Molecular Biology of the Cell* 20 (15), pp. 3525–3532. DOI: 10.1091/mbc.e09-03-0252.

Stadtman, E. R.; Berlett, B. S. (1998): Reactive oxygen-mediated protein oxidation in aging and disease. In *Drug metabolism reviews* 30 (2), pp. 225–243. DOI: 10.3109/03602539808996310.

Suzuki, C. K.; Suda, K.; Wang, N.; Schatz, G. (1994): Requirement for the yeast gene LON in intramitochondrial proteolysis and maintenance of respiration. In *Science (New York, N.Y.)* 264 (5156), pp. 273–276. DOI: 10.1126/science.8146662.

Tatsuta, Takashi; Langer, Thomas (2008): Quality control of mitochondria: protection against neurodegeneration and ageing. In *The EMBO Journal* 27 (2), pp. 306–314. DOI: 10.1038/sj.emboj.7601972.

Tieu, Quinton; Okreglak, Voytek; Naylor, Kari; Nunnari, Jodi (2002): The WD repeat protein, Mdv1p, functions as a molecular adaptor by interacting with Dnm1p and Fis1p during mitochondrial fission. In *The Journal of cell biology* 158 (3), pp. 445–452. DOI: 10.1083/jcb.200205031.

Twig, Gilad; Elorza, Alvaro; Molina, Anthony J. A.; Mohamed, Hibo; Wikstrom, Jakob D.; Walzer, Gil et al. (2008): Fission and selective fusion govern mitochondrial segregation and elimination by autophagy. In *The EMBO Journal* 27 (2), pp. 433–446. DOI: 10.1038/sj.emboj.7601963.

van Dyck, L.; Pearce, D. A.; Sherman, F. (1994): PIM1 encodes a mitochondrial ATP-dependent protease that is required for mitochondrial function in the yeast Saccharomyces cerevisiae. In *The Journal of biological chemistry* 269 (1), pp. 238–242.

Varanita, Tatiana; Soriano, Maria Eugenia; Romanello, Vanina; Zaglia, Tania; Quintana-Cabrera, Rubén; Semenzato, Martina et al. (2015): The OPA1-dependent mitochondrial cristae remodeling pathway controls atrophic, apoptotic, and ischemic tissue damage. In *Cell Metabolism* 21 (6), pp. 834–844. DOI: 10.1016/j.cmet.2015.05.007.

Vogel, Frank; Bornhövd, Carsten; Neupert, Walter; Reichert, Andreas S. (2006): Dynamic subcompartmentalization of the mitochondrial inner membrane. In *The Journal of cell biology* 175 (2), pp. 237–247. DOI: 10.1083/jcb.200605138.

Wagner, I.; Arlt, H.; van Dyck, L.; Langer, T.; Neupert, W. (1994): Molecular chaperones cooperate with PIM1 protease in the degradation of misfolded proteins in mitochondria. In *The EMBO Journal* 13 (21), pp. 5135–5145.

Wai, Timothy; Langer, Thomas (2016): Mitochondrial Dynamics and Metabolic Regulation. In *Trends in endocrinology and metabolism: TEM* 27 (2), pp. 105–117. DOI: 10.1016/j.tem.2015.12.001.

Wang, Chao-Yung; Liao, James K. (2012): A Mouse Model of Diet-Induced Obesity and Insulin Resistance. In *Methods in molecular biology (Clifton, N.J.)* 821, pp. 421–433. DOI: 10.1007/978-1-61779-430-8_27.

Wang, Ke; Klionsky, Daniel J. (2011): Mitochondria removal by autophagy. In *Autophagy* 7 (3), pp. 297–300. DOI: 10.4161/auto.7.3.14502.

Wasilewski, Michał; Scorrano, Luca (2009): The changing shape of mitochondrial apoptosis. In *Trends in endocrinology and metabolism: TEM* 20 (6), pp. 287–294. DOI: 10.1016/j.tem.2009.03.007.

Wellen, Kathryn E.; Thompson, Craig B. (2012): A two-way street: reciprocal regulation of metabolism and signalling. In *Nature reviews. Molecular cell biology* 13 (4), pp. 270–276. DOI: 10.1038/nrm3305.

Westermann, Benedikt (2010): Mitochondrial fusion and fission in cell life and death. In *Nature reviews. Molecular cell biology* 11 (12), pp. 872–884. DOI: 10.1038/nrm3013.

Wikström, M.; Krab, K. (1979): Mechanism and stoicheiometry of redox-linked proton translocation in mitochondria. In *Biochemical Society transactions* 7 (5), pp. 880–887. DOI: 10.1042/bst0070880.

Youle, Richard J.; Narendra, Derek P. (2011): Mechanisms of mitophagy. In *Nature reviews. Molecular cell biology* 12 (1), pp. 9–14. DOI: 10.1038/nrm3028.

Zhang, Qin; Raoof, Mustafa; Chen, Yu; Sumi, Yuka; Sursal, Tolga; Junger, Wolfgang et al. (2010): Circulating mitochondrial DAMPs cause inflammatory responses to injury. In *Nature* 464 (7285), pp. 104–107. DOI: 10.1038/nature08780.